Gravimetric Detection of Pathogens and an Electrochemical Study of the Immunological Consequences of Tuberculosis Exposure

By

Leslie Ann Hiatt

Dissertation

Submitted to the Faculty of the

Graduate School of Vanderbilt University

in partial fulfillment of the requirements

for the degree of

Doctor of Philosophy

in

Chemistry

May, 2011

Nashville, Tennessee

Approved:

Professor David E. Cliffel

Professor G. Kane Jennings

Professor John A. McLean

Professor David W. Wright

To my amazing husband, Matthew, whose support and love carried me through

ACKNOWLEDGEMENTS

There are so many people I would like to thank for their support of this dissertation and of me. My family has been an endless pool of love, always encouraging me to keep going. My husband has been my amazing proof-reader. No matter what frustrations would appear during the day, he would somehow help make them alright by the end of the night. Mom, you always let me know how proud you are of me and inspire me to do better. Dad, your quick wit and teasing always make me smile. (And you always made me want to have the correct chemistry answer for you!) Sandie, I can always count on you for an enjoyable phone call and moments of laughter away from the stresses of life. Tracie, I still remember you visiting and telling me my work was boring, I still love you though! I have the best in-laws a person could ask for—Diana with her endless support and Mike with his random questions about my work. I will always be grateful for your interest in my work and love.

I would like to thank Dr. Cliffel for giving me the guidance I needed to succeed, the random real-world advice that I know will prove to be invaluable, and plenty of opportunities for personal growth. I would like to thank Dr. Wright for his quick emails, helpful comments and perspectives that were essential to the completion of this dissertation. I would like to thank Dr. McLean for always having an open door and for his ability to view my research from a different, and much needed, point of view. Even though I had fewer direct interactions with Dr. Jennings, I would like to thank him for his comments during committee meetings and for indirect interactions through his graduate students. My contact with every one of your students was positive. They were good

people with excellent ideas and helpful attitudes—something I believe directly relates to you and the respect I have for you. I would like to thank Dr. Derek Bruff and the Center for Teaching. The training and experience I received from the CFT has had a large influence my career goals. Thank you Dr. Zoorob for bringing me into the world of forensics, it has been an entertaining journey! I would like to thank each of you!

I would like to thank previous professors. Dr. Self-Davis who refused to let me change my major. Dr. Walker constantly made me go to the board and explain my work and he always believed in me. Dr. Thorthwaite, you have one of the kindest hearts of any of my professors. I appreciated every second you let me work with you, as a researcher and TA. I would not be in graduate school today if it weren't for you. Dr. Delaware from high school, you were one of the first professors who really inspired me to get my Ph.D.

I will always be thankful the wonderful group of girls God blessed me with the opportunity to survive graduate school with. We got into some mischief and I feel like I will always be able to count on you. Jen, you have been a wonderful friend. I feel like you were by my side during every up and down this past year. I am going to miss you. Heather, you will always have drama in your life, it keeps things entertaining, but I doubt there will ever be a more loyal person. Randi, just thinking about you makes me laugh. I don't even have to have a reason. Vanessa, you are a true friend with an amazing heart and ability for compassion and laughter. I will never look at a centerpiece for a wedding the same way again. Which brings me to Anh, I already miss you. You were always a good person to bounce science or life questions off of. You always pushed me to be better and were always so much fun to talk to. Rachel, my fellow giggler, you were always so much fun. I enjoyed Maggie Moo meetings with Alice and having Leila and

Ka Leng in our lab for a brief while, all wonderful people. These are the people who helped keep me sane and kept me smiling. Thank you.

So many wonderful people have just joined our lab. I know I am thankful for the wisdom and humor all the Brians provided. I was especially grateful to them during the months when it was less fun in our lab. I already appreciate each and every one of the newbies! Gong Ping, Danielle, and Mika, each of you has been a pleasure to work with. I have also been blessed to have some wonderful undergraduates in our lab. Fred, you always make me laugh and provided endless questions to distract me from my work, which I never seemed to mind. Tracy and Tesniem are sweet and funny and I am thankful for the chance to have gotten to know you. The sixth floor lab, I wish we were not separated, but every time I went upstairs each of you always had a positive attitude and was willing to help me out. I would like to thank Ron Reiserer and David Schaffer for sharing their never ending expertise and wisdom.

I am thankful to all the Thursday morning soccer guys. It wasn't enough to keep me in shape, but it was always fun! I am thankful to the office staff and stock room, they always put up with my silly questions with a smile.

I would like to thank my Christian family who has been so supportive in prayers and actions. Last but certainly not least, I would like to thank God for giving me this amazing support system and surrounding me with love.

TABLE OF CONTENTS

Page

List of Tables

LIST OF FIGURES

CHAPTER I

INTRODUCTION

The world is changing daily. Technology is improving to meet current global needs and to solve problems that we do not yet know exist. The developed world has the financial means and resources to fight infectious diseases that are serious international threats, but the developing world lags far behind. In order to bridge the gap, creative thinking must be tailored to meet the demands faced in low-resource settings. A lack of funds should not keep researchers from trying to aid those in the developing world. Necessity is the mother of invention, and in the academic world, lack of funds sometimes spurs on the best brain activity.[1] In the United States, the military has focused resources on robust medical technologies that can withstand harsh treatment in difficult environments.[2] This focus of the military has increased the funding available for microfluidic technology and has paved the way for the development of inexpensive diagnostic devices.

Further progress into the realm where life science meets immunology could allow decentralization of technology to the point where even remote villages can better handle symptomatic individuals.[3, 4] One way this goal can be achieved is with the use of biosensors which can provide real-time accurate results at even a primitive point of care (POC).[5] A biosensor is a device that incorporates a recognition element and a means of detection (Figure 1). Biosensor development must take into account the type of sample to be tested as well as any external influences that might affect the response of the signal output. Every aspect of the sensor should be tailored to meet the needs of the eventual application.

In this work, biosensors are designed to meet two final purposes: the detection of pathogens, and the assaying of cellular response to those pathogens. The first type of biosensor employs immunological gravimetric analysis using a quartz crystal microbalance (QCM) and has the end goal of pathogen detection. The second type of biosensor utilizes electrochemical analysis within microfluidic devices to further the understanding of the cellular processes involved in infection and to help find ways to diagnose and treat infected individuals.[1] This dissertation investigates the challenges of combining rapid immunological detection with low-cost technologies.

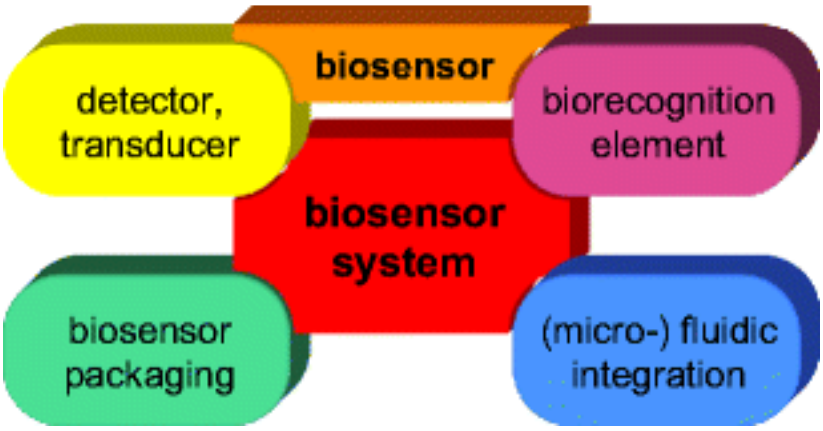

Figure 1. Components to be considered in developing an effective biosensor. Any biosensor requires both a transducer and recognition element. The exact application of the sensor will define the requirements for sensor housing and determine how much protection is required from external electrical, optical, mechanical, and biological interferents. Most biosensors also require integration with the sample through a fluidic environment.[5]

Chapters 2 and 3 discuss the use of the QCM, which was chosen for its speed and simple—but powerful—diagnostic capabilities.[6, 7] Piezoelectric devices such as the QCM would have practical use at the POC where they are easy to use, affordable, portable, sensitive, specific, and fast.[8] The QCM utilizes the reverse piezoelectric effect to record

changes in frequency that occurs from the mechanical deformation of the quartz crystal. In this work, antibodies are utilized as the immuno-recognition element that allows the change in frequency measured with the QCM to be directly related to increase in mass, similar to the original Sauerbrey equation published in 1959.[9] The QCM has previously been shown to detect viruses, bacteria, and other pathogens with selectivity and sensitivity dependent on the recognition element.[10-14] The detection of influenza (and nanoparticle simulants of influenza) and tuberculosis was achieved using the QCM.

The development of a glucose biosensor in 1962 increased demands for both enzymatic electrochemical sensors and microfluidic integration.[5, 15] Chapters 3 and 4 discuss the development of electrochemical assays and their integration into microfluidic devices for the determination of white blood cell responses to tuberculosis. Electrochemistry is sensitive and can be easily miniaturized and incorporated into a microfluidic device for real-time analysis.[1] Microfluidic devices are increasing in popularity at the POC due to the low sample volumes required and the low-cost, high-throughput reproducibility.[16-18] Electrodes can be enzymatically functionalized to increase the selectivity toward particular analytes.[16, 19] Multiple sensors can be incorporated into a single device to increase the information attained from a single sample and a more complete understanding of cellular mechanisms can be attained.[20, 21]

Diseases such as tuberculosis can be treated with medicine, and their further spread can be prevented if diagnostic resources are available at the right place and at the right time. The faster diseases are detected, the sooner patients can be quarantined and drugs distributed. However, developing nations do not have the luxuries of advanced laboratories and diagnostics, and tuberculosis and other diseases can spread and infect

millions. Approximately one third of the world's population is estimated to be infected with tuberculosis. The diagnosis of tuberculosis relies on smear sputum microscopy (a technique developed in the 1870s) and on bacterial culture to determine infectivity.[17, 22] As can be seen in Figure 2, a more sensitive analytic diagnostic for tuberculosis would alleviate a large burden of disease. If resources and innovative thinking are not applied to technologies that could be utilized in low resource settings, much of the world's population will continue to fight an invisible killer, a disease of poverty, without the tools that could have spared many lives.

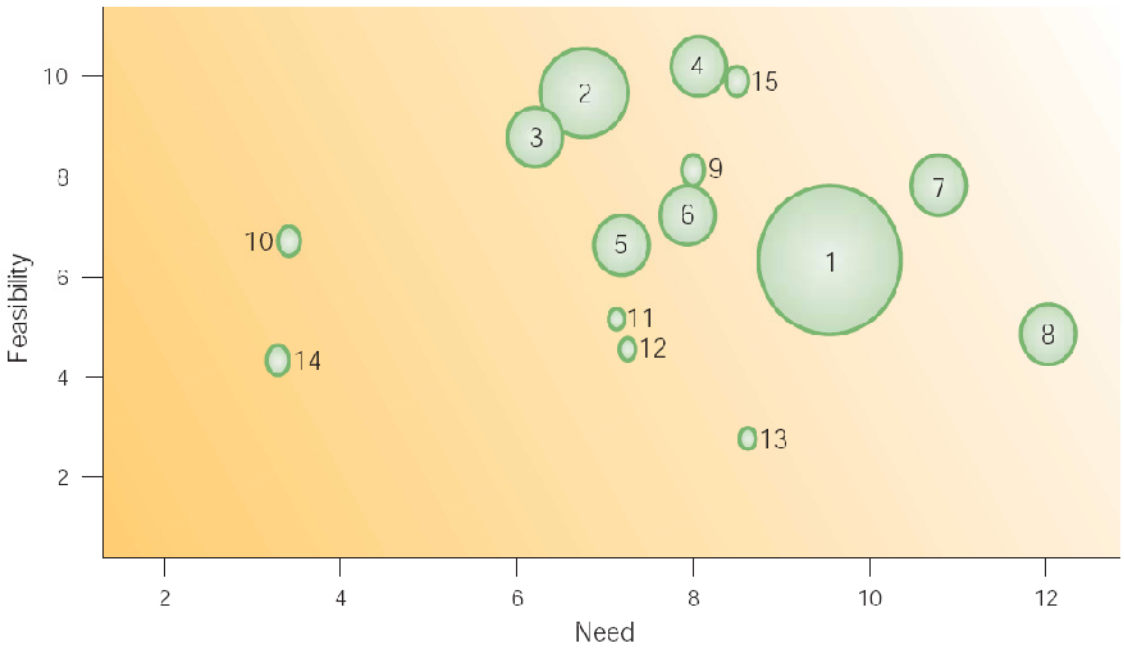

Figure 2. Assessment of priorities for development of diagnostics for diseases burdening the developing world. The horizontal axis is an arbitrary scale denoting the need for the assay; the vertical axis denotes the feasibility of developing such a test; and the size of the circle indicates the burden felt in developing countries by the disease in disability-adjusted life-years that could be prevented. 1, tuberculosis case-management; 2, malaria case-management; 3, malaria test-of-cure; 4, syphilis case-management; 5, visceral leishmaniasis test-of-cure; 6, schistosomiasis case-management; 7, visceral leishmaniasis case-management; 8, African trypanosomiasis case-management; 9, lymphatic filariasis case-management; 10, dengue case-management; 11, leprosy case-management; 12, lymphatic filariasis test-of-cure; 13, leprosy- detection of latent disease; 14, Chagas disease (South American trypanosomiasis); 15, onchocerciasis case-management. [23]

The developing world is not alone in the fight against pathogens. Diseases like tuberculosis are typically limited to third-world settings, but other pathogens can be spread through the entire world. In the age of global travel and cheap flight, any of these diseases could become pandemics—again.[24, 25] Influenza has the ability to undergo reassortment to evade host immunity and can quickly replicate and spread.[26] This is a significant biodefense fear with historical precedence dating back to the 1918 flu pandemic or the recent H5N1 scare that attracted public attention without the 50-100

million death toll.[27] As surely as bacteria and viruses adapt to evade host defenses, assays must be developed which can quickly detect the pathogen, with no risk to clinical professionals, and provide for a way of determining *in vivo* mechanisms of survival. The theme of this dissertation will center on the advancement of technologies for providing more accurate detection of pathogens (influenza and tuberculosis), the calibration of these assays, and the improvement of electrochemical sensors and microfluidic devices for the understanding of host-pathogen interactions.

CHAPTER II

REAL TIME RECOGNITION OF *MYCOBACTERIUM TUBERCULOSIS* AND LIPOARABINOMANNAN USING THE QUARTZ CRYSTAL MICROBALANCE

Mycobacterium tuberculosis (Mtb) currently affects one third of the world's population, or about 2 billion people and is a leading health concern.[22] One out of every ten people develop active *Mtb* in their lifetime and go on to infect, on average, 10-15 people a year.[22] Current techniques for diagnosing *Mtb*, such as sputum smear microscopy, the current gold standard in *Mtb* detection, lack the sensitivity needed to properly diagnose *Mtb* at the POC.[28, 29] Other approaches lack sensitivity,[30] are too expensive,[30-33] and require highly skilled personnel[34] as well as substantial time.[35, 36] New diagnostic assays would enable rapid diagnosis and treatment, therefore, preventing further spread of *Mtb*. The development of easy to use, affordable, portable, sensitive, and specific point-of-care diagnostics for tuberculosis is a critical unmet need in developing nations. An immunosensor based on the quartz crystal microbalance (QCM) meets these requirements and has been used as a platform for diagnostic immunoassays.[6, 8, 37] These assays can be adapted for use with antibodies to multi-drug resistant and extremely-drug resistant tuberculosis, reducing the time it takes to develop diagnostics for new strains of tuberculosis. Since current analytical techniques have not sufficiently demonstrated practicality for use at the POC, the use of the quartz crystal microbalance (QCM) to detect *Mtb* bacilli and antigens will be assessed as a competing technology.

The QCM has proven useful for the detection of various biological species, particularly in the examination of bacteria, with both whole cells and antigenic components of cells

studied.[6, 38-42] These detection systems function in complex environments such as serum,[43] agar,[44, 45] milk, [46] and sputum[47] without the need for labeling, which can impose additional time and cost demands.[48] Detection of whole tuberculosis cells, not surface antigens, such as LAM, with the QCM has been studied previously, but without rapid analysis.[47, 49] Real-time analysis allows for continuous monitoring of binding events and determination of kinetic constants[50] which can be used to determine whether a system is specific and sensitive enough to be used at the POC. Piezoelectric devices such as the QCM have been used routinely to determine equilibrium constants for small molecules and proteins in real time and would therefore be useful for evaluating sensors prior to introduction at the POC.[51-54]

Since detection with the QCM occurs in a process that is normally less than twenty minutes, kinetic data can be gathered and used to determine the binding affinities of each immunosensor. The stronger the attachment that occurs between antigens and antibodies, the lower the limit of detection and the greater the confidence will be in clinical settings. The Langmuir equation can be used to extrapolate equilibrium association constants (Eqs. 1-7), where θ is the degree of surface coverage, α_0 is a correlation factor, μ is the rate at which atoms strike the surface per unit area, v_1 is the rate of evaporation from a completely covered surface, K_a is the equilibrium association constant, C is the concentration, Δm is the change in mass, $\Delta m_{\max}$ is the maximum change in mass, k_a is the association rate constant, k_d is the disassociation rate constant, t is time, and τ is the time constant tau.

The equation used to define Langmuir adsorption isotherms in gaseous environments (Eq. 1) has also been used to describe isotherms occurring in liquid (Eq. 2).[55] In liquid

environments the degree of surface coverage can be represented by the change in mass at a given time over the maximum change in mass for the given concentration (Eq. 3). Incorporating this equation into the mathematical equation for Langmuir adsorption isotherms (Eq. 4) and rearranging allows for graphical determination of binding constants by varying the concentration of protein in solution (Eqs. 5-7).[56-58] These equations allow direct calculation of equilibrium constants using a linear trend line which would not be as definitive if $\Delta m_{\max}$ were instead approached asymptomatically, as is traditionally done.

$$\theta = \frac{\alpha_0 \mu}{v_1 + \alpha_0 \mu} \quad \text{(Eq. 1)}$$

$$\theta = \frac{C}{K_a^{-1} + C} \quad \text{(Eq. 2)}$$

$$\theta = \frac{\Delta m}{\Delta m_{max}} \quad \text{(Eq. 3)}$$

$$\Delta m = \frac{\Delta m_{\max} K_a C}{1 + K_a C} \quad \text{(Eq. 4)}$$

$$\frac{C}{\Delta m} = \frac{C}{\Delta m_{\max}} + \frac{1}{\Delta m_{\max} K_a} \quad \text{(Eq. 5)}$$

$$\Delta m = -\frac{\Delta m}{K_a C} + \Delta m_{\max} \quad \text{(Eq. 6)}$$

$$\frac{1}{\Delta m} = \left(\frac{1}{K_a \Delta m_{max}}\right)\left(\frac{1}{C}\right) + \frac{1}{\Delta m_{max}} \quad \text{(Eq. 7)}$$

At equilibrium, the velocities of adsorption and desorption at the surface of the crystal can be described in terms of respective rate constants and degree of surface coverage (Eqs. 8-9).[51, 59] The association and dissociation velocities can be assumed to be equal at equilibrium, and can be algebraically rearranged to form the general Langmuir isotherm (Eq. 10).

Monolayer formation with time is equal to the velocity of association minus the velocity of dissociation. Integrating this differential equation using a Laplace transform

(boundary condition $\theta = 0\ at\ t = 0$) results in Eq. 11.[60] Substituting the Langmuir isotherm using the principle of microscopic reversibility and allowing $k_aC + k_d$ to be represented by τ^{-1} presents a more simplified equation (Eq. 12).[60, 61] Using the assumption that the maximum degree of surface coverage is one and $\theta(t) = \Delta m/\Delta m_{\max}$, τ can be calculated at various concentrations (Eq. 13) and then graphed versus τ^{-1} to extrapolate k_a and k_d which can be used for comparison with isotherm methods (Eq. 14).[57, 62]

$$\nu_a = k_aC(1-\theta) \quad \text{(Eq. 8)}$$

$$\nu_d = k_d\theta \quad \text{(Eq. 9)}$$

$$k_aC(1-\theta) = k_d\theta \quad \text{(Eq. 10)}$$

$$\theta(t) = \frac{k_aC}{k_aC+k_d}\left[1 - e^{-(k_aC+k_d)t}\right] \quad \text{(Eq. 11)}$$

$$\theta(t) = \theta\left[1 - e^{-\tau^{-1}t}\right] \quad \text{(Eq. 12)}$$

$$\ln\left(1 - \frac{\Delta m}{\Delta m_{\max}}\right) = \frac{-t}{\tau} \quad \text{(Eq. 13)}$$

$$\frac{-1}{\tau} = k_aC + k_d \quad \text{(Eq. 14)}$$

Equation 5 was used in this chapter to calculate Δm_{max} and K_a.

Previous *Mtb* diagnostic research was not restricted only to the detection of tuberculosis cells, but it also included the study of a component of the cell wall, LAM.[63] Therefore, LAM is of great interest and is an ideal target for POC detection due to its extracellular position[64] and prevalence in exhaled breath, which allows for a minimally invasive detection method. In this study, immunosensors utilizing α-LAM and anti-H37Rv antibodies have been developed to detect both whole *Mtb* cells and LAM. The ability to quantify the amount of LAM in various biological fluids will help in the

understanding of its particular role in immune system evasion, as well as to gauge the infectivity of individual patients.

EXPERIMENTAL

Proteins, Cells, and Chemicals

CS-40 anti-H37Rv LAM mouse monoclonal antibody (IgG_1), α-LAM anti-H37Rv LAM rabbit polyclonal antibody (α-LAM), anti-H37Rv whole cell live infection guinea pig polyclonal antibody (anti-H37Rv), H37Rv γ-irradiated *Mtb* whole cells ($8.7x10^{11}$ bacterial cells per 1 gram of wet weight, *Mtb*),[65] and manLAM (from M. tuberculosis H37Rv, MW ~35 kDa, LAM)[66] were received as part of NIH, NIAID Contract No. HHSN266200400091C, entitled "Tuberculosis Vaccine Testing and Research Materials," which was awarded to Colorado State University, Fort Collins, CO. These samples can now be obtained through Biodefense and Emerging Infections Research Resources Repository (BEI Resources). Protein A (46,762 kDa) from Staphylococcus aureus and Protein L (35,800 kDa) from Escherichia coli were purchased from Pierce. Bovine serum albumin (BSA, 66,000 kDa), Tween® 20, tetramethylbenzidine (TMB), goat anti-rabbit IgG, and goat anti-guinea pig IgG peroxidase conjugated antibodies were purchased from Sigma Aldrich Inc. Water was purified using a Barnstead NANOpure Diamond water purification system (~18 MΩ/cm). Phosphate buffer saline (PBS) was prepared as 50 mM phosphate with 150 mM NaCl at pH 7.2, unless noted otherwise. Acetate buffer (Ace) was prepared as 100 mM acetate with 150 mM saline at pH 4.5. Carbonate buffer (CB) was prepared as 50 mM carbonate at pH 9.6. Piranha was prepared fresh as 3 parts

concentrated H_2SO_4:1 part H_2O_2 (30%). All salts and hydrogen peroxide were purchased from Fisher Scientific, while sulfuric acid was purchased from EMD Chemicals Inc.

Quartz Crystal Microbalance

Gravimetric analysis was performed with a Maxtek Research QCM. Ti/Au coated 5 MHz quartz crystals (Maxtek Inc.) were mounted in a Kynar crystal holder to allow flow *via* a Masterflex peristaltic pump. Flow rate was maintained at a speed of 30 µL/min. With a 100 µL chamber volume, this flow rate refreshes the cell volume every 3 minutes which lessens the effects of mass transport, but still allows for high sensitivity and quick detection.[37, 67] The crystals were cleaned three times prior to every experiment with piranha, H_2O, and EtOH and then dried with a stream of N_2 (g). Maxtek software records changes in frequency and resistance, which are used to determine change in mass while accounting for changes in rigidity. The liquid environment intrinsically introduces mechanical softening and stiffening based on the viscosity of the solution. Calculating the changes in resistance along with the normal frequency measurements collected allows for calculations of mass load that account for these changes in viscosity.[37] A calibration with sucrose was used to correct for changes that occur in density and viscosity similar to corrections previously reported.[57] The resulting equation (Eq. 15) used to calculate mass load incorporating this correction factor is based on the original linear relationship developed by Sauerbrey in 1959. [9]

$$\Delta m = -\frac{\Delta f + s\Delta R}{c_f} A \qquad \text{(Eq. 15)}$$

In this equation, Δm is the change in mass (µg), Δf is the change in frequency (Hz), s is the sucrose correction factor (-2.2 Hz/Ω), ΔR is the change in resistance (Ω), C_f is the

known sensitivity factor of a 5 MHz crystal (56.6 Hz cm^2 μg^{-1}), and *A* is the overlapping area of the contact electrode (0.342 cm^2).[57, 68]

Immunosensor Assembly

Binding recognition with the QCM was achieved through the selectivity of antibodies bound to the surface of the gold crystal, similar to previously described methods.[57] The formation of immunosensors was achieved with adsorption of Protein A (200 µg/mL in a 50/50 mix of PBS/Ace, pH 5.4) to the gold QCM surface.[69, 70] Next, BSA in PBS was used to block any non-specific interactions that might occur between the gold substrate and the antibodies or antigens.[71] Then the immunorecognition portion of the sensor bound with Protein A through hydrophobic interactions, either α-LAM (used at 1:1000 dilution in PBS) or anti-H37Rv (used at 1:1000 dilution in PBS).[72, 73] Similarly, Protein L (71.6 µg/mL in 50/50 mix of PBS/Ace, pH 5.4) bound CS-40 (1:20 dilution in PBS) through kappa light chain interactions.[74] PBS was used between each protein to wash away any free or weakly bound molecules from the crystal face. The combination of these three proteins creates an immuno-selective layer capable of binding tuberculosis cells and LAM (Figure 3).

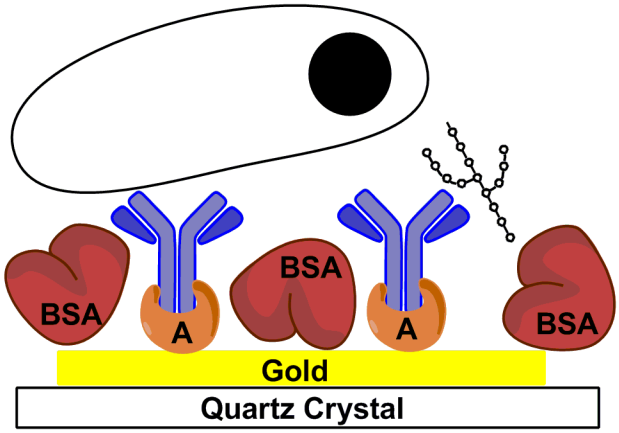

Figure 3. Illustration depicting tuberculosis and LAM detection. Protein A adsorbs to the gold surface and binds to the Fc region of a bivalent antibody. The antibody binds to LAM on the right, and tuberculosis on the left (not to scale). BSA was used to block the bare surface of the gold.

In order to characterize the immunosensors, the strength of the interactions between the antibodies and *Mtb* or LAM was measured using Langmuir adsorption isotherms. These studies examined the kinetics of the binding between the antibodies, α-LAM and anti-H37Rv, and *Mtb* or LAM. The immunosensors were introduced to inactivated tuberculosis cells at concentrations ranging from $8.7x10^4$ to $8.7x10^7$ cells/mL. The α-LAM immunosensor was exposed to LAM at concentrations ranging from 2 to 10 µg/mL. Because of limited availability and low dilution (1:10) requirements for study of CS-40, its use was restricted to binding studies with LAM at a concentration of 10 µg/mL.

Enzyme-linked immunosorbent assay (ELISA)

ELISAs similar to those developed previously by Hamasur *et al.* were developed for LAM and *Mtb* detection.[35] Other ELISA based systems used to detect LAM were also consulted.[35, 36, 66, 75]Briefly, 100 µL of antigen, either LAM or *Mtb* was plated in Immulon

2HB microplates (Fisher Scientific) in carbonate buffer at varying concentrations. The wells were incubated for 1 hour and washed with PBST (PBS with 0.05% Tween® 20). The wells were sequentially incubated for 1 hour with BSA (300 µL, 1 mg/mL), α-LAM or anti-H37Rv (100 µL, 1:1000), and the appropriate peroxidase conjugated secondary antibody (either goat anti-rabbit IgG or goat anti-guinea pig IgG) based on the species that the primary antibody was raised in (100 µL, 1:5000), washing with PBST between steps. Finally, TMB was added to each well (100 µL) as a substrate for the peroxidase conjugated antibody in order to initiate a color change. After five minutes, the reaction was halted with 2 M H_2SO_4, and the plates were read at 450 nm (BioTek Synergy HT plate reader). The limits of detection for tuberculosis cells and for LAM determined using ELISAs were compared to the limits of detection using a QCM.

RESULTS AND DISCUSSION

The development of a rapid, real-time sensor for the detection of *Mtb* and LAM that can be used at the POC will enable rapid diagnosis and treatment, thus reducing the spread of the disease. The QCM successfully measured the adsorption of *Mtb* and LAM in less than 20 minutes. Monitoring mass changes as the different immunosensor layers are introduced to the crystal allows control to be maintained over the depositions in terms of the absolute mass of each layer. Real time detection throughout the development of the entire immunosensor can be achieved (Figure 4A). In this example, Protein A (253 ng) adsorbed onto the gold substrate first, followed by BSA (10 ng) and α-LAM (51 ng). Detection of *Mtb* was seen by the increase of 12 ng immediately following its introduction to the immunosensor. Similar to kinetic measurements taken using surface

plasmon resonance, the collected data has curvature indicative of association and disassociation. These curves are common indicators of binding, and demonstrate the association of two molecules until equilibrium is reached and the curve levels off. After switching to running buffer, any weakly adsorbed molecules will disassociate as indicated by mass loss. After switching back to running buffer, mass loss is common and indicative of disassociation. A similar study was conducted utilizing anti-H37Rv (Figure 4B).

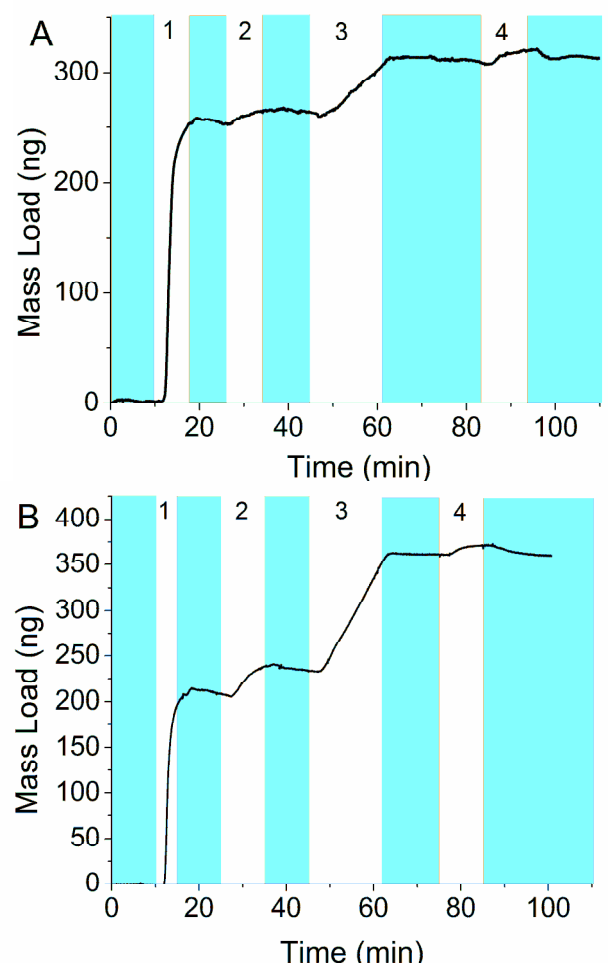

Figure 4. Real-time detection of *Mtb* ($8.7x10^6$ cells/mL) with rabbit polyclonal antibody α-LAM (A) and with guinea pig polyclonal antibody anti-H37Rv (B). PBS flow is indicated by the shaded regions. Steps 1-3 depict the building of the sensing layers and step 4 depicts the detection of *Mtb*. The total mass detected in each step is as follows: (A-1) 253 ng protein A, θ =43% (A-2) 10 ng BSA, θ=20% (A-3) 51 ng α-LAM, θ =11% (A-4) 12 ng *Mtb*, θ =1% (B-1) 207 ng protein A, θ =35%(B-2) 26 ng BSA, θ=53% (B-3) 130 ng anti-H37Rv, θ =27% (B-4) 9 ng *Mtb*, θ =1%.

The assembly of the immunosensor for antigen detection was kept as uniform as possible for all cell concentrations. Typical variation in a single run was ± 1 ng, but run to run variability was much higher. Protein A and antibody concentrations remained constant for the creation of the immunosensor, but maximum binding did vary slightly between runs; Protein A, $\bar{x}$ = 258 ± 84 ng, BSA, $\bar{x}$ = 27 ± 20 ng, α-LAM, $\bar{x}$ = 52 ± 21 ng

and anti-H37Rv, $\bar{x}$ = 96 ± 38 ng. The variation in binding for each protein is due to surface roughness, quantity of available Protein A remaining for binding, and packing efficiencies. The variation could also be due to the different orientations of the proteins on the surface of the gold.[76] Protein A can bind directly to the gold in any orientation, while the antibodies are restricted to sites occupied by Protein A.

The QCM immunosensors were able to detect *Mtb* at concentrations as low as $8.7x10^5$ cells/mL with α-LAM and $8.7x10^6$ cells/mL with anti-H37Rv. The average change in mass for each concentration is seen after introduction of *Mtb* using (A) an α-LAM immunosensor and (B) an anti-H37Rv immunosensor (Figure 5). The detection of *Mtb* with the anti-H37Rv immunosensor occurs linearly as would be expected. Examining the average binding curves for the detection of *Mtb* with the α-LAM immunosensor, one would notice the greatest change of mass occurs with a cell concentration of $4.8x10^7$ cells/mL instead of with a concentration of $8.7x10^7$ cells/mL, as would be expected. There are two hypotheses that could explain this behavior. First, at higher concentrations steric effects dominate, preventing increased binding. Second, a greater number of antibodies could have bound to Protein A for the lower concentration compared with the higher concentration, thus increasing the number of possible binding sites. Comparison of the average amount of bound α-LAM for each cell density proves the second hypothesis is invalid. The average amount of α-LAM that bound for *Mtb* ($4.8x10^7$ cells/mL) was 43 ± 22 ng, while for *Mtb* ($8.7x10^7$ cells/mL) the average antibody binding measured was 56 ± 5 ng. Therefore the greater detection was actually achieved with a lower average amount of antibody present on the surface of the crystal.

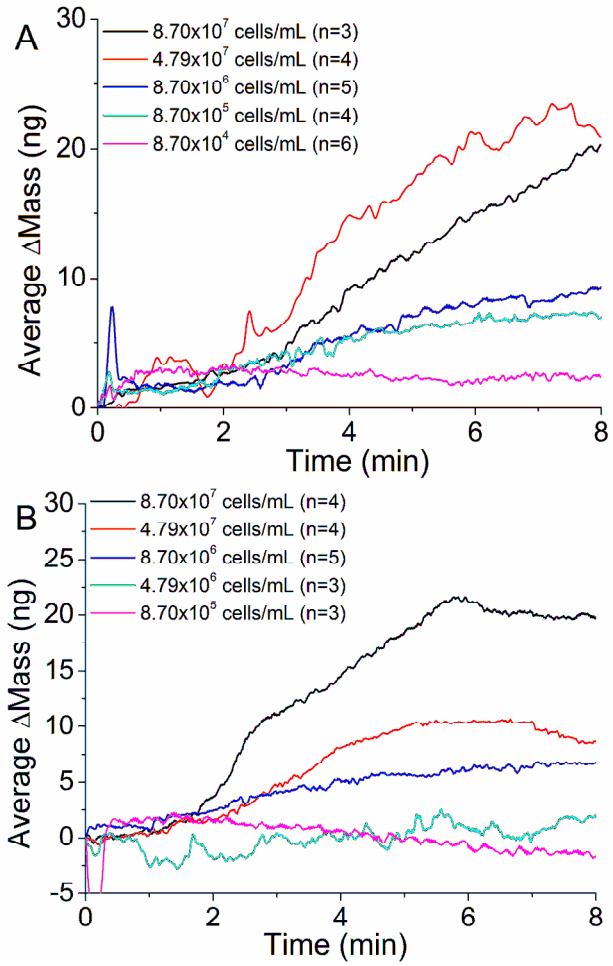

Figure 5. Average detection of varying concentrations of *Mtb* with (A) α-LAM antibodies (1:1000) and (B) anti-H37Rv antibodies (1:1000).

Too often the QCM is used to assess binding constants without giving any thought to the interactions occurring between the molecules adsorbed to the crystal face. In some instances, multi-layers can be assumed to have formed while at other times; only partial surface coverage is achieved. To determine why and how layers form, it is beneficial to examine the size and shape of the adsorbed molecules. Mathematically, one can hypothesize possible surface orientations and therefore determine how each molecule might inhibit the binding of lateral molecules on the quartz crystal. Possible orientations of each layer on the surface of the crystal must be examined.

Protein A (46 kDa) is a spherical, globular protein with a reported radius of 1.03 nm.[77, 78] Mathematically, the number of proteins that can pack on the sensitive area of the crystal (0.342 cm^2) is dependent on the size of the protein and on the packing density. Multiplying by the molecular weight of Protein A yields the change in mass (784 ng) that can be attained for this surface with no space between molecules. If it is assumed that the maximum monolayer surface coverage by this spherical protein could take a face-centered packing lattice, then the protein could maximally pack at 74% efficiency as has been determined using the Kepler conjecture.[79] At 74% packing efficiency, the change in mass would instead be 588 ng. With an average Protein A binding of 258 ± 84 ng, this translates to a surface coverage of 44 ± 14%.

BSA is a protein with a cardioid shape whose radius and dimensions have received much scrutiny with reported radii ranging from 3.3-4.5 nm.[80-86] Representing BSA with spherical calculations would fail to take into account the possible orientations with which BSA can adsorb. Rezwan *et al.* have suggested an adsorption model based on zeta potential and UV-Vis measurements.[87] They presented a "side-on" model calculating surface coverage from the smaller axis (223 ng/cm^2) and "end-on" models calculated from the larger axis (365 ng/cm^2). Using these models, maximum adsorption for a monolayer of BSA on the quartz crystal would be in the range of 76-125 ng. With an average BSA adsorption of 27 ± 20 ng, the QCM crystal is most likely covered with molecules in both conformations and the surface coverage of BSA is in the range of 36 ± 26 to 22 ± 16% covered with BSA. Analyzing the possible conformations of BSA and Protein A helps demonstrate why there is such variation between runs and how 100% of the surface could be covered with completely different ratios of Protein A and BSA.

Future studies should incorporate the use of pegylated thiols or any smaller blocking agent to ensure greater surface coverage and to prevent and non-specific binding and steric hindrances that might arise. Sea block, casein and octanethiol were all used as blocking agents, but similar non-specific binding to monkey samples precluded their continued use.

IgG antibodies can adsorb onto a surface in multiple orientations due to the y-shape formed from the Fc and Fab regions of the protein. As mentioned earlier, Protein A binds to the Fc region of the antibodies used in this study, which eliminates many orientations of adsorption leaving only rotations that occur along the radius of gyration (*Rg*, Figure 6.). There are many ways to mathematically represent the possible orientations that IgG molecules could assume while bound to Protein A. Literature reports the dimensions of IgG antibodies as follows (Figure 6): *Fab-Fab* (14.2 nm)[88], *height* (11.5, 14.0 nm)[89], *Fc-Fab* (13.6 nm)[90], *Fc* (0.91[78], 3.8[88] nm), *Rg* (6,[85] 5.5[91], 5.6[92] nm), *a* (8.5 nm)[88], *b* (4.5 nm)[88], *c*d*e* (7x5x4 nm)[88], *x-y-z* (8.3-7.3-7.9 nm)[93]. This study uses these reported dimensions in the comparison of two probable IgG representations, a spherical and an elliptical representation, in order to calculate packing efficiency and steric hindrance. The first model calculates steric effects using a spherical representation with an average of reported *Rg* values, 5.7 nm, for various IgGs. This model assumes that the molecules will pack in such a way that each molecule will sterically hinder neighboring molecules and prevent them from being closer than their *Rg* would allow. The second model utilizes an elliptical representation. With an elliptical representation, the molecules could pack more densely, but this could only take place if the molecules were oriented with their Fab regions parallel to each other. From this information, a spherical representation, assuming

a 75% packing efficiency, would allows for a maximum mass change for a monolayer of IgG antibody to be 87 ng. Basing the calculations on an elliptical shape using the average of *d* and *b* for the width, and *Fab-Fab* for the length, and 75% packing efficiency yields a maximum monolayer formation of 159 ng. Using the spherical model, the Protein A/BSA layer would therefore be 60 ± 24% covered with α-LAM or 110 ± 44% covered with anti-H37Rv. Comparatively, using the elliptical model the binding detected translates to 33 ± 13% surface coverage with α-LAM and 60 ± 24% surface coverage with anti-H37Rv. The actual surface coverage of IgG antibodies relies on random orientation within any of Protein A's four binding pockets and therefore could pack with the Fab regions parallel or perpendicular to each other resulting in a mixture of orientations. The more ordered the packing, the more antibodies that can be present on the sensor, which would increase the number of binding sites possible for antigen detection.

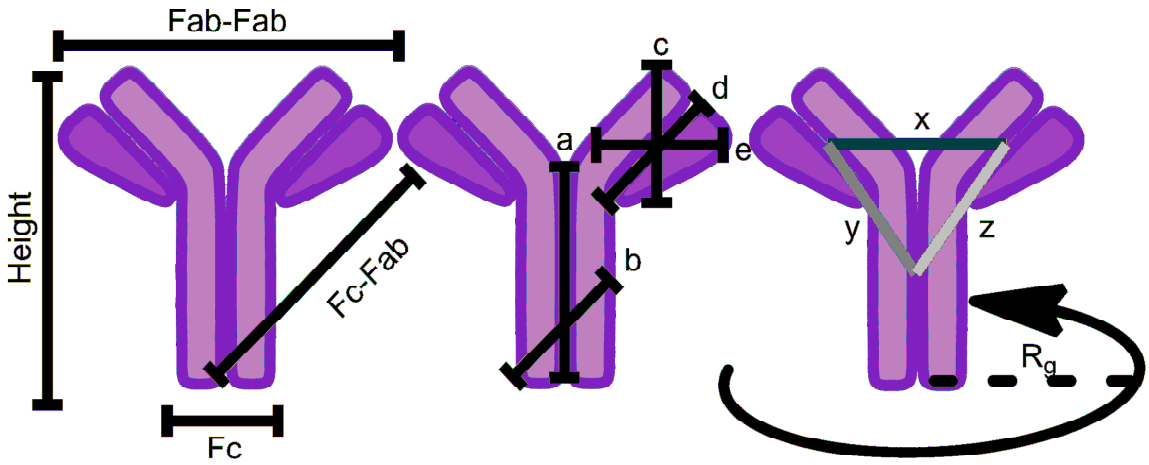

Figure 6. Dimensions of IgG antibodies as reported in literature: *Fab-Fab* (14.2 nm)[88], *height* (11.5, 14.0 nm)[89], *Fc-Fab* (13.6 nm)[90], *Fc* (0.91[78], 3.8[88] nm), *Rg* (6,[85] 5.5[91], 5.6[92] nm), *a* (8.5 nm)[88], *b* (4.5 nm)[88], *c*d*e* (7x5x4 nm)[88], *x-y-z* (8.3-7.3-7.9 nm)[93]. These were used to develop spherical (using *Rg*) and elliptical (using *d* and *b* for the width, *Fab-Fab* for the length) representations that could be used to examine possible orientations of the IgG molecules immobilized on a QCM crystal through binding of its Fc region to Protein A, thus predicting maximum surface coverage.

Coverage by *Mtb* could also be represented by an ellipse with a width of 0.44 µm and a length of 3 µm.[94] This would yield a maximum theoretical surface coverage of 1.88 µg which translates to an experimental surface coverage of 1.3% using the maximum detection of *Mtb* cells. Considering the binding that occurs spatially, when the *Mtb* cells lay on the immunosensor, they could physically make contact with $1.9x10^4$ IgG molecules based on the elliptical model of IgG molecules described previously. When one antibody binds a cell, the orientation of the remaining epitopes on the cell will only bind if the spacing between antibodies and epitopes matches up perfectly. Imperfect matching leads to strained or weakened bonds that would lessen the affinity of the sensor for the cell versus a sensor with complimentary spacing of IgG. However, the imperfect matches would still be stronger than singular attachment mechanisms. Based upon the amounts of antibodies and cells detected, enough antibodies were present to saturate the surface of the cell, but it is not likely that every antibody in the immunosensor was able to bind to an epitope on the cell surface. It is believed that the low percentage of surface coverage by *Mtb* is indicative of steric hindrances due to the spatial orientation of epitopes on the cell as compared with the spatial orientation of the IgG molecules in the immunosensor. This contributes more to *Mtb* surface coverage than the added strength that would come from multiple antibody attachments.

In order for a reaction to be energetically favorable, the association kinetic rate constant must be larger than the dissociation rate constant. Immobilized interactions on the quartz crystal versus interactions in solution do not have statistically different kinetics.[95] QCM measurements make it possible to observe on and off rates of binding directly in rapid succession, and allow the affinity constants to be determined for each antibody-based

sensor by examining the binding at multiple antigen concentrations. Since the Langmuir isotherm is a good fit to the *Mtb* binding curves with α-LAM and anti-H37Rv, it is expected that the affinity coefficients would have little error in their values (Figure 7). K_a and maximum change in mass (Δm_{max}) for the interaction of *Mtb* with both antibodies (α-LAM and anti-H37Rv) were determined using the linear representation of the Langmuir equation (Eq. 5). The Langmuir isotherm (Figure 7) can be used to extrapolate Δm_{max} since it asymptotically approaches Δm_{max} (Eq. 16), but this requires making approximations. Figure 7.The Δm_{max} for the interaction of α-LAM to *Mtb* was 23±1 ng and for the interaction of anti-H37Rv to *Mtb* was 14±1 ng. The interactions are energetically favorable and the affinity of the antibodies to *Mtb* is high. The K_a for both relationships was much higher than expected for antibody-antigen interactions (Table 1).[96] The attachment of multiple antibodies would strengthen the K_a of *Mtb* to the immunosensor, and the dissociation would be dictated by the mass of the cell as well as the strength and number of antibodies which attach the cell to the QCM crystal.[97] The high K_a demonstrates the avidity occurring from multiple antibodies binding per cell on the QCM surface.

$$\lim_{C\to\infty} \frac{\Delta m_{max} K_a C}{1 + K_a C} = \lim_{C\to\infty} \frac{\Delta m_{max} K_a}{\frac{1}{C} + K_a} = \lim_{C\to\infty} \frac{\Delta m_{max} K_a}{0 + K_a} = \Delta m_{max} \quad \text{(Eq. 16)}$$

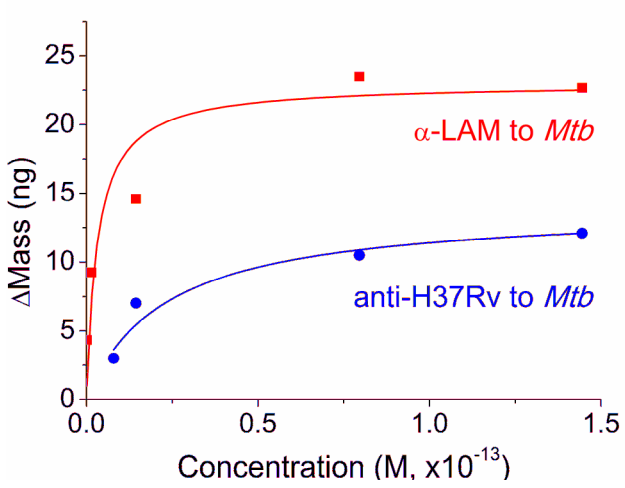

Figure 7. Rectangular hyperbolic fits of *Mtb* binding with α-LAM and anti-H37Rv to the Langmuir isotherm obtained using the Δm_{max} and K_a determined from the linear rearrangement of the Langmuir equation (Eq. 5). (R^2=0.99 for both α-LAM and anti-H37Rv)

Table 1. Equilibrium association and rate constants determined for the interaction of *Mtb* and LAM with either α-LAM or anti-H37Rv antibodies.

	Δm_{max} (ng)	K_a (M^{-1})	k_a ($M^{-1}s^{-1}$)	k_d (s^{-1})
αLAM to mTb	23 ± 1	3.1 ± 2.4 (x10^{14})	4.3 ± 7.7 (x10^{11})	0.2 ± 0.1
anti-H37Rv to mTb	14 ± 1	4.4 ± 1.2 (x10^{13})	2.9 ± 1.0 (x10^{12})	0.1 ± 0.1
αLAM to LAM	12 ± 17	1.3 ± 0.5 (x10^{7})	2.3 ± 1.5 (x10^{6})	0.7 ± 0.3

The QCM detection of LAM was achieved in a manner similar to the attenuated or weakened *Mtb* cells. Real-time detection of LAM at varying concentrations with α-LAM was achieved at a pH of 7.0 and 7.2. Statistical analysis was performed, and it was determined that there was no difference between detection achieved with the immunosensors at the differing pHs. Even though it was thought that the change in pH might change the protein's surface charges and therefore packing efficiency, this study appears to support previous findings which found that the adsorption behavior of proteins

was independent of pH in the range of 6.5-7.5 at high ionic strength.[98] Although LAM is a not a protein, this rule appeared to hold true for adsorption based on the average moles of LAM detected. Detection of LAM was demonstrated (Figure 8), and the kinetics of the combined data sets at pH 7.0 and 7.2 were examined (Table 1). The K_a for the detection of LAM with α-LAM is in the range expected for antibody antigen interactions, from 10^6-10^{10} M^{-1}.[96] Unlike *Mtb*, whose K_a was increased due to avidity, LAM is a small molecule and interaction with α-LAM would be one-to-one and would therefore be expected to fit in this range. High association rate constants were also observed which explains the sharp binding curve measured with the QCM. The significantly lower dissociation rate explains why the saturated antigen layer would have slow dissociation from the sensor surface. The amount of LAM that bound was highly variable, Δm_{max}=12±17 ng, which could be due to the heterogeneity in LAM size, 1-2 nm wide and 5-10 nm in length, as well as the pooled error that arises from the compilation of data from differing pHs. Based on mathematical approximations of the size and shape of LAM, 47 ng could bind to the surface of the QCM immunosensor before encountering complete steric hindrance.[94] The average amount of LAM that bound to the surface of the QCM (10 ng) is equivalent to a surface coverage of 21%. Comparing the average moles of α-LAM that bound with the average moles of LAM detected, a ratio of approximately 1:1 is calculated, and therefore it appears that the amount of LAM that binds is limited by the amount of antibody bound to the sensor. The limit of detection (LOD) in this binding study was determined to be 0.3 nM using the Langmuir isotherm for the interaction of α-LAM with LAM. Detection was experimentally confirmed at a concentration as low as 60.6 nM. Furthermore, sensor reusability was confirmed through the binding of Mtb followed by the binding of LAM

(Figure 9). The following control experiments were also utilized and no nonspecific binding was seen: (1) Prot A followed by BSA then LAM or *Mtb* with no antibody, (2) complete assembled immunosensors with an Ebola virus glycoprotein, mannose, and arabinose, and (3) BSA followed by LAM.

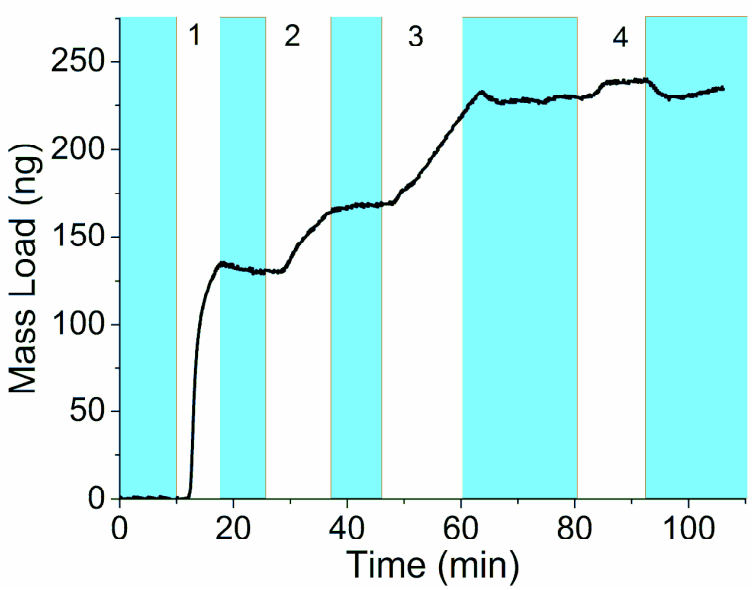

Figure 8. Real-time detection of LAM (8 µg/mL). The total mass detected in each step is as follows: (1) 131 ng protein A, θ =22% (2) 39 ng BSA, θ =78% (3) 61 ng α-LAM, θ =13% (4) 12 ng LAM, θ =26%.

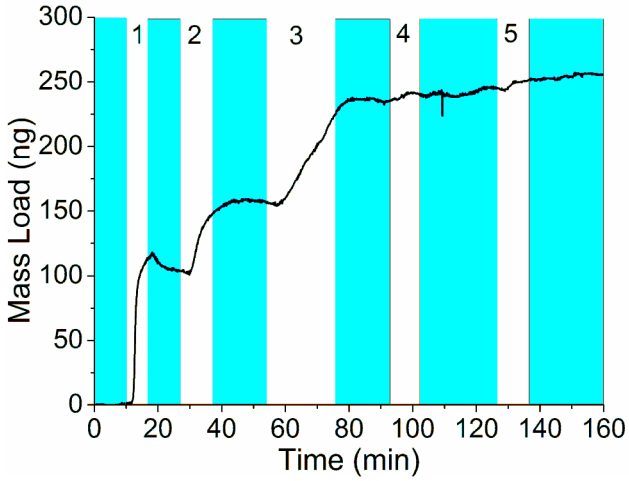

Figure 9. Reusability of the α-LAM immunosensor is demonstrated with sequential binding of *Mtb* and then LAM. The total mass detected in each step is as follows: (1) 101 ng protein A, θ =17% (2) 53 ng BSA, θ =106% (3) 83 ng α-LAM, θ =18% (4) 4 ng *Mtb*, θ =0.3% (5) 6 ng LAM, θ =13%.

Whole tuberculosis cells and LAM were detected with ELISA to corroborate the results attained using the developed QCM immunosensor. ELISA confirmed that the interaction of α-LAM and anti-H37Rv to *Mtb* increased with the concentration of cells present in the well plate (Figure 10). The LOD was determined as the average background plus three times the average standard deviation. The LOD for the interaction of *Mtb* and α-LAM was calculated to be 1.5×10^4 cells/mL, while the LOD for the interaction of *Mtb* with anti-H37Rv was calculated to be 1.3×10^5 cells/mL. As mentioned previously, the LOD for the QCM immunosensors was 8.7×10^5 cells/mL with α-LAM and 8.7×10^6 cells/mL with anti-H37Rv, both one order of magnitude higher than the ELISA results.

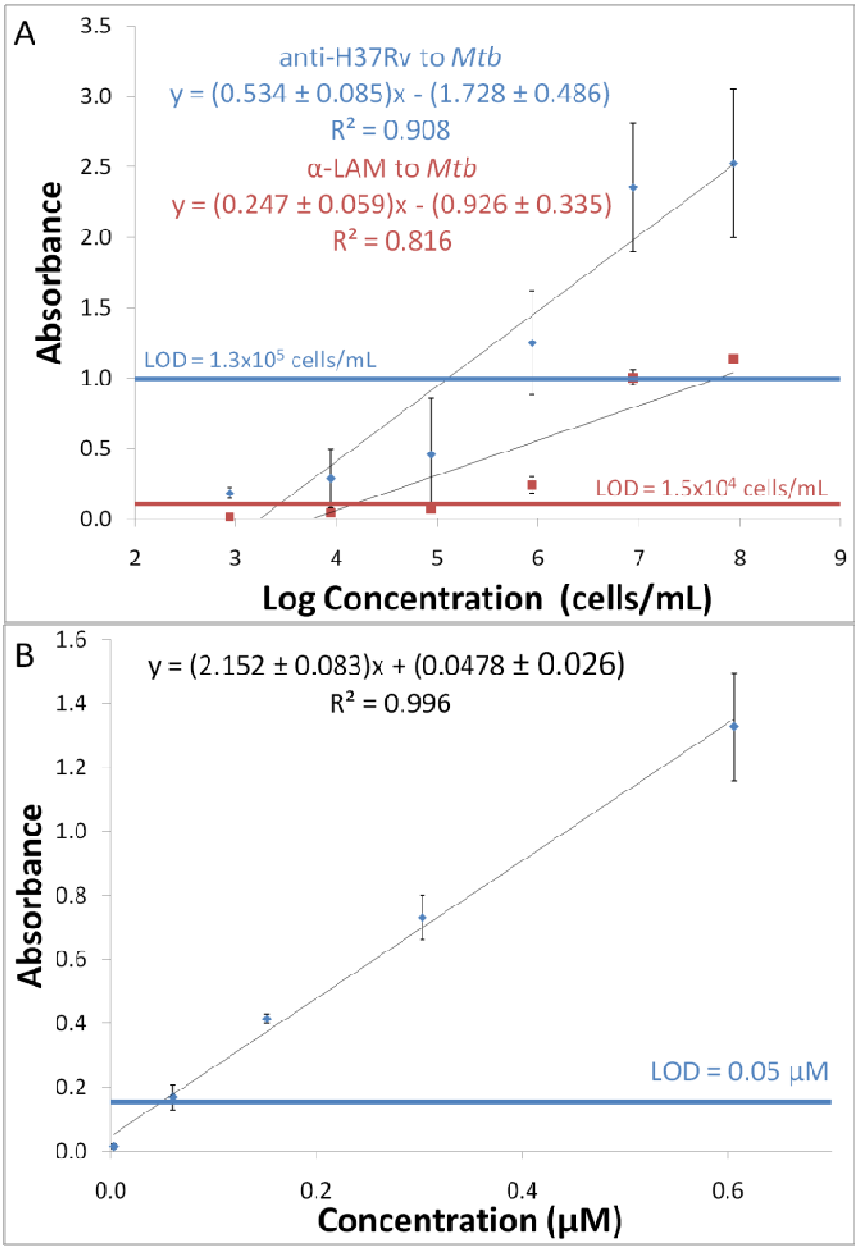

Figure 10. ELISA detection of *Mtb* and LAM. (a) Detection of *Mtb* using anti-H37Rv and α-LAM (b) and of LAM using α-LAM.

There has been much discussion over the benefits of ELISA versus QCM. While ELISA is normally considered a gold standard, the QCM has been found to be more sensitive in some instances.[8] ELISA benefits from natural fluorescent signal amplification, while QCM is faster with real-time results relying on the densities of the

adsorbed particles for signal amplification. The ELISA results utilized whole cells which were attached to the well plate first. Then antibodies were allowed to attach to epitopes on the surface of the cell in any conformation. As stated previously, with QCM the antibodies were used as an immunosensor and thus more antibodies where sterically prevented from binding to the cells.[99] The LOD for ELISA was therefore improved through the increased fluorescence amplification that occurs with multiple attachments of antibodies that were not sterically hindered to the extent that they were within the QCM. The LOD for the interaction of α-LAM and LAM was determined to be 0.05 μM. The LOD achieved with the QCM for LAM was lower (0.3 nM) than the LOD confirmed with ELISA (0.05 μM). This detection was possible even with the low surface coverage of antibodies present on the crystal.

Additional antibodies were briefly studied for the assessment of their usefulness in LAM detection using the QCM. Anti-H37Rv polyclonal antibodies were raised against whole *Mtb* cells in guinea pigs (CSU) and as such were found to have no binding affinity for LAM in both ELISA and QCM experiments. Binding of LAM (10 μg/mL) to CS-40 had an average binding in the QCM of 6 ± 2 ng. Kinetic analysis and ELISA detection of LAM with CS-40 were not possible considering the large quantity of CS-40 required and the limited quantity available. Future experiments could incorporate drug resistant antibodies as they are generated to quickly adapt at the POC with the development of these mutant strains.

The simplicity of using the QCM for early detection of LAM and *Mtb* could have immediate impact in clinical settings as antibodies are developed with higher affinity and selectivity. The sensitivity with which these immunosensors can detect non-processed

bacilli and lipoarabinomannan renders them a potent tool in the fight against tuberculosis worldwide. The LAM immunosensor in particular would have a great advantage for use in clinical settings where its ability for detecting LAM in such small quantities in a non-invasive and timely manner could be utilized.

CONCLUSIONS

Tuberculosis whole cells were detected in a more sensitive and specific method than is currently available. The QCM was shown to be a valid method for detection of both *Mtb* whole cells and LAM. The association and dissociation of *Mtb* and LAM to the immunosensor surface was seen in less than twenty minutes through changes in frequency and resistance. This binding was analyzed to infer information about the kinetics governing the interactions. The average binding to α-LAM and anti-H37Rv at various concentrations was used to extrapolate equilibrium association constants and rate constants. These constants describe the strong affinity with which the immunosensor bound the antigens in the QCM while ELISA was used to affirm the interaction. Mathematical representations were used to describe possible orientations of the molecules on the surface of the QCM. The affects of steric hindrances on both surface coverage and binding affinities was examined. The α-LAM immunosensor has a strong affinity for LAM, which is present in exhaled breath and can be collected noninvasively. Therefore, the α-LAM immunosensor has the most promise for use in POC settings.

ACKNOWLEDGEMENTS

This work was supported in part by NIH GM 076479 and through the kind donations from Colorado State University, NIH, NIAID Contract No. HHSN266200400091C, entitled "Tuberculosis Vaccine Testing and Research Materials". We thank Dr. Chad Roy from Tulane National Primate Research Center for his suggestions to study LAM as a possible antigen useful for diagnosis, and for the exhaled breath samples from his lab's rhesus macaques. L. A. Hiatt thanks Dr. R. Gerald Keil from the University of Dayton for QCM training during his time on sabbatical at Vanderbilt University.

CHAPTER III*

MULTIFUNCTIONAL NANOPARTICLES AS SIMULANTS FOR A GRAVIMETRIC IMMUNOASSAY

*This work represents a collaborative partnership between the labs of Dr. Cliffel and Dr. Wright. Scott A. Miller synthesized the nanoparticles and peptides, while R. Gerald Keil characterized them. I ran the QCM experiments, designed and ran all HA Protein experiments, as well as reworked all kinetics and other calculations. All work performed by colleagues is noted.

Viruses are the smallest form of life on earth with the ability to replicate and spread within living cells.[27] As they pass from cell to cell, they adapt to evade host immunity and spread disease, creating some of the worst pandemics in history.[24] Improving diagnostics for viruses like influenza would help slow the spread of infection in the event of an emerging virus. It is known that even with reassortment, a common viral defense mechanism, the majority of anti-hemagglutinin (anti-HA) antibodies recognize a specific sequence of nine amino acids within the epitope. This sequence, AYDPVDYPY, has been the focus of many assays to improve the detection of influenza.[26] Using this immunodominant sequence for the HA epitope, the influenza epitope can be mimicked with a functionalized nanoparticle that yields a comparable affinity to the linear peptide.[100] Another virus, Ebola, has also been effectively mimicked with a monolayer-protected cluster (MPC) through functionalization of the MPC with the antigenic determinant of the Ebola glycoprotein.[13] This way of integrating biology and materials

chemistry using biomimicry has allowed materials chemistry the opportunity to improve current diagnostic techniques and limits of detection, but further improvements are still yet to be made.[101]

The utilization of immuno-molecular recognition in the assembly of nanoscale sensors has applications in medical diagnosis, treatment, and the understanding of diseases.[102] Enzyme-linked immunosorbent assay (ELISA) is widely utilized in clinics and hospitals as an initial screening for several infectious diseases. While ELISA can be effectively employed in laboratory settings for common infectious agents, several obstacles inhibit the adaptation of this standard clinical assay to portable or select agent detection schemes. Unfortunately, pathogenic agent detection requires calibration with irradiated or otherwise attenuated samples of the organism. This requirement limits the widespread use of immunosensor diagnostics because of the scarcity of these agents and the logistic difficulties in transporting them safely to remote locations. Recent cases like the development of meningitis and tularemia infections in researchers who were working with the causative agents of these diseases alerts scientists to the hazards accompanying work with live calibrants.[103] The possibility of exposure and high cost are enough to warrant investigation into a safer positive control for these disease detection assays and devices. Without a positive control, the operational status of the sensor cannot be determined. Thus, the development of a nanoparticle mimic would be a safer alternative to current methodology and could be extended to address the needs of other assays that incorporate well defined epitopes.

Many traditional clinical assays lack the ability for electronic adaptation and timely results. The need exists for rapid, sensitive, and inexpensive methods that could be

utilized in clinical settings.[104] Therefore, the rapid real-time quantification of a QCM has been combined with the selectivity of monoclonal antibodies to create an immunosensor for the evaluation of multifunctional nanoparticles. The use of a QCM for immunological detection has been demonstrated previously, where it has been shown to detect *Staphylococcus epidermidis* in clinical samples using nanoparticle amplification,[10] severe acute respiratory syndrome (SARS) coronavirus in sputum samples,[11] plant pathogens,[12] an antigenic mimic of Ebola[13] and influenza A and B from nasal washes.[14] In QCM assays, nanoparticles have enabled simultaneous parallel detection and amplification for gravimetry, thus lowering the limit of detection.[101, 105-108] A QCM-based sensor with a nanoparticle control would allow for the simultaneous rapid and accurate analysis of multiple viral or biological hazards, without posing a safety or health threat to the operators. The work reported here builds on this previous work and addresses the specificity of detection of antibody-antigen binding at the QCM using poly-epitope functionalized gold nanoparticles.

Gold nanoparticles have favorable characteristics for their use as the basis for multifunctional microorganism simulants.[109] Nanoparticle size, shape, and capacity for surface modifications, based on chemical characteristics and environments, make the use of nanoparticles advantageous for detection, discovery, and diagnosis.[102, 110] Previous studies have shown that nanoparticles are capable of accepting a wide array of functional molecules *via* the Au-thiol bonds at the interface of the ligand and particle.[111] Since the physical and chemical properties of nanoparticles are dependent upon size,[101] the gold nanoparticles can be customized to simulate the variability in pathogen size. MPCs in this work had an average diameter of 2.6 ± 0.6 nm. Influenza virions vary in size, generally

around 100 nm in diameter, but smaller nanoparticles were chosen in this study since they have a larger surface area to volume ratio, therefore increasing the ratio of possible antigen presentation to gold core.[112] These nanoparticles were poly-functionalized to increase the presentation of the nanoparticle epitope to the antibody. Previous studies have found that multivalent ligand attachment to gold nanoparticles enhances the affinity measured in binding studies.[113, 114] The selectivity of antibody sensors for functionalized MPCs has been examined using two orthogonal epitopes, FLAG and HA. The FLAG epitope is a biological peptide sequence commonly used for identification of proteins in biological samples.[115] HA and FLAG functionalized MPCs can be used as a synthetic simulant and negative control for the HA epitope of the influenza virus.[116, 117] The binding of these nanoparticles was also compared with binding of a negative-control Au-tiopronin nanoparticles and an authentic sample of H5 HA proteins from influenza virus (H5N1). The simulants works as safe controls whose application could be extended to address various pathological threats, in scenarios in which using attenuated controls is problematic for safety or security concerns.

EXPERIMENTAL

Chemicals

Gold shot was purchased from precious metal vendors (Canadian Maple Leaf, 99.99%) and was initially converted to $HAuCl_4 \bullet 3\ H_2O$ by boiling Au^0 in HCl/HNO_3 solution.[118] N-(2-Mercaptopropionyl)-glycine (tiopronin, reagent grade), bovine serum albumin (BSA, fraction V, 96%), and sodium phosphate (monobasic, reagent grade) were purchased from Sigma. Other chemicals were obtained as follows: Protein G was

purchased from Southern Biotech, Fmoc-dPEG-COOH from Quanta Biodesign, anti-FLAG mouse monoclonal antibody from Stratagene, and anti-HA mouse monoclonal antibody from the Vanderbilt Molecular Recognition Core facility. The following reagent was obtained through the NIH Biodefense and Emerging Infections Research Resources Repository, NIAID, NIH: H5 hemagglutinin (HA) protein from influenza virus, A/Hong Kong/156/97 (H5N1), recombinant from baculovirus, NR-652 (56 kDa).[119] Analytical grade solvents for NMR were obtained from Cambridge Isotope Laboratories, and water was purified using a Modulab Water Systems unit (~18 MΩ/cm). Buffers were prepared according to standard laboratory procedure. Other chemicals were reagent grade and used as received.

MPC Synthesis and Characterization

Gold-tiopronin protected MPCs were synthesized by S. A. Miller as previously described.[120-122] Briefly, tiopronin protected gold nanoparticles were synthesized by dissolving tiopronin and $HAuCl_4 \bullet 3\ H_2O$ (3:1) into a MeOH/acetic acid solution (6:1). The reaction was stirred for 30 minutes and then cooled in an ice bath. $NaBH_4$ was then added in 10 x molar excess of gold. Reaction product was stirred for one hour. The solvent was removed under vacuum and the pH was lowered to 1 with concentrated HCl. Reaction product purification by dialysis with cellulose ester membranes (Spectra/Por CE, MWCO = 10,000) removed any excess tiopronin. Average particle diameter was determined by transmission electron microscopy (TEM). TEM images were taken by R. G. Keil on a Phillips CM20 instrument after applying aqueous MPC samples to Formvar-coated 200-mesh copper grids (Ted Pella). The microscope operated at 200 keV with

magnification in the range 150-750,000 x. Thermogravimetric analysis (TGA) was performed by R. G. Keil with a TGA 1000 (Instrument Specialists, Inc.) to calculate Au-tiopronin stoichiometry. From TEM and TGA data the nanoparticle size and Au-tiopronin stoichiometry were obtained. MPCs used in the following experiments had an average diameter of 2.6 ± 0.6 nm and a base composition of $Au_{544}Tiop_{204}$ (140.4 kDa), calculated from TEM and TGA data (at 650 °C) respectively.[123-125]

Peptide Synthesis and Characterization

The FLAG and HA epitopes were synthesized by S. A. Miller with standard 9-fluorenylmethoxycarbonyl (Fmoc protocols on a solid resin support).[126, 127] Epitope sequences were modified with a linker region comprised of a discrete polyethylene glycol (PEG purchased as Fmoc-dPEG™ from Quanta Biodesign) and a C-terminal cysteine. PEG was added to attenuate non-specific binding, while the C-terminal cysteine provided a thiol linkage to the gold surface. PEG formed the link between the cysteine and the rest of the peptide, *e.g.,* HA-PEG-C. After initial MPC studies performed without the PEG linker were found to have no binding, all future studies incorporated this linkage. The notations HA-Au, HA-FLAG-Au, and FLAG-Au are assumed to include the incorporation of this linkage. Epitope antigens HA (AYDPVDYPY-$(PEG)_6$-C, 1562.6 Da) and FLAG (KDDDDKYD-$(PEG)_6$-C, 1451.5 Da) were synthesized on an Apex 396 (Advanced Chemtech) equipped with a 96-well reaction block capable of vortex mixing. 2-chlorotrityl resin was swollen in dichloromethane (Fisher) prior to synthesis.[128] Fmoc amino acids (Synpep) and Fmoc-$dPEG_6$ Acid (Quanta Biodesign) were coupled using O-Benzotriazole-N,N,N',N'-tetramethyl-uronium-hexafluoro-phosphate (HBTU, 5eq with

respect to resin, Synpep), 1-hydroxybenzatriazole (Hobt, 5 eq, Synpep), N,N-Diisopropylethylamine (DIEA, 10 eq, Advanced Chemtech) in N,N,-dimethylformamide (DMF, Fisher). Peptides were cleaved with 90% (v/v) trifluoroacetic acid, 5% anisole (Sigma), 3% thioanisole (Sigma), and 2% ethanedithiol (Sigma). Final purification was performed on a Waters C18 semi-prep reversed-phase high pressure liquid chromatography (RP HPLC) column using a water (0.05% trifluoroacetic acid and acetonitrile) gradient. Peptide identity was confirmed *via* matrix-assisted laser desorption/ionization time-of-flight (MALDI-TOF) analysis.

Place Exchange

Place exchange reactions between tiopronin-MPCs and thiolate-containing peptides HA and FLAG followed a method similar to Hostetler and co-workers[109, 129, 130] and assumes that epitope-tiopronin S_N2 place exchange is one for one. While it has been shown by nuclear magnetic resonance (^{1}H NMR) that the interchange of ligands is 1:1, the final ratio of original ligand to exchanged ligand depends on ligand length, concentration of entering and exiting ligands, and the placement of the ligand (vertice, edge, or terrace) on the surface of the cluster.[109, 129] It should also be noted that the reported ratio will be an average exchanged ratio calculated from ^{1}H NMR, as the dispersity of MPC size will cause variations in the exact number of exchanged ligands on each cluster.[109] With the X-ray diffraction (XRD) identification[131] of staple motifs, which are composed of one Au(I) and two thiolates as part of the capping structure on gold thiolate nanoparticles, place exchange must insert the new thiolate into the existing staples at the same time as the previous thiolate is lost in the S_N2 mechanism. Tiopronin MPCs were co-dissolved in DI

water with free thiolated epitope (1:10). If necessary to aid the solvation of the epitopes into water, the epitopes were first dissolved into ethanol. The place exchange reaction took only one night for the exchange of a single epitope, while requiring three days for the exchange of two epitopes simultaneously. Solutions were dialyzed at room temperature for approximately 3 days as previously described and then dried under air.[120] Place exchange was performed by S. A. Miller. The epitope composition of the MPCs was determined by TGA and ^{1}H NMR analysis.

Nuclear Magnetic Resonance

^{1}H NMR experiments were run at 300 MHz on a Bruker DPX-300 instrument with 5 s relaxation times by R. G. Keil. Samples were dissolved in D_2O. The extent of place substitution of tiopronin by epitope on gold nanoparticles was determined by ^{1}H NMR, using methods previously described.[109, 122]

Enzyme-linked immunosorbent assay

Initial tests to determine whether the functionalized nanoparticles were suitable as both a viral simulant and a synthetic calibrant were performed using ELISAs. Positive activity was established by adhering gold nanoparticles (250-500 ng/per well) with a variety of functionalities (Au-Tiop, HA-Au, FLAG-Au, HA-FLAG-Au) to a 96 well Immulon 2HB plate. Buffer and free peptides (25 µg/well) were plated and tested in a similar fashion. Blocking was achieved with BSA (1 mg/mL) followed by exposure to either anti-FLAG or anti-HA primary antibodies (at recommended dilutions, monoclonal mouse). Horseradish peroxidase linked anti-mouse antibodies (1:5000 dilution) were then added,

followed by exposure to tetramethylbenzidine (TMB, Sigma) substrate solution. The reaction was halted with 2 M H_2SO_4 and the plates were read at 450 nm (BioTek Synergy HT plate reader). ELISAs were performed by S. A. Miller.

Immunosensor Assembly

The immunosensor was assembled on a 5 MHz AT-cut quartz crystal. Before assembly, the gold electrode was triple cleaned in piranha and then rinsed in ethanol or acetone rinse and dried in a stream of N_2 (g). The quartz crystal was then mounted in a flow cell holder, rinsed with phosphate buffer (PB, 50 mM phosphate, pH 7.2) and brought to resonant frequency at room temperature. For the work described herein, a Stanford Research Systems quartz crystal microbalance model 200, which measures both frequency and resistance, was used. Solutions were passed through the cell at a flow rate of 28 µL/min controlled by a Masterflex peristaltic pump. The sequence for biosensor assembly was: Protein G (20 µg/mL, 10 min), BSA (1 mg/mL, 5 min), antibody (20 µg/mL, 16 min), and viral simulant (500 µg/mL, 11 min) all in PB. The nanoparticles were filtered prior to use with a 0.22 µm filter from Millipore. The crystal was washed for a minimum of 10 minutes with PB between each step. Deposition of Protein G allowed for the immobilization of the Fc region of anti-HA and anti-FLAG antibodies. The binding of non-functionalized Au-tio nanoparticles (500 µg/mL, 11 min) with anti-HA antibodies was used as a negative control and as a test for non-specific binding. Positive control was established utilizing anti-HA's recognition of recombinant H5 HA protein (5 µg/mL, 10 min).

The adsorbance of each of these molecules resulted in changes in both frequency and resistance. The bound analyte mass is proportional to changes in the oscillation frequency of the quartz crystal as described by the original Sauerbrey equation (Eq. 17), where Δf is the change in frequency, C_f is the known sensitivity factor of a 5 MHz crystal (56.6 Hz cm^2 μg^{-1}), and Δm is the change in mass.[132]

$$\Delta f = C_f \Delta m \qquad \text{(Eq. 17)}$$

In addition to mass, the frequency of the crystal is also dependent on the density and viscosity of the contact medium, a consequence of the solution's resistance to crystal oscillation.[133] The crystal frequency and resistance were recorded during the QCM experiments to allow for corrections to be made for solution resistance, following the work of Kanazawa and Martin,[134-136] which modifies the standard Sauerbrey equation to

$$\Delta f_{Mass\ Load} = \Delta f_{Measured} + \Delta f_{Resistance} = -C_f \Delta m \qquad \text{(Eq. 18)}$$

This equation demonstrates the changes in mass load that arise from changes in viscosity, changes that were noted in Equation 15. Frequency change for solution resistance is nominally -2.464 Hz/Ω given an active crystal surface area equal to 0.40 cm^2, per sucrose calibrations similar to work reported previously.[123] This number is slightly different than the number reported in Chapter 2, -2.2 Hz/Ω. These differences arise from different manufacturers of the crystals and of the QCMs, either SRS or Maxtek. SRS crystals and instrumentation were used in this chapter to attain this correction factor, while Maxtek crystals and instrumentation were used to attain the correction factor in chapter 2. In both instances, the error is approximately 0.2 Hz/Ω, making the correction factors essentially the same. The resulting change in mass is

therefore a combination of changes in resistance and frequency, while taking into account solution resistance. The QCM results corroborated results from the ELISAs.

RESULTS AND DISCUSSION

In the development of a synthetic positive control for this influenza immunoassay, functionalized gold MPCs were synthesized and characterized. TEM analysis of the tiopronin–gold nanoparticles (Au-tiop) was performed by R. G. Keil and B. N. Turner and resulted in an average cluster size of 2.6 ± 0.6 nm, with a range from 1.5 to 4 nm. The TGA tiopronin MPC mass loss equaled 37.9% and yielded a 2.67 Au:Tiop stoichiometric ratio for the nanoparticles assuming the loss of the Au(I)-thiolate staples. The assumption of the loss of the Au(I) thiolate staples is justified by the observation of gold-thiolate compounds upon thermal decomposition in a mass spectrometer.[137] The average number of gold atoms calculated per cluster equaled 544 atoms. Combining the TEM and TGA yields a calculated empirical formula $Au_{544}Tiop_{204}$ for the 2.6 nm diameter particle. Following place exchange of epitope(s) for tiopronin, the epitope loading was determined through ^{1}H NMR. The epitopes HA and FLAG each contain an exclusive amino acid whose proton signal occurs at a unique location in the ^{1}H NMR spectrum. Specifically, valine (V) is unique to the FLAG epitope and lysine (K) to the HA epitope. Tyrosine (Y) is common to both epitopes, but occurs in different stoichiometric ratios. The integrated resonance for each functionalized nanoparticle can be compared with that for nanoparticles protected solely with tiopronin to determine the average epitope stoichiometry of the nanoparticles. Peaks used for quantification consisted of signals at 1.2 ppm (V, 2 CH_3), 1.45 ppm (tiopronin, CH_3), 2.90 ppm (K, 2 ε-

CH_2), 6.75 ppm (Y, δ-CH) and 7.05 ppm (Y, ε-CH). The ^{1}H NMR data allowed for the nanoparticle stoichiometry to be calculated. The HA and FLAG epitope compositions and molecular weight are: (a) $Au_{544}Tiop_{153}FLAG_{30}HA_{22}$, 210.0 kDa (b) $Au_{544}Tiop_{191}HA_{13}$, 158.6 kDa and (c) $Au_{544}Tiop_{190}FLAG_{14}$, 158.5 kDa.

The ELISA results confirmed specificity of the functionalized gold nanoparticles to the anti-HA and anti-FLAG antibodies (Figure 11). Evidence of cross reactivity between the gold nanoparticles presenting both peptides and both antibodies corroborates with QCM data. HA-FLAG-Au and FLAG-Au were detected with the anti-FLAG antibodies, while HA peptides and HA-Au were not. Correspondingly, HA peptides HA-Au, and HA-FLAG-Au were recognized by anti-HA, while FLAG-Au was not. The limit of detection (LOD) was calculated to be 0.146 O.D. using the average absorbance of wells incorporating buffer only in the initial step, which served as a negative control. The gold particles displaying only tiopronin (Au-Tiopronin) appeared to non-specifically bind with anti-HA. Non-specific binding could be reduced in ELISAs with the use of higher concentrations of BSA or with the use of more stringent rinsing protocols, such as the use of a non-ionic surfactant Tween 20 between steps, which might also remove bound particles and lower the sensitivity of these assays.[138] MPCs functionalized without the PEG linker between the epitope and the cysteine linkage showed no binding with their respective antibodies in either ELISA or QCM experiments, but once the PEG link was incorporated into the mimic's designs, the antibodies were able to bind with the epitope functionalized nanoparticles. Calculations using Spartan computational software show the spatial projection of tiopronin molecules to be about 7 Å from the gold surface, and the peptides, due to the PEG addition, extend 20 Å, from the gold surface.[139] The addition

of the six-mer PEG link between the epitope and the terminal cysteine enhanced the probability for cluster-epitope interaction with antibody by distancing the epitope from the gold surface. This enhanced binding was demonstrated with both ELISA and QCM studies.

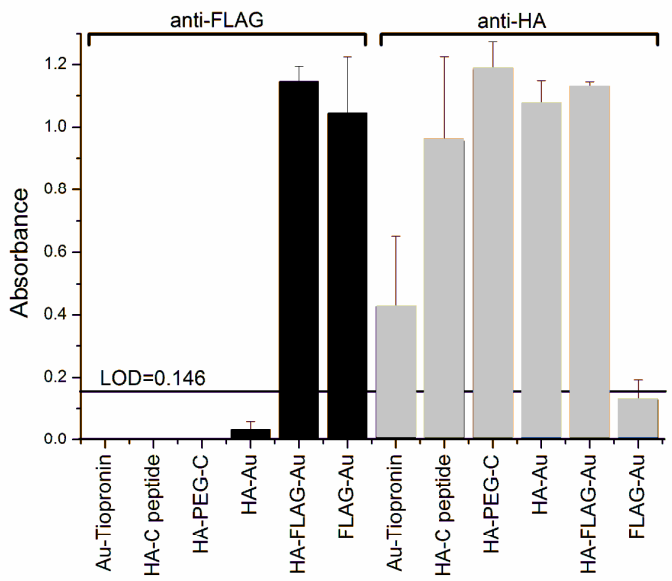

Figure 11. ELISA indicating the interactions of peptides and functionalized gold nanoparticles with FLAG and HA antibodies. Results demonstrate normal and orthogonal antigen-antibody binding. (n=3 for all data points, absorbance at 450 nm). ELISA ran by S.A. Miller, with calculations performed by L. A. Hiatt.

Several observations can be made by inspection of the QCM responses (Figure 12, recorded data and schematic of adsorption) during sensor formation. Both antibodies are found to bind well to Protein G. Observed spikes during assembly occur when reagent flowing through the peristaltic pump is momentarily interrupted for reactant exchange. A time delay (1-2 minutes) between spike and sensor response was due to the requisite transport time for the analyte to move through the peristaltic pump to the QCM sensor.

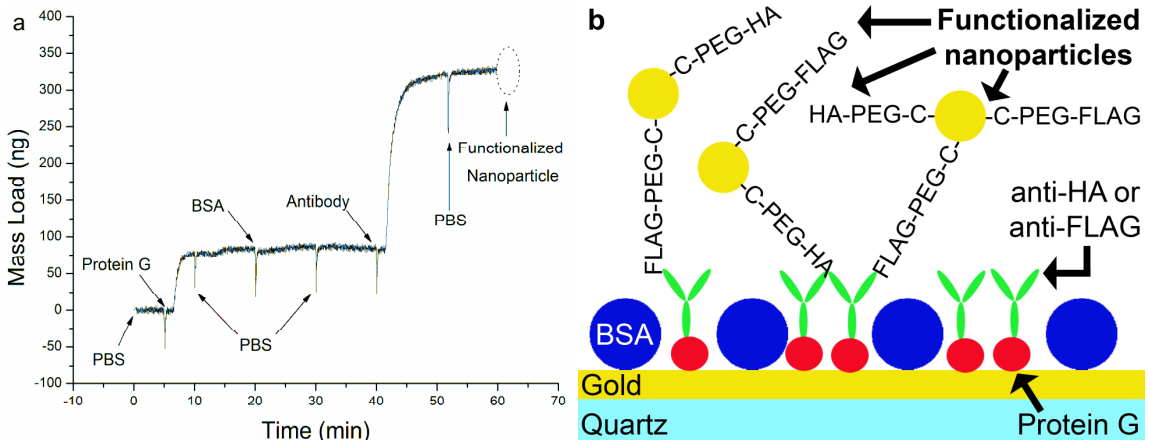

Figure 12. (a) QCM immunosensor assembly sequence for H5N1is recorded. Solutions are pumped over the crystal in this order: Protein G, bovine serum albumin (BSA), antibody (HA or FLAG). The binding of these three proteins constitutes the development of the immunosensor. The next step is not shown (Figure 12), but instead is depicted with a circle. The binding of a functionalized nanoparticle or H5N1 HA protein would be introduced to the sensor next and binding would be measured Phosphate buffer (PB, pH 7.2) flows at the beginning of each experiment and between additions as indicated to establish and re-establish baseline levels. This figure is a representative experiment showing the typical binding seen during the course of an experiment. (b) A schematic of the binding occurring on the sensor is shown. Refer to Table 2 to see average binding for all experiments.

The change in mass measured with the QCM is indicative of the binding of the nanoparticles and the HA protein to the HA-antibody (Figure 13A) and to the FLAG-antibody (Figure 13B). Detection of the HA protein confirms the ability of this assay to detect hemagglutinin specific to the H5 HA subtype, and thus the use of this HA functionalized nanoparticle as a viral simulant. This change in mass is based on the relationship that changes in both frequency and resistance have on mass load. Originally the Sauerbrey equation was applied in air or in a vacuum and the resulting equation was only valid for thin solid layers deposited on the resonator.[140] Since then extensive work has been done to establish the use of the QCM to probe interactions in a liquid environment, involving suitable oscillator circuits, fluid modeling in viscous and lossy

fluids, as well as determination of the relationship between motional resistance and mass load.[12, 42, 136] The sensing layers utilized in this study should yield at most a layer 30 nm thick, using liberal estimates, where the Sauerbrey equation can be applicable to thin films less than 250 nm.[77, 78, 89, 141] Previous work, which uses a sucrose calibration, modifies the Sauerbrey equation to account for the changes that do occur in part from motional resistance, and therefore allows the ideology behind the Sauerbrey equation to apply in environments where energy is dissipated in the non-rigid liquid environment.[121] The nanoparticles increase the resistance of the crystals, and thus the rigidity, as well as decreased the frequency, resulting in a detectable increase of mass adsorbed on the surface of the crystal. Binding to the HA-antibody (positive Δm) occurs if the gold nanoparticle is functionalized with either HA or both HA and FLAG epitopes, but does not occur if the cluster is only FLAG functionalized (Figure 13A). The non-specific binding observed with ELISA of Au-Tiopronin to anti-HA was not observed with the QCM. QCM naturally prohibits non-specific binding through the acceleration of adhered particles. This acceleration is generated by the oscillation of the quartz and can help remove weakly bound or non-specifically bound molecules.[142, 143] Similar binding of anti-FLAG to FLAG-Au and HA-Au-FLAG but not HA-Au was measured with the QCM (Figure 13B). Thus, orthogonal and normalized binding at the QCM is observed consistent with immunological results obtained from ELISA, but is observable in a much shorter time interval (10 minutes compared to the 4 hours it took to complete the ELISAs) when using the developed immunoassay and the QCM.

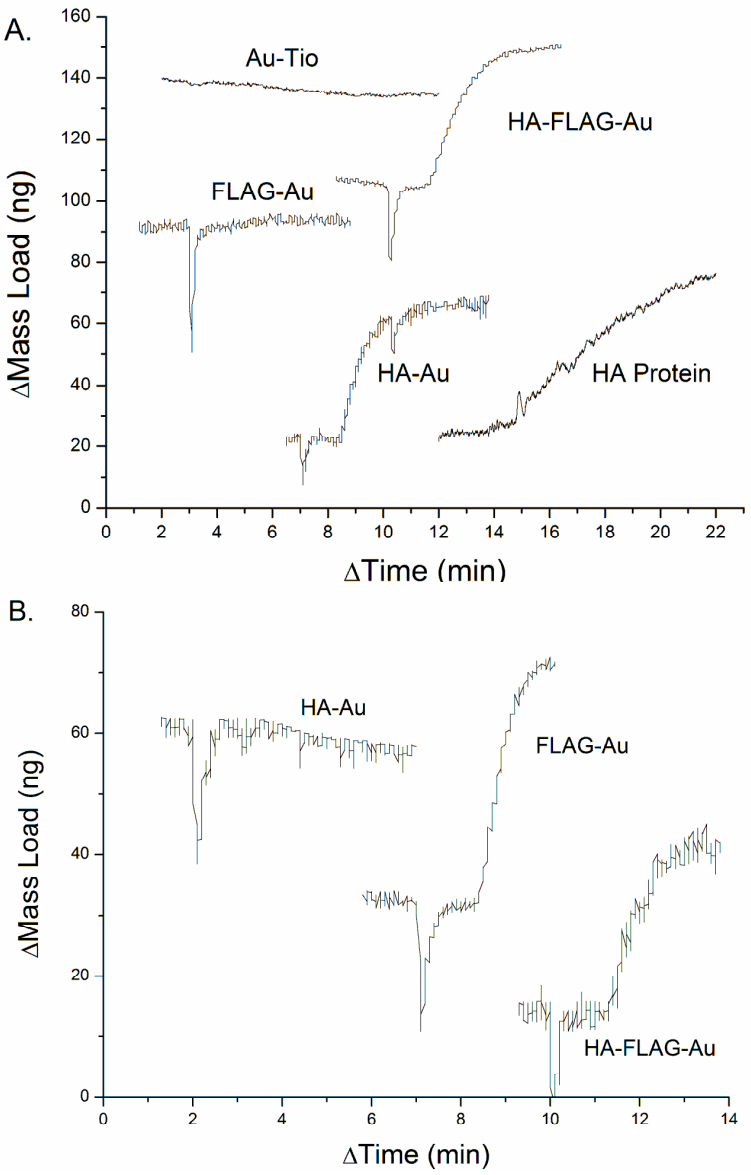

Figure 13. Functionalized gold MPC binding measured with a QCM. Response to functionalized gold nanoparticles at room temperature from eight different experiments is shown. The data was normalized in time and in mass load, keeping the relative changes the same as the original data, for aesthetic purposes in combining all the data on two graphs. The responses were generated using (A) anti-HA and (B) anti-FLAG antibodies. An increase in mass is indicative of binding which begins with the introduction of nanoparticles bearing the epitope for which the immune responses were generated. Lack of binding to orthogonal particles has been demonstrated through negative controls.

The demonstrated binding between bi-functionalized nanoparticles and their respective antibodies makes evident the practicality of their use as a simulant for microorganisms, while lacking the difficulties associated with use of an attenuated or killed pathogen. When a change in mass is observed upon introduction of the functionalized MPC to the immunosensor, the immunological response is shown to be above the limit of detection (~3 ng, calculated by three times the average noise). Results show the average change in mass for Protein G to be 128 ± 48 ng, for antibodies, 276 ± 75 ng, and for the nanoparticle simulants, 37 ± 8 ng (Table 2). While the time was held constant for each step, the binding varied slightly which could be due to slight variations in surface roughness and the surface coverage of prior adsorption steps. Even with a standard deviation of 75 ng for antibody adsorption, a deviation of only 8 ng was measured for the final detection step.

Table 2. Change in mass detected with the H5N1 immunosensors for the addition of each layer of adsorbed molecules: protein G, antibodies, and epitope functionalized nanoparticles. Average adsorption occurred in 10 min (protein G), 16 min (antibodies), and 11 min (functionalized nanoparticles). *Denotes average and standard deviation determined without including the negative controls.

	Calculated Change in Mass		
	Protein-G	Antibody	Nanoparticle
Antibody, Nanoparticle	**(ng)**	**(ng)**	**(ng)**
Anti-FLAG, FLAG-Au	100	270	30
Anti-FLAG, FLAG-Au	150	300	40
Anti-FLAG, FLAG-Au	80	270	30
Anti-HA, HA-Au	170	120	30
Anti-HA, HA-Au	60	180	50
Anti-HA, HA-Au	110	280	40
Anti-FLAG, HA-FLAG-Au	170	370	50
Anti-FLAG, HA-FLAG-Au	180	280	30
Anti-FLAG, HA-FLAG-Au	70	220	30
Anti-HA, HA-FLAG-Au	220	430	30
Anti-HA, HA-FLAG-Au	140	290	40
Anti-HA, HA-FLAG-Au	140	270	40
(Negative Controls)			
Anti-FLAG, HA-Au	130	320	0
Anti-HA, FLAG-Au	70	260	0
Average	128	276	37*
Standard Deviation	48	75	8*

The binding of the nanoparticles demonstrates saturation behavior (Figure 13). Based on the shape of the QCM curves and the rapid increase in mass with time, it can be assumed that the kinetics would occur quickly and with presumably large equilibrium association constants. To test this theory, a calibration of anti-HA to HA binding was determined and the binding of the functionalized nanoparticles was compared. The HA protein from H5N1 was exposed to anti-HA antibodies at concentrations ranging from 1 to 40 µg/mL (Figure 14A and B). This binding can be compared at any time point to generate a calibration curve (Figure 14C, example shown is at 1.5 min). Based upon the

desired separation of the lower data points, the binding can continue for several more minutes. Also, the amount of nanoparticle exposed to the surface can be lowered to prevent overloading of the sensor.

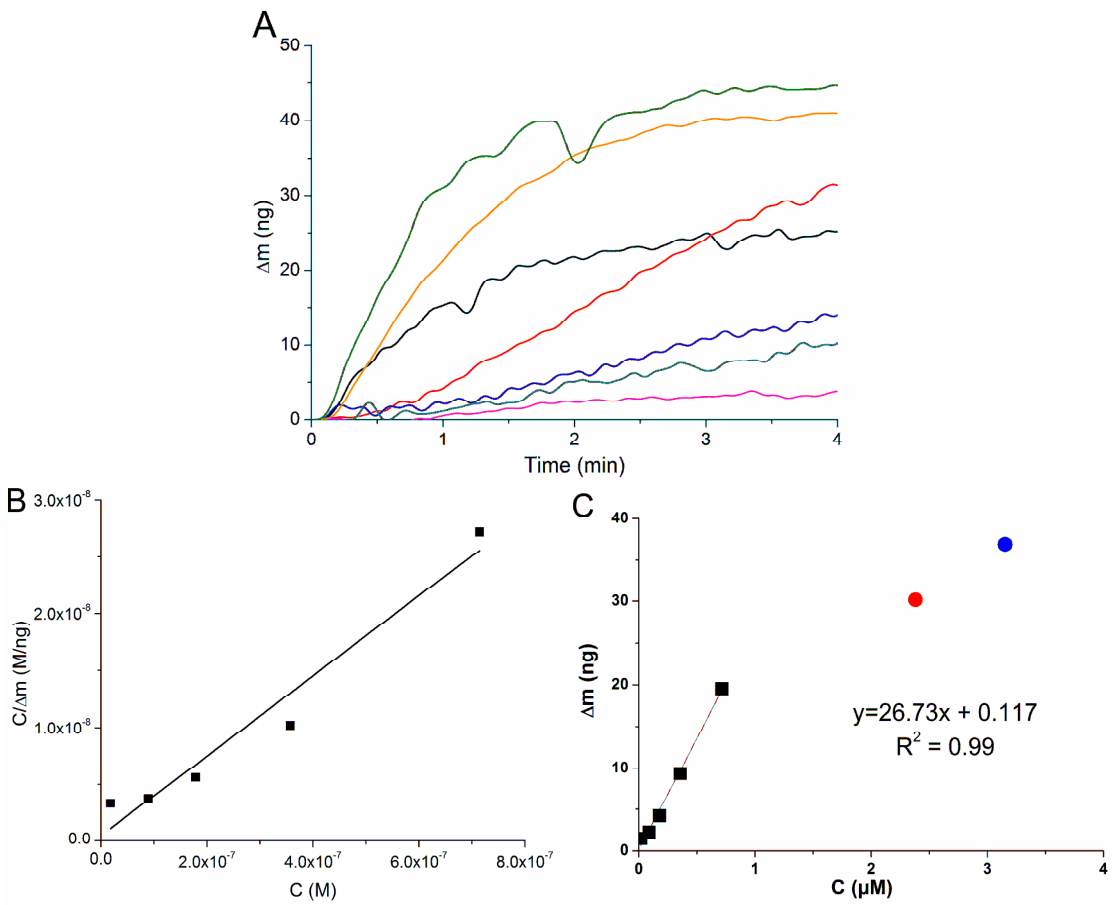

Figure 14. Calibration of HA protein binding to anti-HA. (A) The average change in mass of H5N1 HA protein binding was determined at varying concentrations. Briefly, (—) 40 µg/mL (n=2), (—) 20 µg/mL (n=5), (—) 10 µg/mL (n=3), (—) 5 µg/mL (n=3), and (—) 1 µg/mL (n=4). Also shown for comparison is the binding of HA-Au (—) and HA-FLAG-Au (—).(B) A linear representation of the Langmuir isotherm produced by this average binding is shown with a linear relationship of $y=(0.035\pm0.004)x+(4.90\pm15.5)*10^{-10}$ and $R^2=0.96$. (C) Calibration curve for an assay time of 1.5 minutes where the black squares are HA proteins and the red and blue dots are HA-FLAG-Au and HA-FLAG respectively.

Measuring the maximum binding that occurs, as opposed to at lower time points, can be used to determine the equilibrium association constant (K_a) and increase our understanding of the affinity of our sensor. This constant was determined by fitting the experimental data to a linear rearrangement of the Langmuir adsorption isotherm, where C was plotted versus C/Δm (Eq. 5, Figure 14B).[121]

This yielded an equilibrium association constant for the binding between the HA protein and anti-HA of $7.14 \pm 0.26 \times 10^7$ M^{-1}. This K_a is in the range expected for antibody-antigen interactions, from 10^6-10^{10} M^{-1}.[96] In fitting the binding of the nanoparticles to this Langmuir isotherm calibration (at the experimentally used nanoparticle concentration of 500 μg/mL), the sensor response to HA-FLAG-Au would have the same binding as 0.92 ± 0.01 μM HA protein and HA-Au would generate the same sensor response as 1.50 ± 0.02 μM HA protein. The large response seen is at the maximum of the Langmuir isotherm. This demonstrates that even at lower concentrations, these functionalized nanoparticles can be used as a positive control. The functionalized MPC-antibody binding is not inhibited by the presence of an additional non-interacting epitope (either FLAG or HA) on the poly-functionalized nanoparticle; therefore, multiple binding interactions can be explored simultaneously.

CONCLUSIONS

The ability to create multi-epitope presenting nanoparticles that can orthogonally bind to specific monoclonal antibodies has been demonstrated using both ELISA and immunological QCM. Determination of the extent of antibody-functionalized nanoparticle binding using the QCM is rapid compared to ELISA. Also, like ELISA, the

immunological response is specific, with QCM incurring little non-specific binding. Interaction of the epitope with its antibody was improved through the use of a PEG linkage for epitope attachment to the MPC. Binding studies at the QCM show that poly-functionalized gold nanoparticles exhibit the expected affinity to both antibodies, that a normal immunological response is achieved from matched antibody-antigen couples, and that an orthogonal response results otherwise. The results demonstrate that binding of poly-functionalized gold nanoparticles could be used to determine sensor functionality, without resorting to the use of attenuated or killed microorganisms or extracted and purified whole proteins.

ACKNOWLEDGEMENTS

The authors acknowledge support from NIH grant R01 GM076479 and DTRA HDTRA1-10-0067. L. A. Hiatt acknowledges support from a Department of Education GAANN Fellowship (P200A040022) and QCM training from R. G. Keil. R. G. Keil acknowledges sabbatical leave support received from the University of Dayton and Vanderbilt University. We thank B. N. Turner for his assistance in TEM and TGA data collection.

CHAPTER IV

SUPEROXIDE DISMUTASE COATED ELECTRODE FOR THE STUDY OF MACROPHAGE OXIDATIVE BURST

Reactive oxygen species (ROS) produced by macrophages assist in the elimination of foreign particles and bacteria. However, some bacteria, such as tuberculosis through lipoarabinomannan,[144] have developed means through which they evade this mechanism of macrophage defenses. Basal production of ROS by NADPH oxidase in the macrophage cell is low, but is increased to degrade pathogens in what is termed oxidative burst.[145, 146] Deviations from normal levels of ROS or ROS scavenging can lead to macrophage damage, cell death, or the impairment of cell proliferation and host responses.[147, 148] Dynamic quantitative assay of ROS production would further the understanding of the immunological consequences of macrophage exposure to tuberculosis or lipoarabinomannan.

Reactive oxygen species are highly unstable which makes them difficult to analyze directly.[149, 150] Traditionally, oxidative burst is detected by measuring hydrogen peroxide, the hydroxyl radical, or reactive nitrogen species (RNS), as these species are the most stable and readily diffusible candidates for describing the chemical cell response. In oxidative burst, production of superoxide (O_2^-) and nitric oxide radicals generate the remainder of the molecules produced in an oxidative burst, *i.e.,* hydrogen peroxide, peroxynitrite and the nitrite ion. High intracellular concentration of O_2^- can have detrimental effects on a cell. Several means of O_2^- dismutation are present *in vivo*, including the spontaneous dismutation of O_2^- with water (10^5 M^{-1} s^{-1})[151] to limit the

cellular concentration of this analyte and prevent cellular damage.[152] Superoxide can also form other molecular species through dismutation *via* superoxide dismutase (SOD, ~$2x10^9$ M^{-1} s^{-1})[149, 150] or through its interaction with RNS which can sometimes outcompete SOD (~10^{10} $M^{-1}s^{-1}$)[150]. Since hydrogen peroxide is more stable than O_2^-, it is present at higher concentrations in culture.[152, 153] Detection methods must be specific and sensitive enough to differentiate between each reaction product to accurately study oxidative burst.[154] Measuring O_2^-, instead of one of its byproducts, will differentiate oxidative burst from other pathways that might also generate hydrogen peroxide.

Previous work has been performed by the lab of Christian Amatore to improve the detection of ROS and RNS where the concentrations of H_2O_2, $ONOO^-$, $NO^\bullet$ and NO_2^- were determined using amperometry at varying potentials and through the subtraction of peak heights to identify each reactive species.[155, 156] The Amatore group has used mechanical depolarization, calcium ionophores, phorbol 12-myristate 13-acetate (PMA) and interferon-γ/ lipopolysaccharides to stimulate macrophages and induce oxidative burst for measurements at the single cell level using platinized carbon-fiber ultra-microelectrodes (UMEs).[155, 157, 158] They further advanced single cell measurements using chronoamperometry at multiple potentials to assess the time release of each of these reactive species.[156] Electrochemical measurements were verified with the use of UV-Vis in the presence of a natural detoxification molecule, ascorbic acid, to show end-point product formation.[153] In order to determine meaningful statistical relationships among cellular responses and controls, single cell measurements cannot be used for comparisons since they are not indicative of a complete cellular environment.[156]

Further work has expanded on the detection of ROS through the incorporation of immobilized protein films into electrochemical sensors. Cytochrome c has been utilized for the detection of superoxide on gold electrodes due to its role as a natural antioxidant and its ability to be reoxidized by the electrode at a suitable potential.[159, 160] Cytochrome c reacts with O_2^- at a reaction rate of $1.4x10^9$ M^{-1} s^{-1}. When a cytochrome c electrode was placed into a solution with O_2^-, an increase in current was seen. This change in current was completely depressed with the addition of SOD to the solution,[159] since SOD can outcompete cytochrome c with its faster reaction rate, $2x10^9$ M^{-1} s^{-1}.[149] SOD has previously been immobile on electrochemical sensors and improvement on and further characterization of this enzymatic electrode is needed to understand its mechanism of O_2^- detection.[149, 161]

Ink-jet printing is one way to improve reproducibility and enzyme deposition for an O_2^- sensor. There is a growing interest in ink-jet printing due to its reproducibility in rapid, small-scale fabrication.[162-164] While many contact/non-contact deposition techniques exist, this study compares hand-casting with printing of the SOD enzyme film. If printing of the enzyme can be achieved with limited loss in enzymatic activity, a uniform and better controlled enzymatic film can be produced and the difficult process of immobilizing distinct enzymes on different parts of an electrode array can be overcome.[20, 21] Utilizing a screen printed electrode (SPE) for these studies will serve as a reliable platform for comparing enzyme depositions.

Due to the short, concentration-dependent lifetime of O_2^- in protic solvents, the detection and characterization of reactive oxygen intermediates (ROIs) must occur on the time order of the reaction, making an electrochemical study difficult.[165] The $O_2/O_2^{\bullet-}$

couple has been studied with bare electrodes in dipolar aprotic solvents containing tetra-alkyl ammonium salts.[166] The tetrabutylammonium cation in aprotic solvents stabilizes the superoxide ion through solvation or ion pair formation.[167] At high scan rates the electron transfer from superoxide to the electrode can compete with its chemical destruction.[166] A similar system, involving the proton transfer behavior of quinines, was studied in aprotic solvents to determine reaction intermediates and can be used as an example for studying superoxide behavior.[168] Studying the electron transfer in non-aqueous solvents leads to better understanding of the reactions occurring at the electrode, which in turn can lead to important insights not attainable under biological conditions.[165]

Studies of the $O_2/O_2^{\bullet-}$ couple have been carried out in dimethylformamide (DMF), dimethyl sulfoxide (DMSO), and acetonitrile (ACN).[165-167, 169-171] Each solvent system has its own advantages. The formal potential for the $O_2/O_2^{\bullet-}$ couple is typically in the range of -0.73 and -0.80 V vs. a SCE reference electrode.[169] Reversibility of this couple has been achieved in DMSO, DMF, and ACN, with DMSO having the best peak separation. Peroxide can be produced at an even more negative potential.[167] It has been proposed that the $O_2/O_2^{\bullet-}$ couple in the presence of an acid has a ECE reaction mechanism where "E" represents an electron transfer at the electrode surface and "C" is a homogeneous chemical reaction.[172] In this case, for example, O_2^- is formed, protonated by the acid in solution, and then reduced at the electrode surface (ECE, Eqs. 19-21).[165] The chemical step determines reversibility. When acid is not present, the reaction proceeds as a simple "E" mechanism as shown by Equation 19. Understanding of this couple on a Pt electrode will provide a good comparison for determining the electrode

mechanism of a SOD coated electrode. Dismutation of O_2^- by SOD is generally accepted to be a proton-coupled electron transfer (Eqs. 22-23).[173]

$$O_2 + e^- \rightleftarrows O_2^{\bullet -} \quad \text{(Eq. 19)}$$

$$O_2^{\bullet -} + HA \rightleftarrows HO_2^{\bullet} + A^- \quad \text{(Eq. 20)}$$

$$HO_2^{\bullet} + e^- \rightleftarrows HO_2^- \quad \text{(Eq. 21)}$$

$$Cu^{2+}SOD + O_2^{\bullet -} \rightarrow Cu^{+}SOD + O_2 \quad \text{(Eq. 22)}$$

$$Cu^{+}SOD + O_2^{\bullet -} + 2H^+ \rightarrow Cu^{2+}SOD + H_2O_2 \quad \text{(Eq. 23)}$$

The detection of superoxide at SOD in multiple solvent systems will increase the understanding of the reaction mechanism and the requirements of the proton donor. Proton transfer in aprotic solvents requires a proton donor from a weak acid instead of a strong acid, due to the substantial water content in strong acids.[168] In this study xanthine oxidase was used to convert hypoxanthine to uric acid (pK_a=5.8), which produces two molar equivalents of superoxide and was used to produce O_2^- for calibration of SOD electrode in PBS.[149, 174, 175] This enzymatic system has been used to generate superoxide in protic solvents.[149] This enzymatic system has not been used in aprotic solvents due to limited solubility. Potassium superoxide is used to generate O_2^- in aprotic solvents, while xanthine oxidase is used in aromatic and protic solvents where it was more soluble.

Superoxide production can be confirmed using UV-Vis spectrophotometry. [171, 176] To increase solubility, and therefore O_2^- production, the SOD electrode mechanisms were also studied in *p*-xylene. Aromatic hydrocarbons have rarely been used in electrochemistry due to the limited solubility of suitable electrolytes.[177] Previous electrochemical studies in aromatic hydrocarbons utilize ultramicroelectrodes (UMEs), lithium dodecamethylcarba-*closo*-dodecaborate as an electrolyte, or a mixture with methanol to overcome the high solution resistance.[177, 178] In this work,

tributylhexadecylphosphonium bromide was used as an electrolyte in *p*-xylene. This electrochemical study of a SOD electrode in a protic, an aprotic, and an aromatic solvent was utilized to characterize and understand the reactions occurring at the electrode interface.

EXPERIMENTAL

Materials and Instrumentation

Superoxide dismutase (SOD, Bovine with Cu/Zn reaction centers[179]), xanthine oxidase (XOD, Bovine), and bovine serum albumin (BSA) were purchased from Sigma Aldrich. Hypoxanthine disodium salt (HPX) was purchased from MP Biomedicals LLC. Glutaraldehyde (GA, 25% in water) was purchased from Acros Organics. Dimethyl sulfoxide (DMSO) and all other solvents were purchased from Fisher Scientific Company, LLC. Ag/Ag+ reference electrodes were purchased from CH Instruments, Inc.

Custom designed (J. R. McKenzie) screen-printed platinum electrodes (SPE) were obtained from Pine Research Instrumentation. The SPEs utilized consisted of three layers: a ceramic substrate, screen printed platinum, and an insulating layer covering the entire chip except for the areas needed for electrochemical detection, such as contact areas and electrodes. Each chip has 5 electrodes: three Pt 1.8 mm^2 disk electrodes, one Pt 0.08 mm^2 bar electrode, and one Pt 19 mm^2 rectangular counter electrode.

Amperometric experiments were attained using a Vanderbilt Institute for Integrative Biosystems Research (VIIBRE) multichannel multipotentiostat at a potential of +0.6 V vs. Ag/AgCl.[180] Voltammetric measurements (linear sweep voltammetry (LSV), cyclic voltammetry (CV), or open circuit potential (OCP) experiments) were attained using a

CHI 660a potentiostat from CH Instruments with a picoamp booster and faraday cage. Enzymes were printed with a Fujifilm Dimatix, Inc. Materials Printer. The maximum voltage used was 25.0 V, and the frequency of the pulses was maintained at 23 kHz. Spot spacing was kept uniform at 45 μm over a square print area of 2 mm^2.

UV/Vis measurements were taken in a 1.4 mL quartz Spectrocell cuvette (path length of 1 cm) and recorded with a Cary 100 BioSpectrophotometer. The absorbance of solutions of XOD, HPX, xanthine (XAN), and uric acid (UA) in phosphate buffer saline (PBS, 100 mM KCl, pH 7.2) or p-xylene were all taken at a concentration of 0.2 μM. The absorbance of the mixture of HPX with XOD was taken at concentrations of 0.1 and 0.2 μM respectively.

Enzymatic Sensor Fabrication

SOD films were cast onto the SPEs using one of two methods: hand-cast or ink-jet printing. For the hand-cast method, BSA was dissolved in phosphate buffer at a concentration of 62 mg/mL. SOD was then dissolved in the PB-BSA solution at a concentration of 5000 U SOD/mL PB-BSA. GA was then added to the solution at a concentration of 1 μL GA/250 μL PB-BSA. Finally, the solution was hand-cast using a pipette tip onto each of the 1.8 mm^2 disk electrodes and allowed to dry.[181]

For the ink-jet printing method, the SOD-PB-BSA solution was made at the same concentrations as the hand-cast solution. This solution was added to the ink-jet cartridge (10 pL print volume, Fujifilm Dimatix, Inc.). Instead of mixing the SOD PB-BSA solution with GA where it would immediately begin crosslinking, a solution of 1% GA in water was prepared in another cartridge. The SOD solution was printed first, followed by

the GA solution. After drying, both hand-cast and printed electrodes were stored in PBS at 20 °C.

Solvent Conditions

Phosphate buffer saline (PBS) was prepared with 50 mM phosphate and 100 mM KCl at pH 7.2. DMSO was prepared with 100 mM tetrabutylammonium perchlorate (TBAP) as the electrolyte. The electrolyte utilized in all electrochemical experiments involving *p*-xylene was 100 mM tributylhexadecylphosphonium bromide (TBHDPBr). All experiments were conducted with a platinum mesh counter electrode. PBS experiments utilized a Ag/AgCl (2 M KCl) reference electrode while aprotic and aromatic experiments utilized a Ag/Ag+ anhydrous reference.

Superoxide Production and Sensor Calibration

Superoxide was produced *via* the reaction of xanthine oxidase (XOD, 0.1 µM at 0.6 U/mg) with hypoxanthine disodium salt (HPX, 1-6 µM) in bulk PBS and *p*-xylene solutions.[149, 174, 175] HPX is enzymatically oxidized to xanthine, which can be further oxidized to yield uric acid (Figure 15). The concentrations used in these calibrations are much lower than the saturation behavior of bovine erythrocyte SOD, 0.21 mM $O_2^{\bullet -}$.[182] These enzymatic processes produce two superoxide radicals for every oxidation event. These radicals are then oxidized by SOD to generate a current at the electrode. In DMSO, KO_2 was used to generate superoxide.

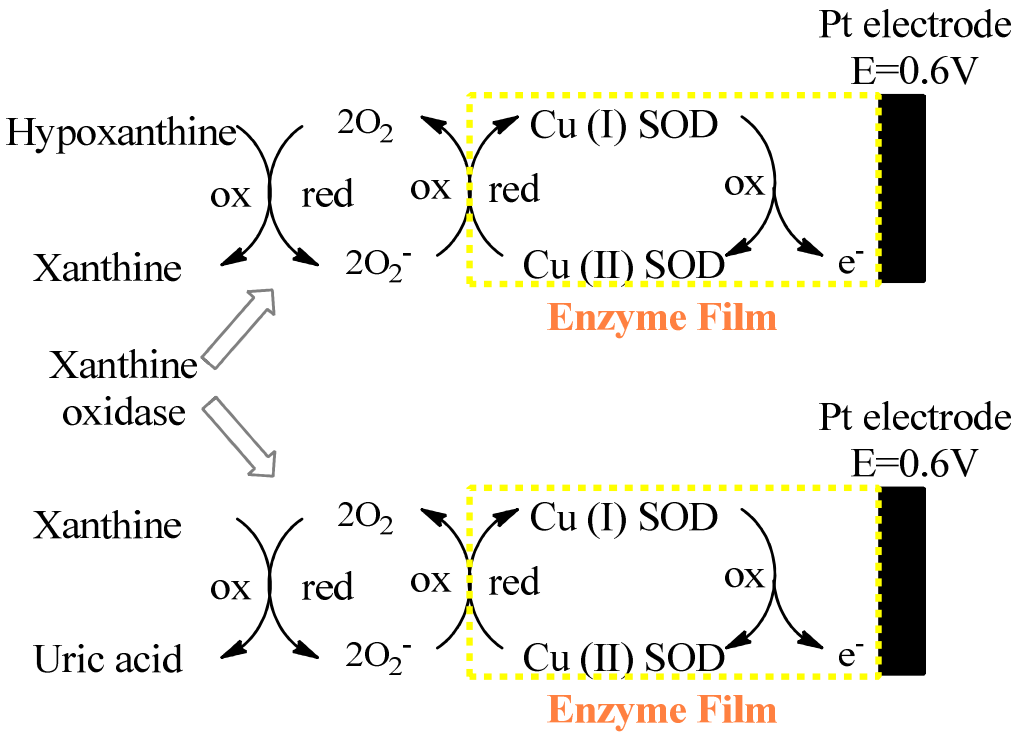

Figure 15. The enzymatic oxidation of hypoxanthine to uric acid utilized in the calibration of the SOD enzyme film.

RESULTS AND DISCUSSION

The SOD films were studied and characterized using cyclic voltammetry and amperometry. A standard redox couple, potassium ferricyanide, was used to determine if the SPE was introducing resistance that might prevent reversible electron transfer (Figure 16). While slight variations in peak separation (ΔE_p) were seen at higher scan rates, the average ΔE_p was calculated to be 72 mV at a scan rate (υ) of 5 mV/s. The ratio of peak currents (i_{pa}/i_{pc}, anodic and cathodic respectively) had a mean value of 0.83, indicating almost equivalent anodic and cathodic peaks. With the combination of these two measurements, the ferricyanide redox couple is reversible or quasi-reversible under these

conditions. This conclusion is also supported by the linear trend seen between i_p and $\upsilon^{1/2}$(Figure 16).

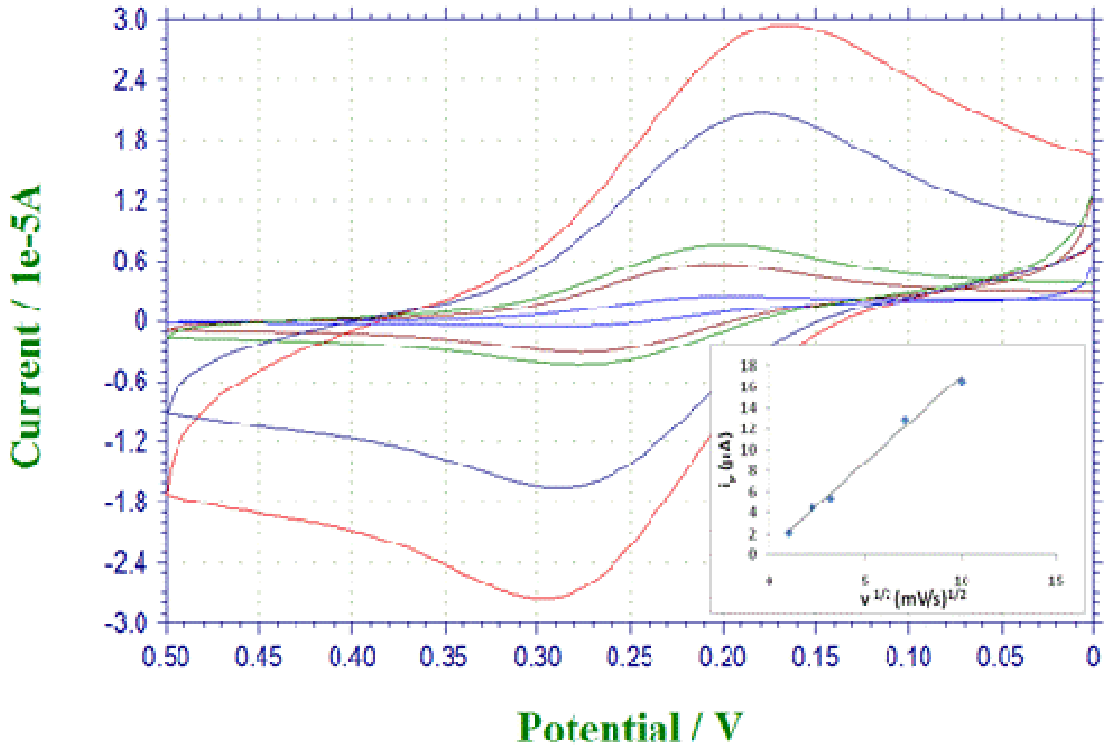

Figure 16. CVs of potassium ferricyanide in PBS (5 mM ferricyanide, 100 mM KCl) with different scan rates (1, 5, 10, 50, and 100 mV/s). The peak separation was calculated to be 72 mV (5 mV/s) and the ratio of peak currents had a mean value of 0.83, yielding a reversible system. Inset: plot of peak current *vs.* scan rate ($y = 1.629\ x + 0.636$, R^2=0.994).

XOD converted HPX to O_2^- in a bulk PBS solution. Acid-cleaned Pt SPEs and SOD coated electrodes were used to determine any changes in current due to non-specific and specific oxidation of O_2^- at the electrode interface respectively. Background scans were performed and compared with two ROS: H_2O_2 and O_2^- (Figure 17).

Since hydrogen peroxide can also be oxidized at +0.6 V, the selectivity of the electrode for O_2^- as compared with hydrogen peroxide had to be determined. The SOD coated

electrode had a greater oxidative peak at +0.6 V for O_2^- solution as compared with the H_2O_2 solution. Both electrodes detected large increases in reductive current as compared with the increases in oxidative current (Figure 18). This indicates not only the ease at which each electrode can reduce oxygen, as shown in previous studies of the oxygen couple, but also the irreversible behavior exhibited by the lack of symmetry in the two peaks. This irreversible behavior is most likely due to the short half-life of O_2^- in water.[151, 165-167, 169-171] The majority of O_2^- in the solution is oxidized prior to diffusing to the electrode surface, but the introduction of SOD as part of the electrochemical sensor allows higher detection of O_2^- than with a bare Pt electrode.

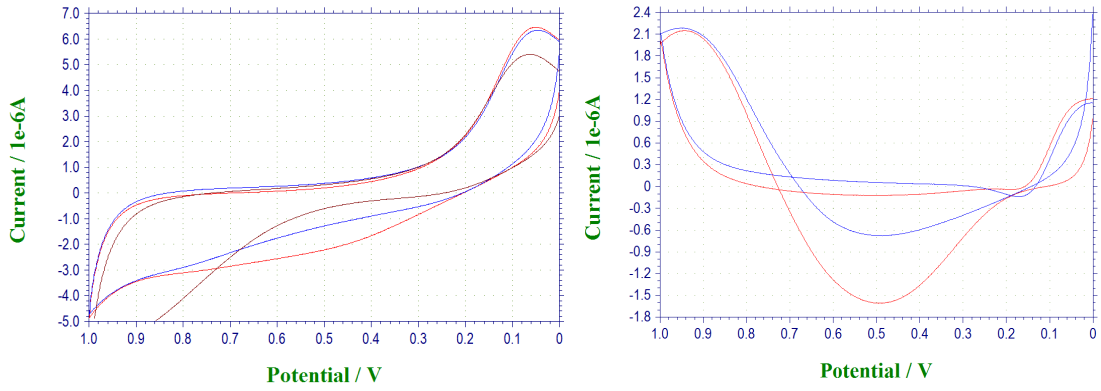

Figure 17. CVs of printed SOD film and the changes in current upon exposure to ROS, H_2O_2 (*blue line*, 1 µM) and $O_2^{-\bullet}$ (*red line*, produced with 1 µM XOD and 100 µM HPX) vs. no ROS (*brown line*) shown on the left. All samples in PB with 100 mM KCl at a scan rate of 20 mV/s. On the right, the PBS background was subtracted to yield net current change for H_2O_2 (*blue line*, 1 µM) and $O_2^{-\bullet}$ (*red line*, produced with 1 µM XOD and 100 µM HPX) with a difference of 0.93 µA at 0.49 V.

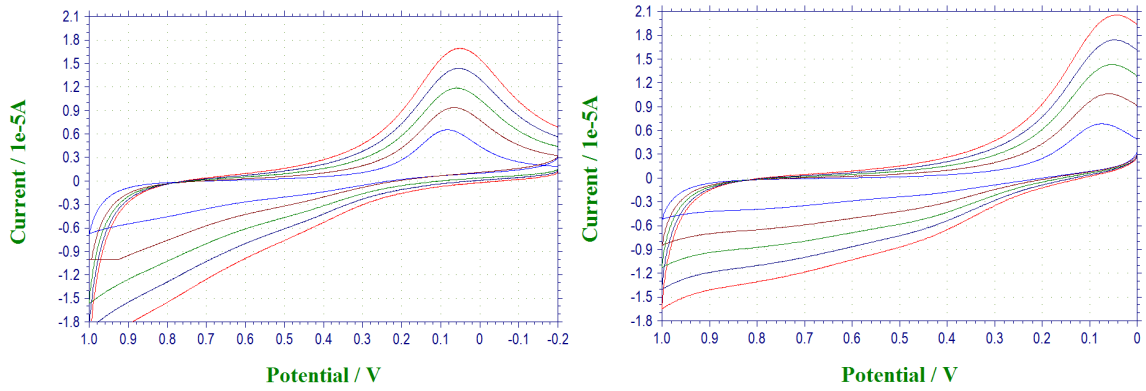

Figure 18. Recorded CVs for bare Pt and SOD coated electrodes (*left and right respectively*) in PB with 100 mM KCl, 1 µM XOD, and 100 µM HPX vs. a Ag/AgCl reference electrode. Oxidation current is seen for the SOD coated electrode at +0.6 V. As the scan rate increases (20, 40, 60, 80, and 100 mV/s noted by the *light blue, brown, green, blue, and red lines*), the oxidation currents and reduction currents increase.

The presence of a preceding reaction mechanism can be determined from the resulting detection of O_2^- in the CVs. The current detected at both electrodes scaled linearly with the square root of the scan rate (Figure 19). In order to determine the number of electrons utilized at each electrode in generating current, the slope of each of these lines was analyzed using the Randles-Sevcik equation (Eq. 24),[172]

$$i_p = 0.4463 \left(\frac{F^3}{RT}\right)^{1/2} n^{3/2} A D_O^{1/2} C_O^* \upsilon^{1/2} \qquad \text{(Eq. 24)}$$

where i_p is the peak current (Amps), F is Faraday's constant (96458.34 C/mol), R is the gas constant (8.341 J/mol-K), T is temperature (298.15 K), n is the number of electrodes involved in the electrode reaction, A is the area of the electrode (0.018 cm^2), D_O is the diffusion coefficient of oxygen in water which is similar to PBS (2.42 x 10^{-5} cm^2/s)[183], C_O^* is the bulk concentration of oxygen (mol/cm^3), and υ is the scan rate (V/s). Using this equation and the slope of the lines in Figure 19 allows for the determination of both the O_2^- concentration and the number of electrons that participate in the electrode reaction.

Even though both electrodes detected changes in oxidative and reductive currents similarly, the electrode kinetics demonstrates a fundamental difference in the way O_2^- is detected. If C_O^* is assumed to be 100 μM, where 100 μM HPX was used to generate O_2^-, then the SOD film was calculated to utilize four electrons while the Pt bare electrode only utilized two. This can be understood by the presence of the HPX/XOD generation of superoxide occurring within the diffusion layer of the sensor itself, a reaction that itself requires two electrons. There has been much debate over whether or not any sensor can actually detect O_2^-in a protic solvent instead of one of its by-products due to its fast dismutation rate.[158] Incorporating SOD into the enzymatic film creates a method for detecting O_2^- at low concentrations directly at the electrode surface, where it can be oxidized at a bare Pt electrode (+0.6 V) or through a faster mechanism of dismutation *via* SOD. SOD electrostatically guides O_2^- into the positively charged active site of SOD to achieve dismutation at 10,000 times the speed of dismutation in water.[184]

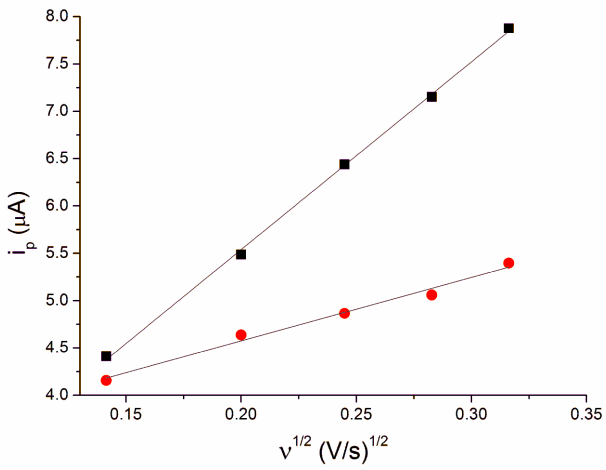

Figure 19. Dependence of the detection of superoxide on the square-root of the scan rate with a SOD film and an acid cleaned SPE (Shown in Figure 18). Measurements were taken in PB with 100 mM KCl, 1 µM XOD, and 100 µM HPX vs. a Ag/AgCl reference electrode. The SOD film (■) and Pt (●) electrodes had linear correlations between scan rate $(V/s)^{1/2}$ and i_{pc} (A) of R^2=0.999 and R^2= 0.987 for the lines, $y = (1.98\text{x}10^{-5})x + (1.57\text{x}10^{-6})$ and $y = (6.70\text{x}10^{-6})x + (3.24\text{x}10^{-6})$, SOD and Pt respectively.

The Randles-Sevcik equation can be used again with the assumption that the concentration of O_2^- could equal up to 400 µM, since one mole of hypoxanthine can create two molar equivalents of O_2^- in its conversion to xanthine and then two more molar equivalents of O_2^- in its conversion to uric acid. Using Equation 24 and HPX concentration of 400 µM, the SOD film was calculated to utilize 1.6 electrons while the bare Pt electrode was calculated to utilize 0.8 electrons. The dismutation of O_2^- *via* SOD occurs in a two electron, two proton coupled reaction, while the oxygen couple is known to occur *via* a one-electron transfer and the oxidation of hydrogen peroxide is also a one-electron transfer.[165, 167, 185] The utilization of 1.6 electrons at the SOD electrode surface could be explained by the combination of increased current flow from both O_2^- detection (2 e^-) and from diffused hydrogen peroxide (1 e^-). While it is expected that some of the current increase is due to hydrogen peroxide detection formed through O_2^- dismutation in

water (Figure 17), the 0.8 electrons calculated for the bare Pt electrode cannot be explained by this theory. Instead, the most likely understanding of the reaction mechanism occurring at our electrode must be a combination of these two theories, dependence of current on both hydrogen peroxide diffusion and HPX/XOD O_2^- production at the sensor surface. The combination of these two theories support a reaction mechanism that would involve 4 and 2 electrons transfers for the detection of O_2^- at the SOD and Pt electrodes respectively. With this new SOD electrode, literature results examining the mechanism of SOD dismutation are confirmed and the enzymatic mechanisms involved in O_2^- dismutation are retained.[186, 187]

The enzymatic activity and the reproducibility of the hand-cast method and the ink-jet printing method of enzyme deposition were determined (Figure 20). The size of the printed droplets was determined using profilometry (Figure 21). Even thought the droplets could not be sized directly on the platinum portion of the SPE due to surface roughness (Figure 21A), it could be sized on the acrylic portion of the SPE (Figure 21B). The droplets had an average width of 42.7 ± 1.0 μm with an average spacing of 4.4 ± 0.6 μm. Each droplet was higher along the edges, 325.6 ± 14.0 nm, and lower in the middle, 243.0 ± 14.3 nm. The correlates to an approximate volume of 0.41 pL or 4% of the 10 pL drop volume. The SOD-BSA-PBS solution is composed of 6% SOD-BSA. The activity of these droplets was then evaluated. First, the slopes of the line denoting change in HPX concentration versus the change in current were compared. The handcast had an average slope of 3.1 ± 0.9 nA/μM HPX and a LOD of 0.10 μM HPX, while the printed films had slope of 3.5 ± 0.4 nA/μM HPX and a LOD of 0.19 μM HPX. This is a 28% deviation among electrodes for the handcast enzyme film, and an 11% deviation for the printed

films (Figure 22). Second, the activity and reproducibility over an 8 day period were assessed. The deviation in the slope among electrodes for the handcast films was 14, 22, and 19% for days 1, 5, and 8 respectively. On these same days, the printed films had deviations of 11, 8 and 6%. No downward trend in slope was seen, outside of the error, to indicate the loss of enzymatic activity was seen for handcast or printed films. The average slope calculated across the 8 days was 3.3 ± 0.7 nA/μM HPX for the handcast film and 3.9 ± 0.5 nA/μM HPX for the printed film. These slopes were determined to not be statistically different. To determine whether or not enzymatic activity was lost in the printing process, the Michaelis-Menten constants for the two electrodes were compared using a Lineweaver-Burk plot.[188, 189] The handcast film was seen to have a K_m of 0.25 ± 0.24 mM with a V_{max} of 0.89 ± 0.78 μA. The printed film was seen to have a K_m of 0.11 ± 0.04 mM with a V_{max} of 0.47 ± 0.14 μA. These enzymatic activities are comparable with those determined polarographically and spectrophotometrically in literature for SOD, K_m of 0.54, 1.3, and 3.5 mM.[190, 191] This demonstrates that SOD can be printed with limited loss of enzymatic activity using the ink-jet printing method. This also shows that the immobilized SOD can achieve dismutation of O_2^- at a rate nearing the nearly perfect dismutation achievable in nature, creating an efficient and quantifiable sensor.

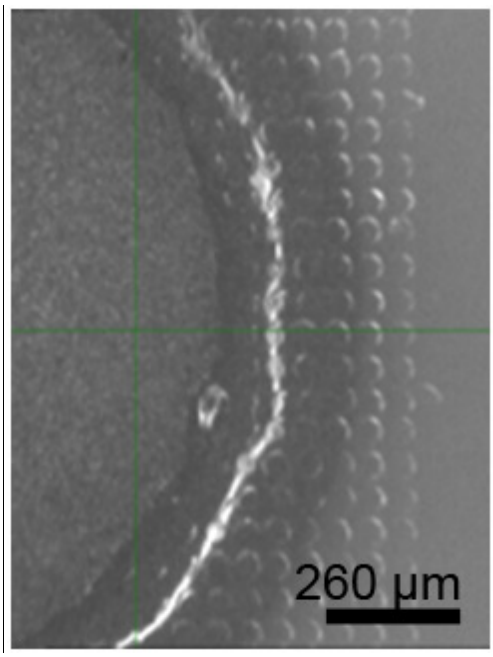

Figure 20. SPE with a SOD printed film taken with a Dimatix Fudicial Camera at 10 x magnification.

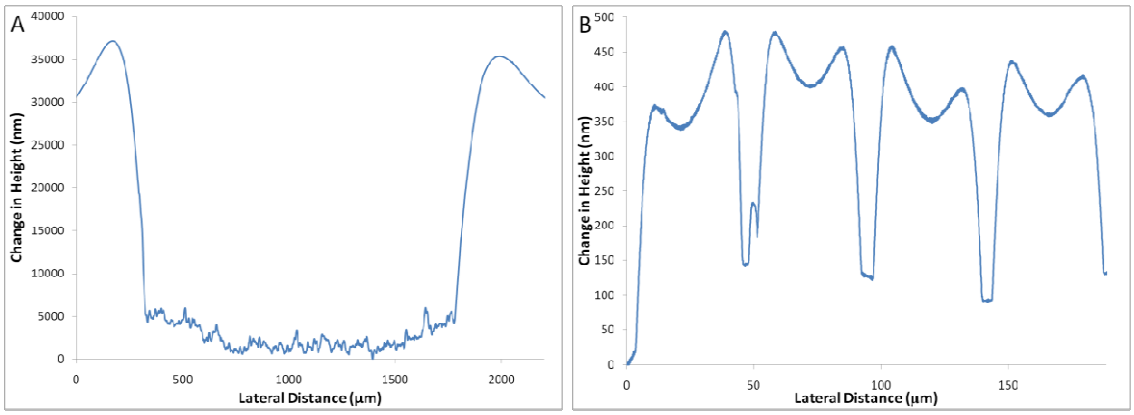

Figure 21. Profilometry of SOD/BSA printed film on the Pt portion of the SPE where the droplets can not be identified due to the high surface roughness (A) and on the acrylic portion of the SPE where 4 individual SOD/BSA droplets are seen (B).

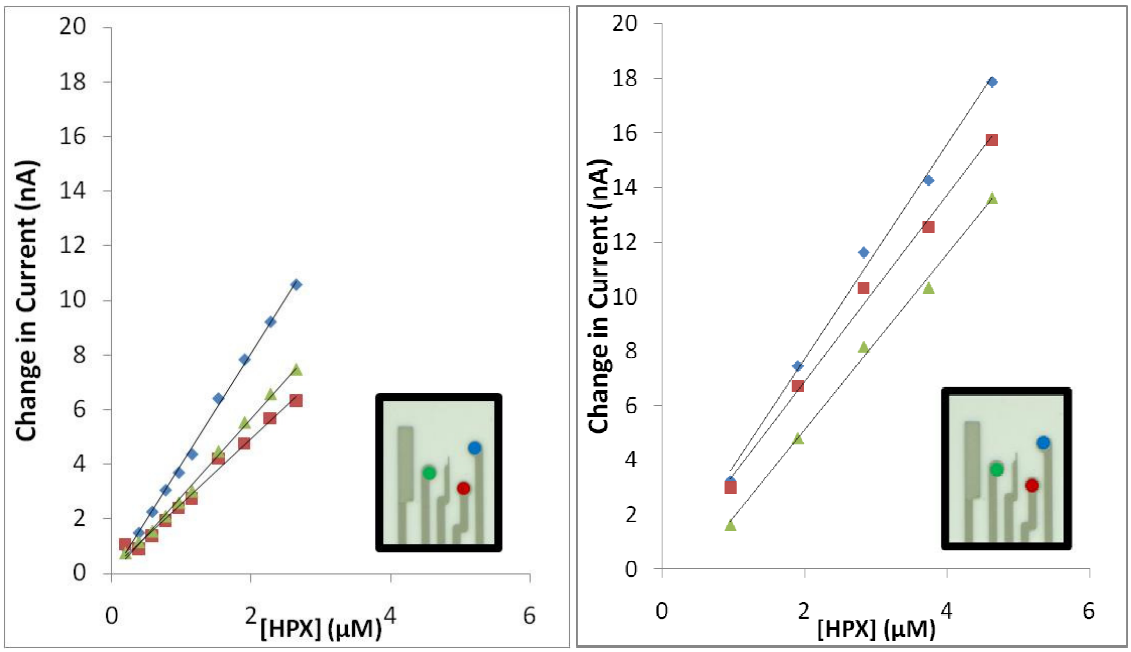

Figure 22. Amperometric calibration of hand-cast and ink-jet printed SOD biosensors. The handcast film (left) demonstrates greater deviation in slope (3.1 ± 0.9 nA/µM HPX, 28% deviation) compared with those electrodes coated with a printed film (right, 3.5 ± 0.4 nA/µM HPX, 11% deviation).

Understanding how SOD functions in aprotic solvents will lead to increased confirmation of the theories of electron transfer introduced previously. Without hydrogen ions in solution, the mechanism of SOD dismutation is drastically changed. With Cu/Zn SOD complexes, a histidine located within the active site gives up its coordination with the metal center coordinates with hydrogen through its amine group, which increases the stability of the dismutation reaction.[186, 187] In this two step process, two successive superoxide radicals enter the active site and are converted to O_2 and H_2O_2.[186] Characterizing the SOD electrode in an aprotic solvent will lead to better understanding of the sensor and answer two main questions, can the dismutation of O_2^- proceed without the presence of hydrogen ions, and how many electrons are involved in this electron transfer. Therefore, the SOD biosensor was studied in both DMSO and *p*-xylene.

DMSO is an aprotic solvent that has been utilized in the study of the oxygen couple.[165, 167] DMF and ACN were also examined, but the greatest reversibility was observed in DMSO, so all further aprotic reactions were carried out in this solvent.[169] The generation of O_2^- was achieved using potassium superoxide (KO_2). It was desirous to see the effects the HPX/XOD couple would have on electron transfer in an aprotic solvent, but due to lack of solubility, they could not be used. UV-Vis was used to detect uric acid production from the generation of O_2^- in DMSO, DMF and ACN. No product peak was seen in any of these solvents and KO_2 was therefore used to generate O_2^-.

Bare Pt and SOD coated electrodes were analyzed using cyclic voltammetry to determine the electrochemical mechanisms of the film. The reversible oxygen couple on a Pt electrode (ΔE_p of 156 mV, i_{pa}/i_{pc} of 0.81) had similar peak separation to the SOD coated electrode at low scan rates (ΔE_p of 141 and 159 mV, i_{pa}/i_{pc} of 0.74 and 97, υ of 50 and 100 mV/s respectively, as determined by taken the first-order derivative of the peaks). The CVs are shown for comparison at a scan rate of 100 mV/s (Figure 23), where a shift in the current baseline is seen and peak broadening occurs indicating lessened reversibility and the presence of an adsorbed species.[172, 192] At higher scan rates, υ of 200, 300, 400 and 500 mV/s, the peak splitting is decreased to an average of 45 mV, but the graph of i_p *vs.* υ demonstrates irreversible behavior (Figure 24). Using Equation 24, the known one-electron transfer on a platinum electrode can be used to determine the number of electrons involved in the electrode reaction on the SOD electrode, 3 e^-. This is once again two more electrons involved in the reaction at the electrode surface. It appears that SOD still functions *via* a 2 e^- mechanism, even in an aprotic solvent.

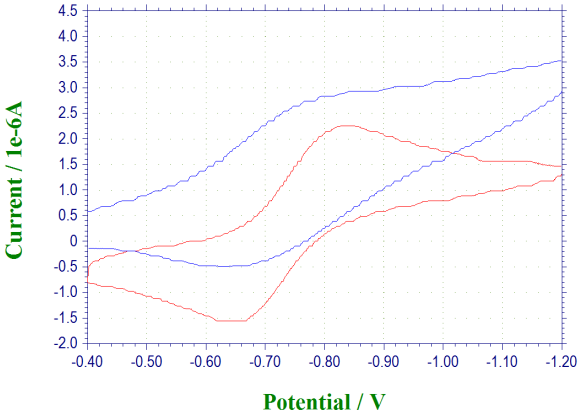

Figure 23. Oxygen couples in DMSO on bare Pt and SOD coated electrodes at a scan rate of 100 mV/s. A vertical shift in current and peak broadening is seen.

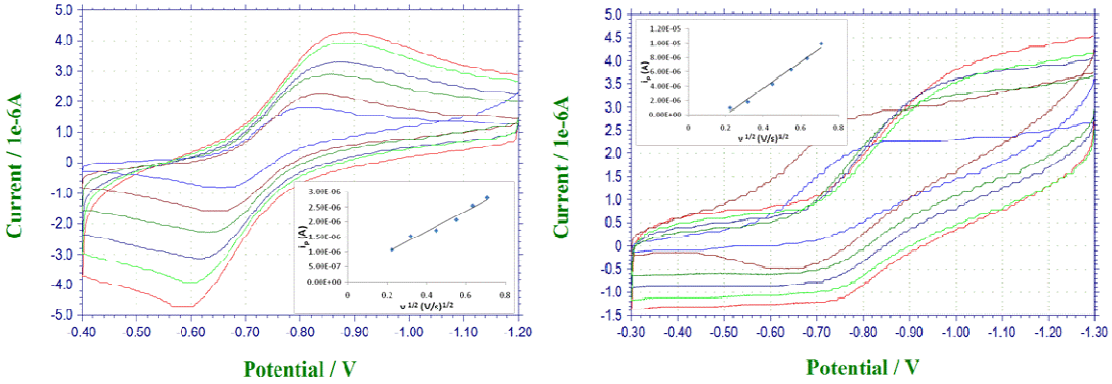

Figure 24. Oxygen couples as a function of scan rate on Pt and SOD coated electrodes in DMSO (0.1 M TBAP, υ = 50, 100, 200, 300, 400, and 500 mV/s). Pt (*left*) demonstrates reversible behavior, while SOD coated (*right*) shows irreversible behavior.

To look further at the behavior of the oxygen couple, KO_2 was added to the bulk solution of DMSO. The Pt electrode detected a shift in formal potential and then an increase in anodic current (Figure 25). The SOD electrode detected increases in cathodic current (Figure 26). The CVs had to be taken immediately after the addition of KO_2 to prevent diffusion and possible loss of superoxide ions. The decrease in current, followed by an increase with additional superoxide ions by the bare Pt electrode was unexpected. The

initial decrease might be caused by dimerization of the superoxide ions in the bulk solution, which is typical in an aprotic solvent.[172] Further increases then would be due to the additional amounts of superoxide ions. The increase in cathodic current is due to increased scavenging by SOD at a potential where SOD cannot be reoxidized, and therefore results in a greater amount of O_2 present near the electrode surface that can be reoxidized during the cathodic scan. Overlaying the derivatives of the CVs (+1 to -1.3 V range) for the increasing concentration of superoxide demonstrates a slight increase in current with concentration around +0.7 V where SOD can be reoxidized. The increase is not higher than the signal to noise ratio. These experiments confirm the reaction mechanism theorized from the experiments performed in PBS and demonstrate a 2 e^- process for SOD, even in an aprotic solvent.

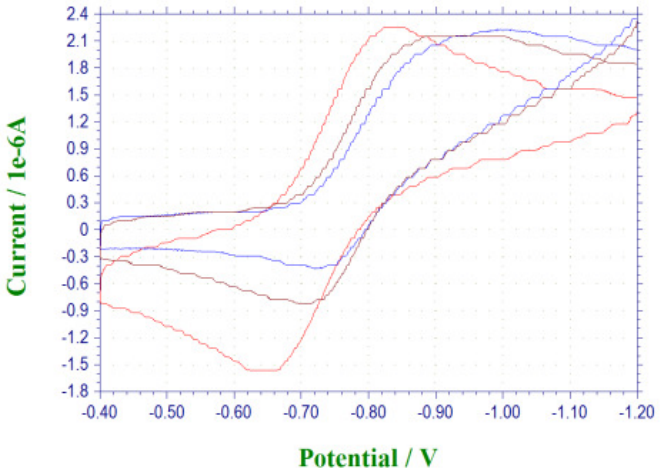

Figure 25. Pt electrode in DMSO with increasing amounts of superoxide. The CV was conducted at a scan rate of 100 mV/s with increasing concentrations of superoxide, 0 (*red*), 2 (*blue*), and 5 (*brown*) µM.

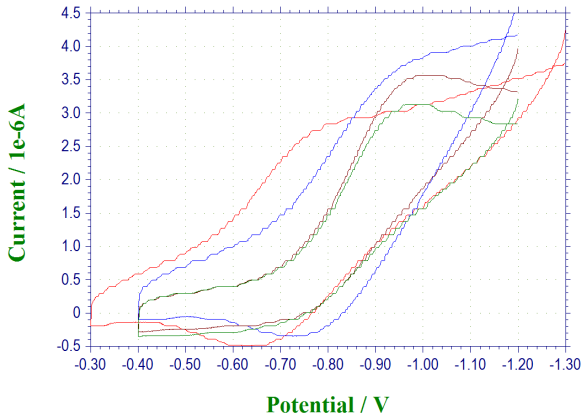

Figure 26. SOD coated electrode in DMSO with additions of superoxide at a scan rate of 100 mV/s. Increasing concentrations of superoxide, 0 (*red*), 5 (*blue*), 10 (*brown*), and 20 μM (*green*), resulted in increases in cathodic current.

Absorbance peaks for the reaction of HPX with XOD can be seen in both PBS and *p*-xylene, which can therefore be used as comparisons for reactions in the presence and absence of hydrogen ions (Figure 27). The absorbance of standard solutions of XOD and HPX, as well as the reaction products XAN and UA (Figure 15), were also determined. The production of UA by the mixture of XOD and HPX in *p*-xylene demonstrated that *p*-xylene can be used with HPX/XOD as an alternative to aprotic reaction conditions.

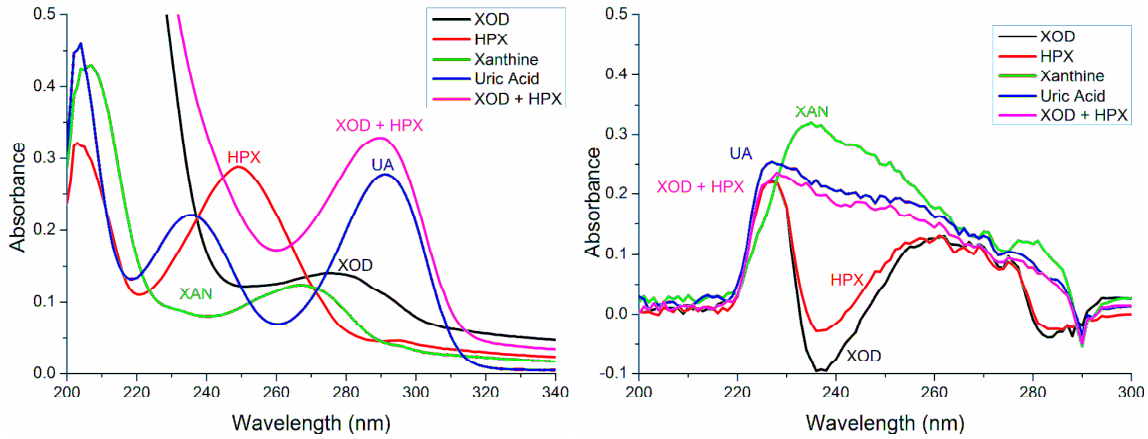

Figure 27. Production of uric acid confirmed with UV-Vis spectroscopy by HPX/XOD. The conversion of HPX to UA by XOD was confirmed spectrophotometrically in PBS (left) and *p*-xylene (right). Standard mixtures of XOD (λ_{PBS} = 275), HPX (λ_{PBS} = 203 and 249), XAN (λ_{PBS} = 207 and 267), and UA (λ_{PBS} = 204, 236 and 291) are shown for comparison. In *p*-xylene, all samples have maximum absorbance around 230 nm, but UA and XAN have broader absorbance that extends to 290 nm.

The majority of electrochemical experiments are not performed in aromatic hydrocarbons with a macro electrode due to the high resistance of these solvents.[177] All experiments were performed in 1 M TBHDPBr to help overcome the high intrinsic resistance, but the limit of solubility of the salt has not been reached and more electrolyte could be added (Figure 28). The oxygen couple was seen at a slightly more negative formal potential than in aprotic solvents (-1.1 V) and was eliminated by 15 minutes of nitrogen purging. The bare Pt and SOD coated electrodes both detected a negative shift in baseline current with increases in superoxide production. The large shift in baseline with both addition of O_2^- and increases in scan rate are most likely due to the depletion of salt at the electrode interface causing an increase in resistance between scans. This was confirmed by a nonlinear correlation between the square root of scan rate and i_p. Further studies in additional aromatic solvents will be required to determine whether or not

HPX/XOD within the diffusion layer of the electrode are the cause of the 4 e^- reaction mechanism seen in PBS.

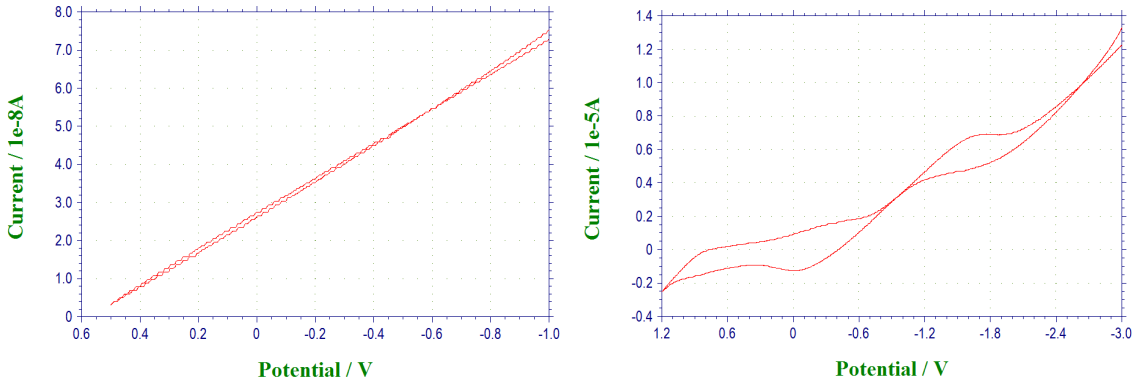

Figure 28. CVs of a Pt electrode in *p*-xylene with varying resistance. The CV on the left demonstrates high solution resistance with a salt concentration of 0.1 M TBHDPBr, while the right CV was performed with 1 M TBHDPBr at a scan rate of 100 mV/s.

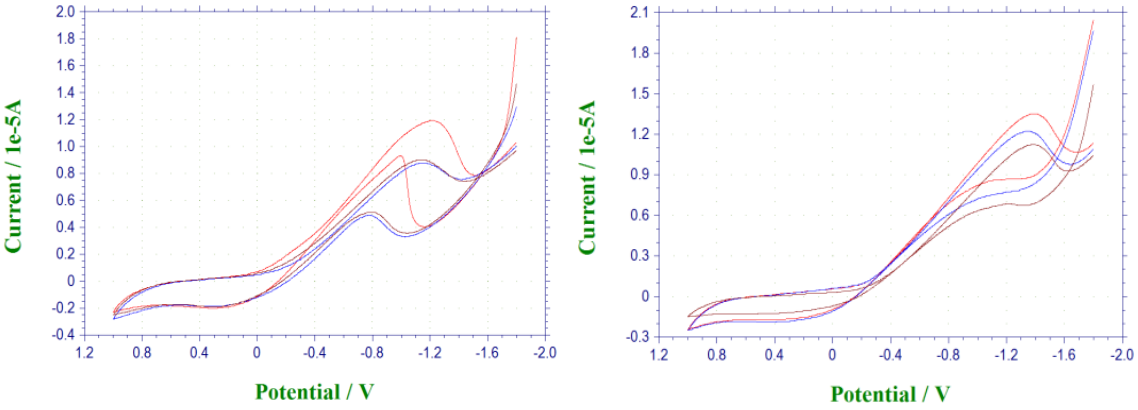

Figure 29. CVs of the oxygen couple in *p*-xylene (1 M TBHDPBr). The electrochemistry of a bare Pt (*left*) and SOD coated (*right*) electrode was studied in XOD (0.1 µM, *red*), HPX (2.5 µM, *blue*) and HPX (5 µM, *brown*) at a scan rate of 50 mV/s.

CONCLUSIONS

A new SOD electrode was developed for the detection of O_2^-. The electrode was calibrated in a bulk solution with an established LOD of 0.10 and 0.19 µM O_2^- (hand-cast

and printed respectively), with enhanced selectivity towards O_2^- than towards H_2O_2. The enzymatic activity of SOD was retained during the materials printing process. The SOD sensor required two more electrons in the electrode reaction than a bare Pt electrode, confirming the 2 e^- reaction mechanism for the dismutation of O_2^- by SOD established in literature. This work further demonstrates that the 2 e^- reaction mechanism can take place in an aprotic solvent in addition to a protic solvent, where other ions probably ion pair with the histidine in the active site to fill the stabilizing role hydrogen usually plays. This electrode was tested in bulk solutions and further incorporation into a microfluidic device will enable detection of macrophage oxidative burst from exposure to tuberculosis or other pathogens.

ACKNOWLEDGMENTS

This work was supported by a grant from the National Institute of Allergy and Infectious Diseases (UO1 AI 061223). This work would not have been possible without collaborations with the Vanderbilt Institute of Integrative Biosystem Research and Education. I would like to thank Jennifer McKenzie, Gong Ping Chen, Fred Hijazi and Dr. Piotr Kaszynski for conversations and suggestions that were greatly appreciated.

CHAPTER V

DEVELOPMENT OF CELL HOUSING FOR REAL-TIME MONITORING OF OXIDATIVE BURST IN A MICROFLUIDIC ENVIRONMENT

A more complete understanding of macrophage immune responses to tuberculosis could be determined through the combination of microfluidic technology with multianalyte detection.[181] For this purpose, a new microfluidic environment must be developed that can provide stability to the cells in an aqueous environment, while encasing a low sample volume for microfluidic measurements of multiple cells in real-time.[156] Microfluidic devices have been used for DNA sequencing, electrophoresis and immunoassays.[18] They have been used for the detection of as few as twenty tuberculosis bacteria per milliliter in a chip-based diagnostic system.[17] Traditional fabrication of microfluidic devices employs photolithography on glass, quartz, or silicon, but a polymer polydimethylsiloxane (PDMS) can be used as a low-cost alternative.[193] PDMS is optically transparent, chemically inert, and can be fabricated rapidly making it ideal for biological applications.[4, 194] PDMS wells have been used to trap cells and electrochemically detect hydrogen peroxide formation following macrophage oxidative burst.[195] Serving as a platform for this large array of analytical assays, these devices can offer micro- to nanoliter volumes, while providing stable and sensitive measurement aquisition.[16] In this work, microfluidic devices are developed that can house macrophages while incorporating electrochemical sensors. Macrophages are white blood cells responsible for the degradation of bacterium and other foreign pathogens. By studying

macrophage response to *Mtb* antigens, a more complete understanding of pathogen-host response can be developed.

Traditional PDMS processing consists of lithography followed by replica molding.[18, 196] In contrast to these techniques, both positive and negative photo-definable PDMS have been developed that utilize exposure to UV light to achieve feature definition. Exposing PDMS with 2, 2-dimethoxy 2-phenylacetophenone (DMAP) as a photoinitiator to UV light allows PDMS to act as a negative photoresist, where the exposed regions are cross-linked and cured.[197] Unfortunately, exposure to oxygen or ambient light can prevent crosslinking which limits the utility of this technique in microfabrication laboratories. Incorporating benzophenone as a photoinitiator, the PDMS becomes a positive photoresist where areas exposed to light can be washed away in toluene. Photoinitiation with benzophenone does not suffer from the side effects of DMAP.[198, 199] This technique has been used previously to create a microfluidic channel with PDMS sidewalls, a PDMS roof, and a glass base.[194] Glass is robust and rigid but hard to machine, while PDMS is good for sealing microfluidic devices. Combining these desirable attributes into one design can create a stronger microfluidic device.[196]

The hydrophobicity of PDMS must be changed in order to improve fluid flow, device bonding, and cell growth, and to prevent binding of small hydrophobic molecules.[3] The incorporation of a glass roof and floor with PDMS used only in the sidewalls will lower the overall hydrophobicity of the device. This improves fluid flow and possibility for cell growth directly on the device. The creation of a microfluidic device with PDMS sidewalls sandwiched between glass has been previously described where a positive photoresist was coupled with reactive ion etching (RIE).[196] The RIE created a rougher

surface which was detrimental for plasma bonding. In order to achieve bonding, the devices were sonicated in acetone for 10 minutes, and debris was removed with tape followed by the use of high temperatures and a hydraulic thermal press.[196] The use of high temperatures and a hydraulic press are not feasible for incorporation of cell studies, therefore this study centers on chemical modifications to PDMS. Different techniques for achieving hydrophillicity of PDMS have been utilized including 2-hydroxyethyl methacrylate chemical modifications, plasma treatment, and UV/Ozone treatment.[193, 194, 196] These methods work by converting the –O—$Si(CH_3)_2$— methyl groups to hydrophilic moieties such as –OH silanol bonds.[196] These techniques have all resulted in successful bonding and sealing of the microfluidic devices. Other studies have incorporated laminin or other cell adhesion molecules to promote direct cell growth on the PDMS.[99, 200-202] Cell growth was achieved on both plasma treated PDMS and a separate membrane to be inserted between the PDMS channel and platinum electrodes.

EXPERIMENTAL

Materials

Superoxide dismutase (SOD, Bovine), xanthine oxidase (XOD, Bovine), *p*-xylene (HPLC grade), benzophenone, and bovine serum albumin (BSA) were purchased from Sigma Aldrich. Hypoxanthine disodium salt (HPX) was purchased from MP Biomedicals. Glutaraldehyde (GA, 25% in water) was purchased from Acros Organics. Mylar film (3.6 μm thick), glass slides, luer lock syringes, toluene, dimethyl sulfoxide (DMSO) and all other solvents were purchased from Fisher Scientific Company. Phorbol

12-Myristate 13-Acetate (PMA) was purchased from L C Laboratories. Stainless steel blunt needle with luer adapter was purchased from Small Parts Inc.

Instruments and Equipment Utilized

Amperometric experiments were attained using a Vanderbilt Institute for Integrative Biosystems Research (VIIBRE) multichannel multipotentiostat at a potential of +0.6 V *vs.* a Ag/AgCl (2M KCl) reference electrode.[180] Voltammetric measurements (LSV, CV, or OCP experiments) were collected on a CHI 660a potentiostat from CH Instruments with a picoamp booster and faraday cage. Profilometry measurements were made using a Veeco Dektak Profilometer. UV exposure was attained with EXFO Novacure® 2100 by Photonic Solutions Inc. Plasma treatment was achieved with a Harrick Plasma cleaner. A Laurell Technologies Corporation spin coater was used for spin deposition.

Cell Culture

The adherent mouse macrophage cell line, RAW 264.7 (ATCC), was maintained in continuous culture with Dulbecco's Modified Eagle's Medium (Mediatech, Inc), supplemented with 10% fetal bovine serum (Atlanta Biologicals, Inc), 1% sodium pyruvate (Mediatech, Inc), and 0.1% Gentamicin Sulfate (BioWhittaker) at pH 7.40 in a 5% CO_2, 37 °C atmosphere. Dulbecco's Phosphate Buffered Saline (DPBS) without calcium and magnesium salts from Atlanta Biologicals Inc. was used between passages.

Cell growth prior to incorporation into Microfluidic Devices

Cell growth on PDMS was achieved through laminin or collagen cellular adhesion layers as well as through plasma treatment. Collagen was adhered to the PDMS at 7.5 $\mu g/cm^2$ (50 µg/mL in 0.1 M HCl) for one hour at room temperature. Laminin was adhered to plasma treated PDMS at 10 $\mu g/cm^2$ (10 µg/mL in media) for one hour at room temperature. After each treatment, the PDMS surface was washed and exposed to approximately $5x10^4$ cells prior to incubation under normal culture conditions. Cell growth and confluency was affirmed 12 hours later through visual microscopic inspection. Plasma treatment was achieved through 30 seconds of exposure.

Polycarbonate membranes (3 µm pore size) from Fisher Scientific Company were plasma treated for 30 seconds. The membranes were placed into individual culture dishes with flexiPERM reusable cell culture chambers by Sarstedt, Inc. (growth area of 0.9 cm^2, dimensions of 11x8x9 mm^2). Raw 264.7 cells were deposited onto the membrane and the remaining chamber volume was filled with culture media. The remainder of the culture dish was also filled with culture media to allow for the exchange of nutrients across the membrane, while preventing cell loss to the culture dish outside of the culture chamber. Prior to experimental usage, the growth area was excised and placed into the microfluidic chamber immediately before plasma bonding. Images were taken with a Pixera Camera attached to an Olympus Microscope (Figure 30).

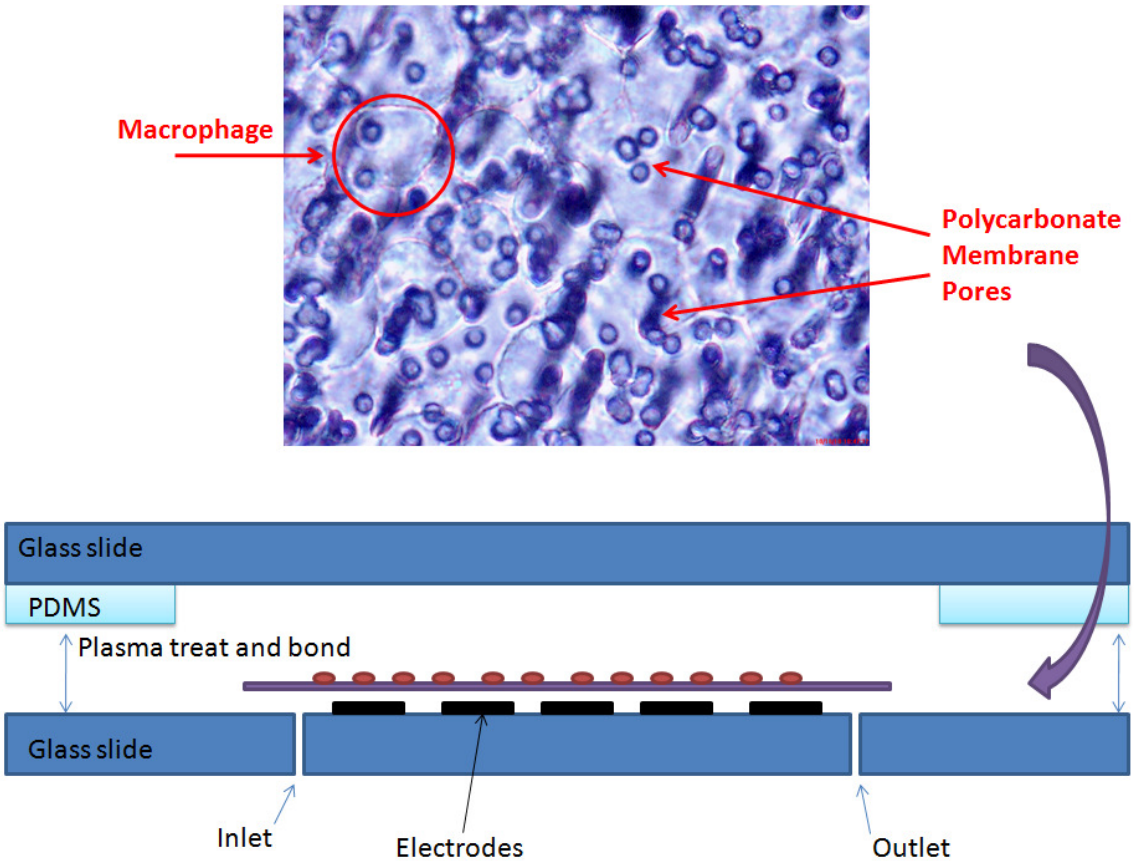

Figure 30. Diagram demonstrating macrophage growth on a polycarbonate membrane and incorporation into a photocurable microfluidic device. The macrophages shown are at 50 x magnification.

Development of PDMS Microfluidic Devices

Photolithography and patterning of SU8 wafers was performed by David Schaffer in collaboration with J. R. McKenzie and VIIBRE. Custom designed (J. R. McKenzie) screen-printed platinum electrodes (SPE) were attained from Pine Research Instrumentation. Dow Corning Sylgarda 184 silicone elastomer kit (PDMS) was purchased from Essex Brownell. The PDMS was poured over the negative SU8 wafer and hardened for a minimum of 2 hours at 55 ºC (10:1 PDMS to curing agent). The PDMS was separated from the mold and silanized by exposure to

trichloro(1H,1H,2H,2H-perfluorooctyl)silane (Sigma Aldrich Co.) under vacuum within a glove box (N_2 atmosphere) for a minimum of 3 hours. The molds were soaked in water overnight and then sprayed with IPA and dried. PDMS was again poured over this mold, cured, and silanized as previously mentioned. This set of PDMS molds was cured and used as the negative from which all future PDMS microfluidic devices were attained.

The height of the PDMS devices was determined using profilometry. A new device was poured for every experiment. Inlet/outlet holes were punched with a 1.8 mm diameter hole punch. Tygon tubing had an outer diameter (OD) of 1.78 mm and an inner diameter (ID) of 1.02 mm. The PDMS device was plasma treated, with a mask covering the binary splitting, prior to cell plating to allow a confluent layer of cells to adhere to the PDMS before every experiment. The cells were plated at a density of $3x10^5$ cells. The PDMS device with adhered cells was pressed against the SPE and held in place with a home-built clamping device. The electrodes consist of a rectangular counter electrode (19 mm^2), 3 circular working electrodes (1.8 mm^2), and a smaller working electrode (0.08 mm^2). The electrode is connected to a downstream 2 M Ag/AgCl reference electrode (Molecular Devices, Inc).

Enzyme coating

BSA was dissolved in phosphate buffer at a concentration of 62 mg/mL. Next, SOD was dissolved in the PB-BSA solution at a concentration of 5000 U/mL PB-BSA. Glutaraldehyde was then added to the solution at a concentration of 1 µL GA/250 µL PB-BSA. Finally, the solution was hand-cast using a pipette tip onto each of the larger screen

printed working electrodes (1.8 mm^2) and was allowed to dry. The electrodes were stored in PBS at 20 ^{0}C.

Testing Cellular Responses with PDMS Microfluidic Devices

Electrochemical cellular responses were attained using a home-built multipotentiostat, amperometric i-t, at a potential of +0.6 V.[180] Flow of the media was controlled by a Harvard Apparatus Pump 11 PicoPlus MA1 70-2213 syringe pump at a rate of 20 µL/min. LabVIEW software was designed to control pump flow as will be discussed in Appendix A. The media was warmed prior to microfluidic device entry using a Watlow temperature controller with silicone rubber heaters.

Crystal Clear Alternatives to PDMS Microfluidic Devices

The use of Crystal Clear 200 rigid urethane (Smooth-On, Inc.) was explored as a rigid alternative to PDMS. Universal Mold Release (Smooth-On, Inc.) was sprayed into the PDMS molds developed previously. Crystal Clear was poured into the molds and cured overnight at room temperature. Adhesion to the SPE was attempted using vacuum grease, a PDMS gasket, a PDMS stamp and stick seal,[203] and a thin layer of PDMS that was spin-coated onto the device (1000 rpm, 60s).

Photocurable PDMS Microfluidic Devices

Inlet and outlet holes were drilled into a 2"x3" glass slide using a Cameron Micro drill press with variable speed control and a metal bond diamond core drill bit (0.039 inch OD mounted on a 3/8"-24 female adapter) from Technodiamant USA, Inc. The glass slides

were cleaned with piranha and isopropyl alcohol (IPA) and then dried with N_2 (g). Photocurable PDMS (PC PDMS) was mixed as previously described[198, 199] with a few modifications for a thicker PDMS layer. Briefly, 1.5 g benzophenone/mL *p*-xylene was sonicated until benzophenone was completely dissolved.[197, 204] The PMDS was mixed 10:1 PDMS:curing agent with 4.5% benzophenone. The inlet and outlet holes were covered on the backside with tape and then the glass slides were spin-coated with the PC PDMS mixture. The spin times and spin speed were varied to determine the appropriate conditions for the various heights.

The edges of the glass slides were wiped with IPA and placed under a mask for UV exposure. The glass slide (1.0 mm thick) was positioned between two thick glass slides (1.2 mm thick) which were bonded to a third glass slide with 0.4 mm of epoxy. The mask was laid over the PC PDMS, connected to the adjacent glass slides, with a height differential of approximately 0.5 mm. The PC PDMS was exposed to UV light (320-500 nm) with a 5 mm light guide attached to a collimating adapter. The set dose at the light guide was 1080 J/cm^2 and the intensity was set to 6000 mW. The expanded light circle had a 5 cm diameter. The glass slide was placed in the oven (120 °C) for bake times proportional to the thickness of PC PDMS, normally 2-4 minutes. The slide was rinsed with toluene and IPA and then dried with N_2 (g). Prior to plasma bonding, the slides were sonicated in acetone for 15 minutes to remove impurities and create a stronger seal.[205] Scotch tape was also used to remove impurities immediately prior to plasma bonding.[196]

Microfluidic fittings were purchased from IDEX Health and Science LLC and include tubing (PEEK tubing with ID of 0.01 inch and ODs of 1/16 and 1/32 inch, or with ID of 255 µm and OD of 510 µm), quick connect female luer to 10-32 coned, 1/16 inch OD to

10-32 fittings as either quick connects or nuts with ferrules, tubing adapter sleeves (Teflon, 1/16 inch OD with either 0.033 inch ID or 0.021 inch ID), and nanoports consisting of 6-32 coned nanoports with gasket, and 6-32 to 1/32 inch quick connect fittings. The nanoports were bonded to the glass slides prior to plasma treatment using super glue (Loctite), thus allowing them to be re-used through removal with acetone. The PEEK tubing connected the syringe pumps to a Valco Instruments Co, Inc. 10 position switching valve, to the device, to the downstream reference, and finally to an outlet.

RESULTS AND DISCUSSION

The development of microfluidic devices reduces larger assays into clinically useful fluid amounts for biological study. This work compares multiple methods for incorporating and housing cells for microfluidic studies. PDMS devices 128 ±4 μM in height were replicated and clamped to a SPE *via* a home-made clamping mechanism. The detection of O_2^- was calibrated using solutions of XOD (0.18 μM) with HPX (5-30 μM).[149, 174, 175] Continuous monitoring of O_2^- production was achieved using both continuous flow and stop-flow experiments. Previous work has incorporated the use of stop-flow, where pumping is temporarily halted to allow for the increase or decrease in a given extracellular metabolite over time, and any changes in peak height reflect the consequences of cellular respiration.[181, 185, 206] This allows the metabolites to be maximally produced or consumed, therefore increasing the signal to noise ratio.

The calibration of the SOD sensor was conducted in both continuous and stop-flow conditions (Figure 31). The change in current is an absolute value where continuous measurements were calculated by subtracting the final change in current from the initial

current where HPX concentration was zero. With an increase in HPX concentration, O_2^- production increases and would therefore result in greater oxidation of SOD at the electrode. This resulted in a greater change in oxidative (negative) current. For the stop-flow measurements, the baseline current was subtracted from the peak current. If superoxide was to build up at the electrode, an increase in oxidative current would be expected. Instead, we measured a decrease in oxidative current during each stop flow. This demonstrates the dependence of the oxidative current on the high rate of O_2^- dismutation *via* water and SOD.[151, 152] Without the constant renewal of O_2^- *via* fluid flow, current becomes limited. The differences between convection and diffusion limited current are clearly seen, where the linear response during continuous flow was $y = (0.43 \pm 0.01)\ x + (3.14 \pm 0.23)$ while the linear response during stop-flow had a much lower slope, $y = (0.24 \pm 0.04)\ x + (0.66 \pm 0.67)$. Through examination of these calibration curves, it was determined that a larger sensor response could be achieved with continuous flow measurements.

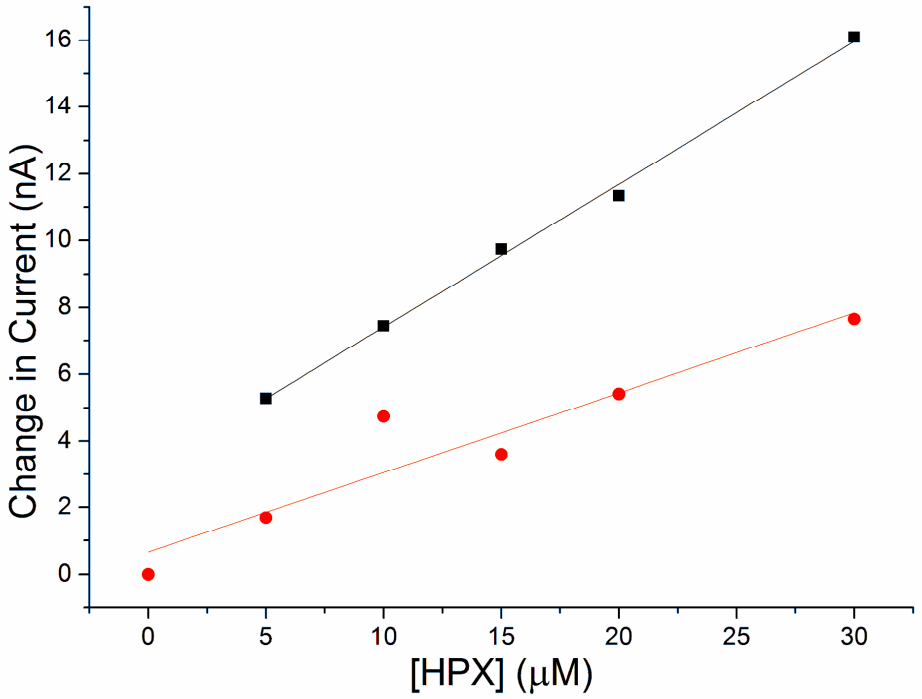

Figure 31. Change in current within a microfluidic device during calibration of SOD coated Pt electrodes using solutions of 0.18 μM XOD with varying concentrations of HPX (5-30 μM). Measurements were taken during periods of continuous flow (■) and stop-flow (●). A zero point was ascertained for stop flow only, as change in current during continuous flow was calculated from the baseline current during 0 μM HPX.

Cellular response to PMA, a known promoter of oxidative burst, was studied in a microfluidic device.[207, 208] Cell adhesion to PDMS was achieved through the use of plasma treatment, laminin and collagen. The cells reached confluency and were clamped to a SPE. After one hour of fluid flow, the PDMS was removed from the clamp and visually inspected. Both laminin and plasma treated PDMS had less than 30% cell loss from stripping during either clamping or fluid flow, while collagen had only about 10% of the cells remaining on the PDMS after testing. Plasma treatment was used for the remainder of experiments for cell adhesion to prevent introduction of an experimental variable with the laminin.

Two microfluidic devices were prepared and exposed to PMA simultaneously (Figure 32). Both microfluidic devices housed one SOD coated electrode. One device contained no cells, while the other was plasma treated and incubated overnight with $5x10^5$ cells. The response to PMA was similar to the response seen using HPX/XOD as a calibration. The cells were examined using stop-flow fluid pumping as can be seen in the raw data (Figure 32A, 210-s of flow/90-s of stop-flow). A close up of the raw data shows that the three main parts of the curve that appear are due to the pumping mechanism (Figure 32B). They consist of (1) baseline current (2) peak current and (3) dip from pump switching. The dip at (3) was originally sharper, returning to position (2) within seconds, but filtering (0.005 Hz) introduced this artificial curve. Filtering was required in order to determine a good average baseline current. Since (3) is a filtering artifact, this means changes in current must be deduced using (1) or a combination of (1) and (2). Stop-flow measurements are taken by subtracting the baseline current from the peak height (Figure 32C). The average baseline current was determined to be 6.5 ± 0.8 nA. The average change in current upon exposure to PMA was 9.5 ± 1.2 nA, which was slightly higher than the limit of detection (9.0 nA). Determining change in flow by plotting the current versus baseline current at (1) over time, demonstrates typical $t^{-1/2}$ decay as explained by the Cottrell equation, which indicates the building of a capacitance double-layer (Figure 32D). This curve has the equation y=(-148.7 ± 5.15) $x^{1/2}$ +(7.28 ± 0.80). The change in baseline current upon exposure to PMA was once again only slightly higher than the LOD, but a change in oxidative response was apparent.

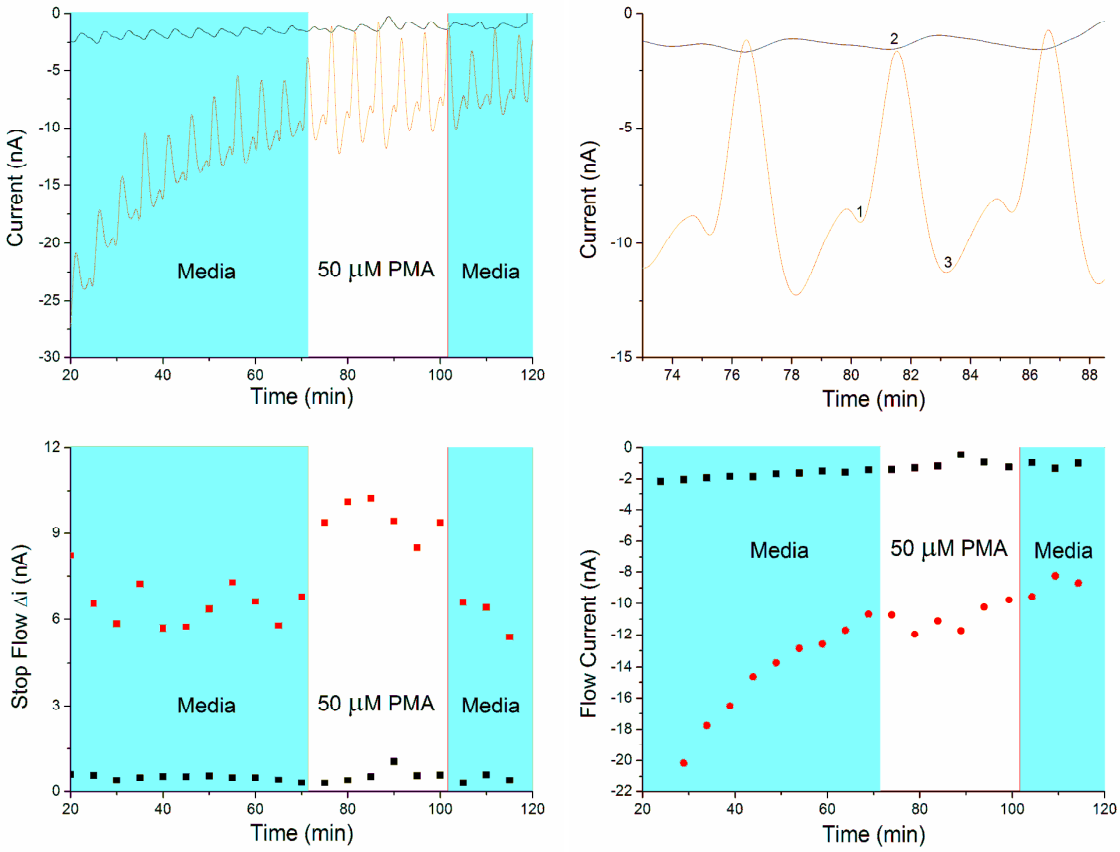

Figure 32. Macrophage response to PMA exposure in a PDMS microfluidic device. The amperometric response of the macrophage can be represented by: (A) raw data filtered at 0.005 Hz (B) close-up of raw data showing the three main parts of every curve, (1) baseline current (2) peak current and (3) dip from pump switching (C) stop-flow analysis where the baseline current is subtracted from the peak current or (D) baseline current. Two chambers were run concurrently where one chamber had no cells (*black*) and the other had $5x10^5$ cells (*red*).

Detection using a typical microfluidic device clamped onto a SPE has been achieved to provide a cellular macrophage oxidative response from the average of multiple cellular responses as desired.[156] The success rate using this system was low, 1 out of every 20, with fluid leakages and cell death resulting from too much pressure on the roof of the devices. To overcome these issues, several other rigid microfluidic techniques were explored. Crystal Clear® is a polyurethane alternative to glass that can be poured into

molds and rapidly replicated for experimental use. No bonding of the Crystal Clear® molds to the SPE was achieved directly. Adhesion to the SPE was attempted using vacuum grease, a PDMS gasket, a PDMS stamp and stick seal,[203] and a thin layer of PDMS that was spin-coated onto the device (1000 rpm, 60 s).The use of both vacuum grease and the stamp and seal methods resulted in incomplete seals and therefore constant leakage. The PDMS gasket allowed fluid flow, but resulted in the loss of all internal features. The Crystal Clear® with PDMS spincoated onto the hardened mold resulted significant losses in internal features (from 128 ±4 μM as a solid urethane, to 35 ± 4 μm when coated with PDMS). A tight seal was not formed with the SPE and resulted in leakage. This could be caused by irregularities in the PDMS layer due to spreading prior to curing as well as the normal non-uniformity of spincoating around the edge of the substrate. In order to further advance this method and ensure uniform pressure around the seals, plasma bonding could be utilized with newly fabricated platinum electrodes on a glass slide. Spinning a thin layer of PDMS onto a glass slide that has platinum electrodes, curing, and then plasma bonding to the Crystal Clear® device slide could result in uniform chamber sealing. The additional layer of PDMS on the electrode side would help account for heterogeneous spincoating along the edges.

The PC PDMS was shown to be a robust and quick method for creating a microfluidic device. In contrast to the Crystal Clear® which has PDMS on three walls, a more hydrophilic channel has been created using PC PDMS to create a rigid microfluidic environment. PC PDMS was spun onto glass slides and the height for each speed and spin time were determined (Figure 33.) The logarithmic trend lines for each spin time are: y= -(170.6 ± 40.7)ln (x) + (1246.6 ± 268.2), y= -(129.3 ± 0.5)ln (x) + (933.6 ± 2.8), y= -

$(112.3 \pm 7.9)\ln(x) + (772.1 \pm 48.0)$, and $y = -(72.7 \pm 13.2)\ln(x) + (504.4 \pm 79.6)$ for 30, 60, 120, and 180 seconds respectively. To give a height of 118 µm, slides were piranha cleaned and then coated with PC PDMS by spinning at 550 rpm for 60 s. A 3x2 inch glass slide must be used as the 1x3 inch glass slides do not have enough space for a uniform layer of PC PDMS in the center of the slide. The smaller glass slides have edges that are higher than the device features and interfere with plasma bonding. After a layer of PC PDMS was formed on the slide, the slide was held under a mask (500 µm difference between the mask and PC PDMS layer, Figure 34) and the dose at the substrate was 10.8 J/cm^2.The PC PDMS was cured for 3 minutes and 15 seconds at 120 ºC.[198] At this temperature and time, all regions that were exposed to UV remained un-cured due to production of radicals that prevented crosslinking, while all other regions became cured. The unexposed regions were then washed with toluene and IPA and dried with N_2 (g). A razor blade was used to remove all PDMS further than 1 cm from the outer edges of the microfluidic features. The slides covered in cured PC PDMS were then sonicated in acetone for 15 minutes to remove impurities. The samples were rinsed with IPA and dried with N_2 (g). Scotch tape was also used immediately before plasma treatment and bonding to remove any impurities gained during transport.

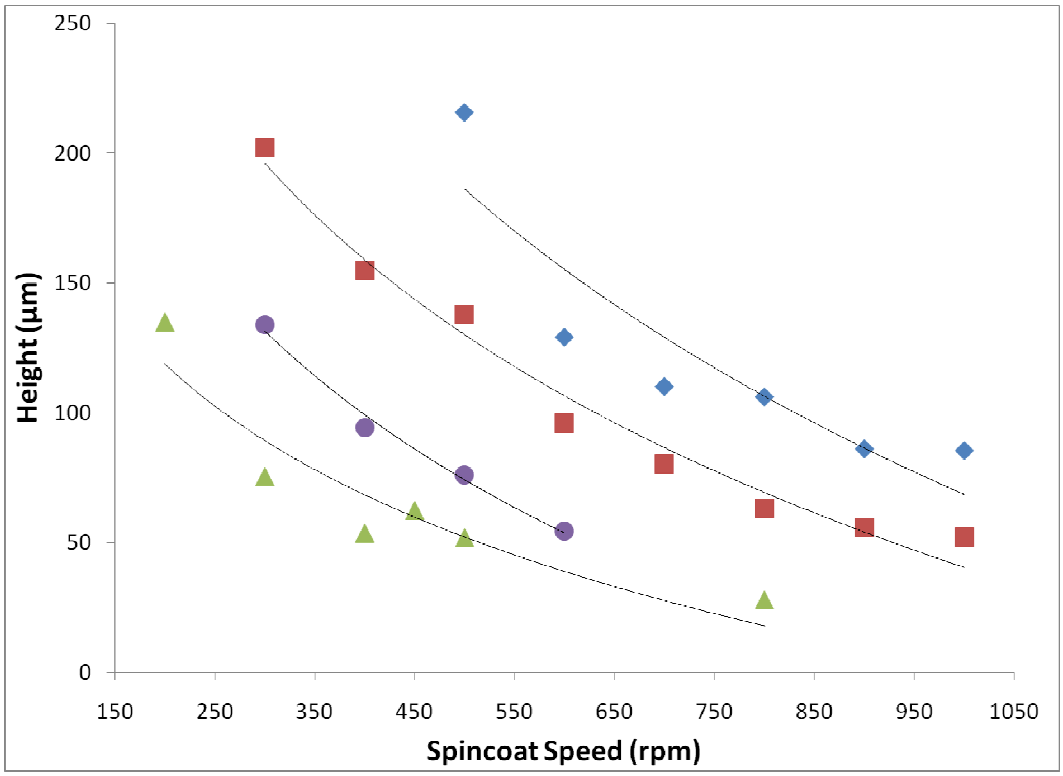

Figure 33. PDMS heights achieved at a variety of spincoat speeds. Increasing the spin time resulted in a decrease of PDMS height. The times represented here are: 30 s (◆), 60 s (■), 120 s (●) and 180 s (▲).

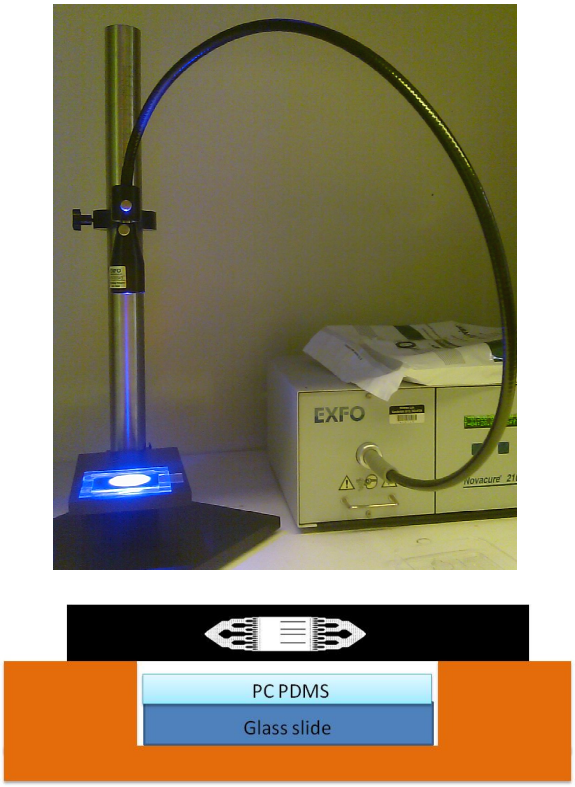

Figure 34. PC PDMS photoinitiation achieved using UV light. The top figure shows the collimating adapter used to direct light to the substrate. The bottom figure shows the typical setup for laying the mask over the PC PDMS by attaching it on both sides to two thick (1.5 mm) glass slides. The glass slide the PC PDMS was on was only 1.0 mm. The thick glass slides were bound *via* epoxy to allow for easy transfer of the PC PDMS into the appropriate position for UV exposure.

Once the microfluidic devices were created, they were assembled and fluid flow was tested overnight. Initially, the PC PDMS was clamped onto a SPE. As can be seen (Figure 34A), clamping methods resulted in leaks, but plasma treating the SPE resulted in no chemical modifications and therefore no way to form a permanent bond. Alternatively, plasma bonding the PC PDMS to a glass slide resulted in a strong seal that would last overnight or longer (Figure 34B). Some of the devices were rinsed with water, set aside, and tested a week later with successful fluid flow. Using the PC PDMS with Pt electrodes

evaporated onto a glass slide will allow these new devices to be used in a variety of electrochemical detection strategies.

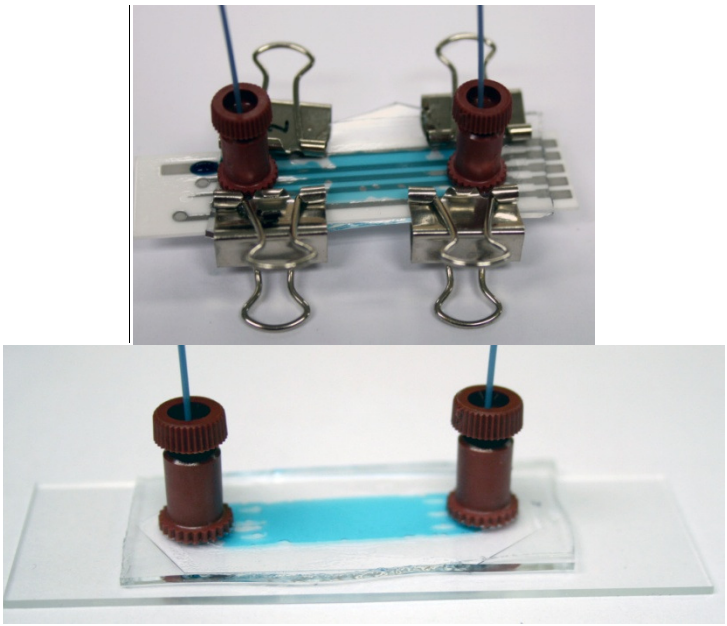

Figure 35. PC PDMS microfluidic devices demonstrating fluid flow. On the top, PC PDMS was clamped onto a SPE where non-uniform flow and leakage was seen. On the bottom, PC PDMS was bonded to a glass slide, both of which were plasma treated, and fluid flow is illustrated with blue food coloring.

CONCLUSIONS

Detection of macrophage oxidative burst using a SPE in a microfluidic environment provided a summative cellular macrophage oxidative response as desired. HPX/XOD was used to demonstrate the requisite constant renewal of O_2^- *via* fluid flow, without which current becomes limited. The differences between migration and diffusion limited currents are clearly seen, and a larger current response was achieved with continuous flow measurements. Exposure to PMA generated an oxidative response, which was detected in a microfluidic device. The cellular response to PMA was similar to the response seen using HPX/XOD as a calibration. The usability of PC PDMS was shown to

be a robust and quick method for creating a microfluidic device with hydrophilic channels. This new method combined with new electrode designs will pave the way for improved electrochemical studies of oxidative responses.

ACKNOWLEDGMENTS

This work was supported by a grant from the National Institute of Allergy and Infectious Diseases (UO1 AI 061223). This work would not have been possible without collaborations with and use of instruments associated with the Vanderbilt Institute of Integrative Biosystems Research and Education. Collaborations with Jennifer McKenzie and Ron Reiserer were essential.

APPENDIX A

LABVIEW PROGRAM DESIGN FOR CONTROL OF MULTIPLE SRS QCMS AND FOR INCORPORATION OF SYRINGE PUMP CONTROL INTO MICROFLUIDIC AMPEROMETRIC DATA COLLECTION

SRS QCM MULTIPLEXING

Stanford Research Systems provides a standalone executable file to facilitate data acquisition using the SRS QCM200 Quartz Crystal Microbalance. The software sends a query to all available COM ports and establishes communication with the first QCM to respond with the appropriate identification query. As such, the software only has the capability to run one instrument at a time, even if multiple QCMs are interfaced with the computer. The control of multiple QCMs simultaneously is essential in improving reproducibility and productivity. To achieve this goal, a new LabVIEW program was written with the capability of communicating with 3 QCMs simultaneously.

Tests were performed to determine the reliability of the data collection achieved with each program. The standalone SRS program was tested for 10 minutes with gate times, the amount of time the QCM200 used to acquire a frequency measurement, set to 1 and 0.3 seconds. The average and standard deviation of this sampling was determined using Microsoft Excel (Table 3). Next, the LabVIEW program provided by SRS was also tested in a similar manner using only one QCM. When used to collect data from one QCM, this program performed as effectively as the standalone version.

Table 3.Testing of SRS QCM software against homebuilt LabVIEW software. Three programs were tested for ten minutes to determine the deviation that occurs in the data collection timing. Either 1 channel or 3 channels, refers to the number of QCM's, were tested simultaneously at a sample rate of 1 or 0.3 times per second.

	# of Channels	Set Sample Rate	Average Rate	Stdev	% Deviation
Standalone SRS	1	1	1.07	0.005	0.43%
	1	0.3	0.27	0.054	20.31%
Labview SRS	1	1	1.07	0.005	0.44%
	3	1	1.03	0.142	13.88%
Leslie SRS	3	1	1.00	0.000	0.00%
	3	0.3	0.30	0.007	2.20%

The way the standalone software was written by the SRS programmers made it more difficult to make the modifications that would enable multiple QCM control. In their software, each QCM is controlled *via* a RS232 cable connecting the instrument to a COM port. Using RS232 to USB adapters, all three QCMs were interfaced with the computer. The first QCM turned on is assigned the first available COM port, the second the next available, and the third is assigned to a final COM port. In this way, three separate versions of their LabVIEW VI could be opened simultaneously. The first program would find the instrument connected through the first COM port, and so forth. Then all three VIs could be run almost simultaneously by pressing start on each program sequentially. With much practice, this could result in a delay time in data collection of as little as 19 seconds between the first and last QCM in operation. This peculiarity in the way a QCM is "called" was hidden within many subVIs (subroutines). Thus, it would take extensive programming to make the changes that would allow one program to do the work of 3.

This extensive network of calling multiple subVIs also had detrimental effects on the sampling rate. With only one program running, a large deviation in timing was not seen. Querying 3 COM ports increased the deviation in the sampling rate and should therefore

be avoided. There are two reasons for this large increase in deviation. The SRS LabVIEW program is not designed as simply as it could be, and therefore it wastes vital processing power. There are too many steps required in determining the frequency and resistance of the crystal and not enough time for one sampling to be completed before the next sampling is started. This problem is also seen with the SRS standalone file at lower higher sampling rates (Table 3). Another contribution to the high deviations in sampling rate is the way that the run time of the experiment is calculated. The program calls a LabVIEW VI "relative time," which is set to the computer clock which is also a source of error.

Since there was no simple way to "fix" the issues that caused timing problems within the SRS LabVIEW files, I started from scratch and wrote a new program for controlling up to three QCMs simultaneously using LabVIEW version 8.0. The final block diagram (Figure 36) calls only 5 subVIs, which is in direct contrast to the 100s of subVIs buried within the SRS LabVIEW program. These LabVIEW routines are called Read COM1, Read COM3, Read COM4, Read Frequency String, and Read Resistance String and utilize some of the basic building blocks LabVIEW provides. Read COM1, 3, and 4 all identify the specific QCM being queried, which does not change after turning on the instruments (Figure 37). Read Frequency and Read Resistance Strings send either "F" or "R" commands to the instruments and record the data sent back (Figure 38). In addition to eliminating useless commands, I utilized a time stamp of the current time at the beginning of the experiment and subtracted this input from the timestamp of the current time to improve the accuracy of the time function over the previously used "relative time" function used by SRS. This "Get Date/Time in Seconds Function" utilizes

universal time instead of the clock maintained by the program. The improvements in sampling rate with this newly designed program versus the SRS standalone program and the SRS LabVIEW program are seen in Table 3. At the higher sampling rate, a deviation of 2.2% versus 20.3% was seen, marking a vast improvement.

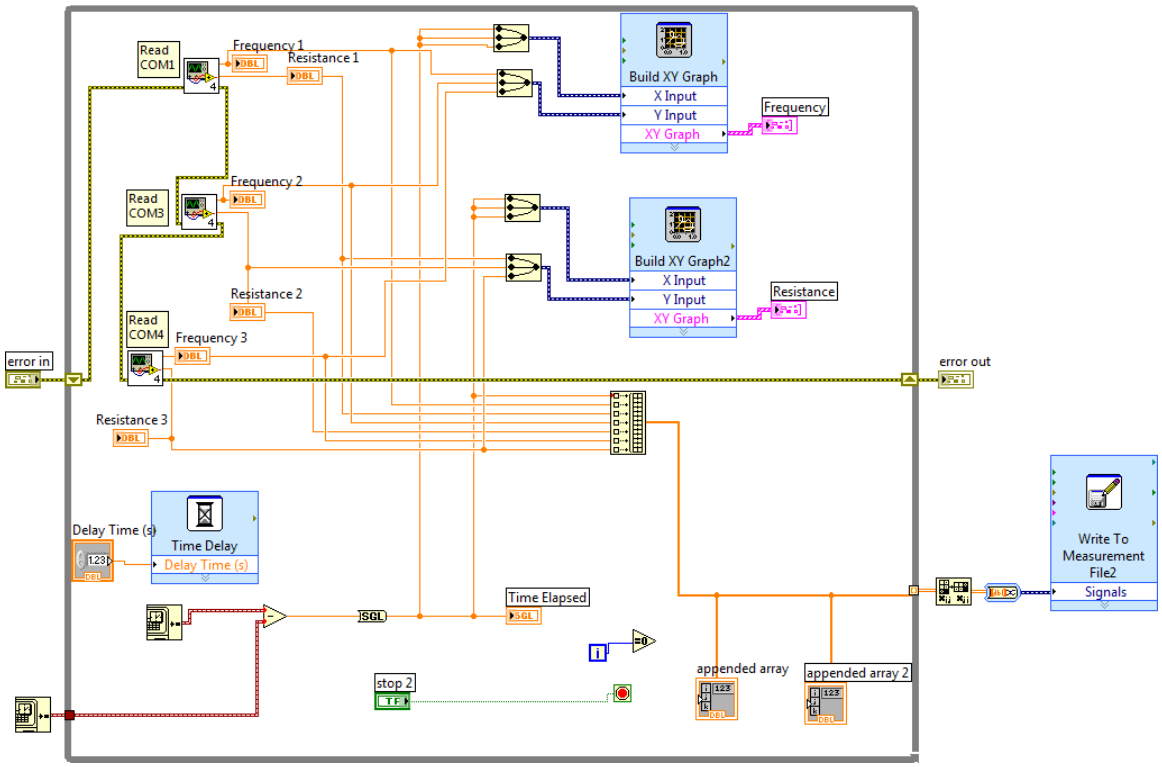

Figure 36. LabVIEW block diagram for control of three SRS QCM200s simultaneously.

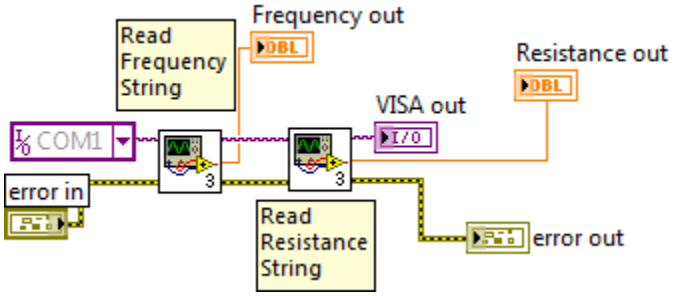

Figure 37. An example COM subVI which is responsible for identifying the correct QCM and call further subVIs to receive frequency and resistance outputs.

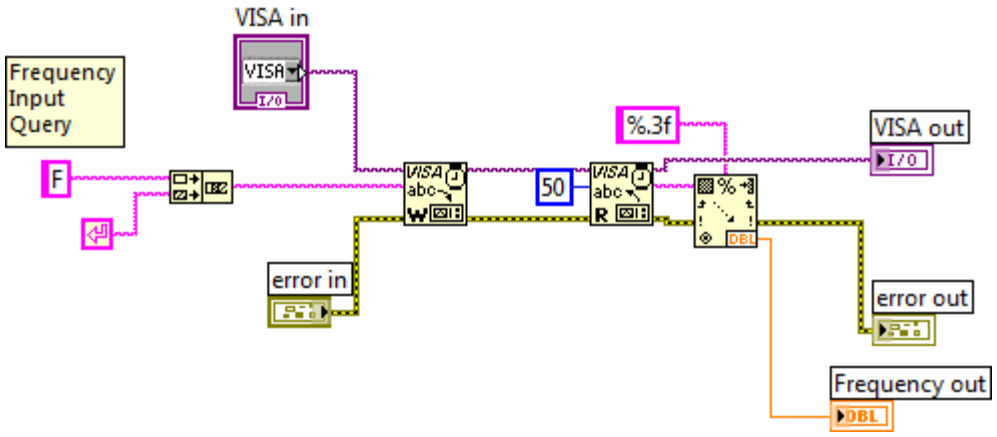

Figure 38. LabVIEW block diagram for attaining frequency measurements. This subVI is termed “Read Frequency String”. Resistance measurements are attained the same way, but use “R” as the input query.

An additional improvement is the automatic data logging function. The original program required a separate step to initiate data logging. Automating this function eliminates the possibility of user error resulting in data loss of the entire experiment. The final program has many advantages over the original program including simultaneous use of 3 SRS QCMs, automatic data logging, one front panel to control all three (Figure 39), and improved timing with lower error.

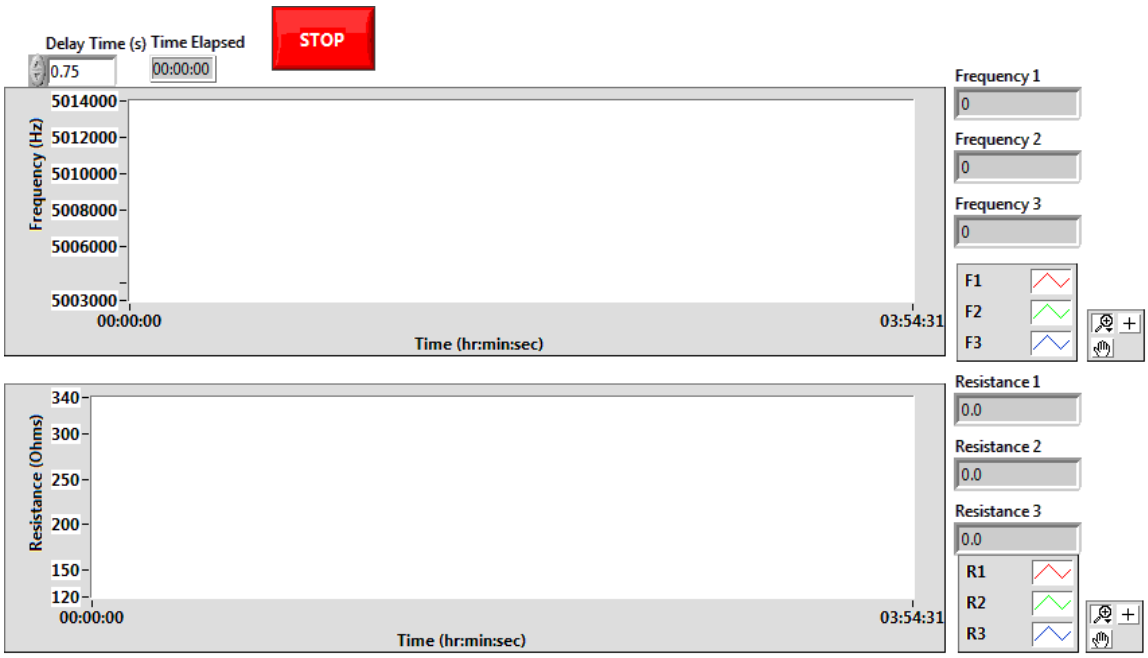

Figure 39. User interface for the LabVIEW program controlling three SRS QCM200s simultaneously. Delay time indicated is used to dictate the sampling rate.

AUTOMATED LABVIEW SYRINGE PUMP CONTROL

In developing the next generation multianalyte microphysiometer (MAMP), screen-printed electrodes (SPEs) were used with a polydimethylsiloxane (PDMS) microfluidic housing. Amperometric measurements were taken using the same LabVIEW program previously developed by Dr. Rachel Snider for the MAMP.[180] However, in order to utilize a stop-flow pumping mechanism for data analysis, control of the Harvard Apparatus Pump 11 PicoPlus MA1 70-2213 syringe pump had to be automated. Harvard Apparatus supplies subVIs for initializing communication with the pump, starting the pump (using presets programmed on the keypad), stopping the pump, restoring keypad control, and for closing communication with the pump. I created a program that utilizes a time delay within a While Loop to provide for the pump on and off times using LabVIEW version 8.5 (Figure 40). The program is controlled by inputs on the front panel

(Figure 41). For the example shown in the figure, the pumps would turn on for 105 seconds, followed by 15 seconds of stop-flow. This input is in seconds and has been tested with inputs from 1 to 15 minute intervals. All interval times resulted in successful flow/stop-flow control with the pump. This VI's block diagram can be inserted into any program that requires flow/stop-flow intervals and was tested in the MAMP LabVIEW program.

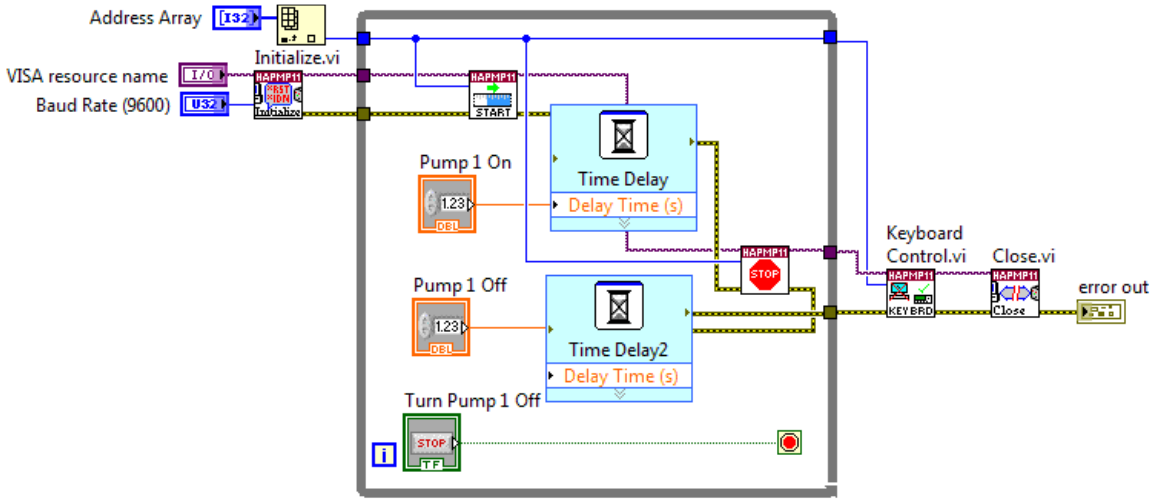

Figure 40. Block diagram for LabVIEW program control of the syringe pumps.

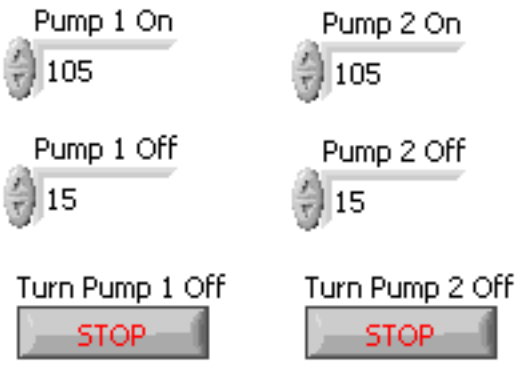

Figure 41. User interface for syringe pump control that was incorporated into the front panel of the MAMP LabVIEW program.

Both of these LabVIEW programs served a very specific function crucial to the completion of this dissertation. The SRS program can be utilized to increase progress of future graduate students. The syringe pump automation program can be used for on-chip sensors to allow for the build-up of metabolites to improve sensitivity.

ACKNOWLEDGMENTS

I would like to thank Dr. Rachel Snider who was instrumental in orienting me to LabVIEW programming and in helping me sort through the piles of subVIs to find the "F" and "R" commands I needed to communicate with the instruments. I would also like to thank Bert McMahan who was a great resource in troubleshooting LabVIEW programs.

APPENDIX B

DITHIOTHREITOL REDUCTION OF ANTIBODIES AS A NEW STRATEGY FOR IMMUNOSENSOR DEVELOPMENT

Antibodies are commonly utilized as recognition elements in immunological sensors. Varying attachment strategies are used to control the orientation of the antibody in the sensor and are key to the successful development of biosensors and protein microarrays, since the random orientation of the immobilized antibody decreases the accessibility of the antibody active site.[209] Biotinylation is often used to couple antibodies to a streptavidin coated quantum dot or other solid support.[210-212] Polyethylene glycol (PEG) and pyridyl disulfide moieties have also been used to link antibodies to solid supports or nanospheres to achieve bio-recognition capabilities.[209, 213, 214] For applications utilizing the quartz crystal microbalance (QCM), Protein G, L, or A are commonly used to bind the Fab region of the antibody.[13, 57, 215-217] In this work, dithiothreitol (DTT) was used to reduce the IgG antibody in an attempt to covalently bond the antibody to the gold without the use of another protein or a conjugation mechanism. DTT has previously been used to covalently bond antibodies to gold, but instead of reducing the internal disulfides, amine- or sulfhydryl reactive crosslinkers were first covalently attached to the antibody and then reduced to provide for the covalent gold bond.[218] Instead of incorporating the reduction of external disulfides, the natural internal disulfides were exploited to provide a strong covalent attachment to gold for future QCM biosensors.

EXPERIMENTAL

Materials and Instrumentation

Goat anti-rabbit (IgG) and rabbit anti-chicken (IgY) antibodies were purchased from Sigma Aldrich Inc. Bovine serum albumin (BSA) was purchased from Aldrich. DTT was purchased from Pierce and stored at 2 °C. Precision Plus protein Kaleidoscope Standards (10-250 kDa) and Bio-Safe Coomassie Stain were purchased from Bio-Rad Laboratories, Inc. Water was purified using a Barnstead NANOpure Diamond water purification system (18 MΩ/cm). Phosphate buffer saline (PBS) was prepared as 50 mM phosphate with 150 mM saline at pH 7.2. All other chemicals were reagent grade and used as received from Fisher Scientific. Millipore Microcon centrifuge filters (30 kDa molecular weight cutoff) were purchased from Fisher Scientific.

Antibody concentration was monitored using UV/Vis spectroscopy. The measurements were taken at 280 nm by scanning at wavelengths from 220-350 nm in a 1.4 mL quartz Spectrocell cuvette (path length of 1 cm) and recorded with a Cary 100 BioSpectrophotometer. A calibration with goat-anti-rabbit antibodies was conducted to determine the extinction coefficients. All gravimetric experiments were conducted using a Maxtek Research QCM.

Reduction of Antibody Fc Region

Antibodies were reduced using DTT. Whole IgG antibodies were diluted to desired concentration. An amount of 1.9 mg of DTT was weighed out and dissolved in 100 µL PBS. Then 24 µL of this solution was added per every 500 µL of diluted antibody. This solution was allowed to react for varying times to determine the appropriate length of

time for reduction of the antibody backbone. The original protocol dictated the removal of DTT by using a Sephadex 10 column; however, this protocol was deemed inefficient and time consuming. Instead, the antibody solution was centrifuge filtered to remove the 25 kDa light chain and DTT from the larger antibody fractions. After centrifugation, the upper portion was saved and reconstituted to 1 mL PBS and absorbance was measured at 280 nm.

Polyacrylamide Gel Electrophoresis

The samples were chromatographed on a 12% Tris-Glycine polyacrylamide gel (Invitrogen) at 37 °C. Voltage was maintained at 135 Volts for 1.5 hrs, with a constant current of 35 mA. The proteins were stained with BioRad Bio-Safe Coomassie stain, then destained overnight with 7.5% MeOH and 5% acetic acid in dH_2O.

Quartz Crystal Microbalance Immunosensor Assembly

All QCM experiments were conducted in a manner similar to those previously mentioned. Briefly, quartz crystals were washed three times with piranha, rinsed with water and ethanol, and dried under a stream of nitrogen before mounting in a Kynar flow cell. The reduced goat anti-rabbit IgG antibodies (10 μg/mL) were bound directly to the gold on the quartz crystals through thiol bonds. Next, BSA (1 mg/mL) was used as a blocking agent to prevent non-specific interactions. PBS was used between steps to wash away any excess samples that had not adsorbed to the crystal face. Last, rabbit antibodies in PBS (20 μg/mL, rabbit anti-chicken) were flowed across the face of the crystal until

binding reached a maximum, as assessed by the leveling off of frequency and resistance curves.

RESULTS AND DISCUSSION

Reduction of Antibody Fc Region

The use of DTT to cleave antibody disulfide bonds can result in three different fragments based upon complete or partial cleavage of all available bonds.[211] These fragments will include light chain fragments (25 kDa), heavy chain fragments (50 kDa) or partially cleaved heavy-light chain fragments (75 kDa) as depicted in Figure 42. For use in immunological recognition, the Fab region must remain intact. The only fragment that has Fab regions intact is the partially cleaved heavy-light chain fragments. The reaction will ideally proceed as depicted in Figure 43.

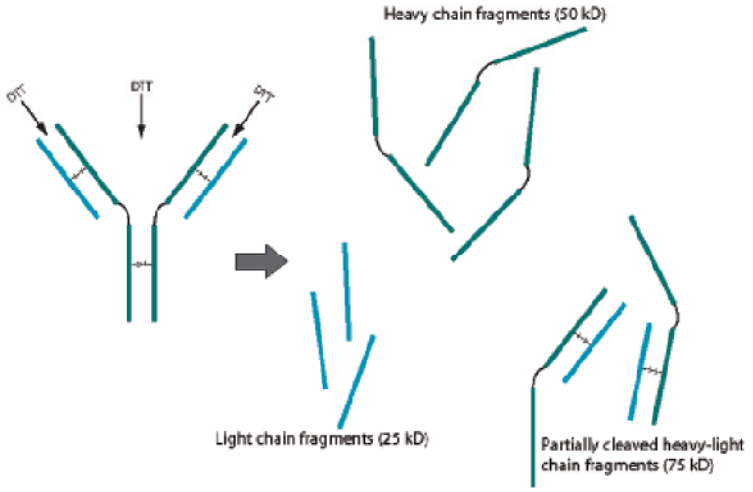

Figure 42. Schematic of DTT cleavage of antibody disulfide bonds.[211]

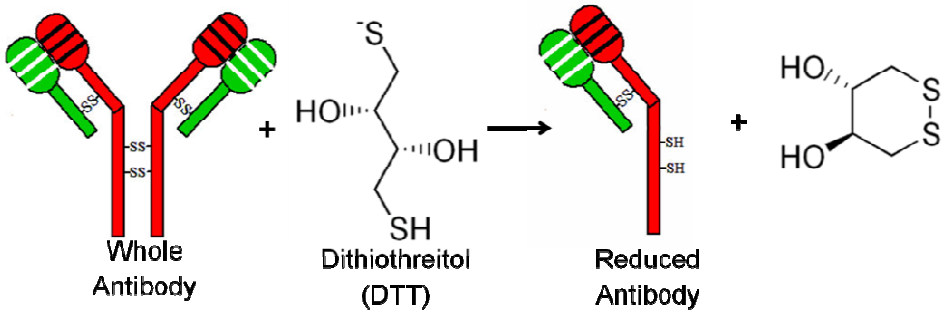

Figure 43. Ideal DTT cleavage of an antibody: the Fab region of the antibody remains intact, with free thiols in the Fc region ready to covalently bind to gold.[219]

In order to verify the reduction of the antibody, polyacrylamide gel electrophoresis (PAGE) was used to verify the presence of any antibody fragments attained. Initial results (Figure 44, left) compared the Kaleidoscope standards to reduced and whole antibodies. The light chain appears at 25 kDa, the heavy chain at 50 kDa, the heavy and light chain held together by a disulfide bond appear at 75 kDa, and the whole antibody appear at 150 kDa. Lane 3 consists of the reduced antibody that was never separated from DTT. Since no band was seen at 75 kDa, this lane consists of complete reduction of the light chain from the heavy chain. Lane 4 is a control which verifies the presence of the whole antibody appearing at 150 kDa.

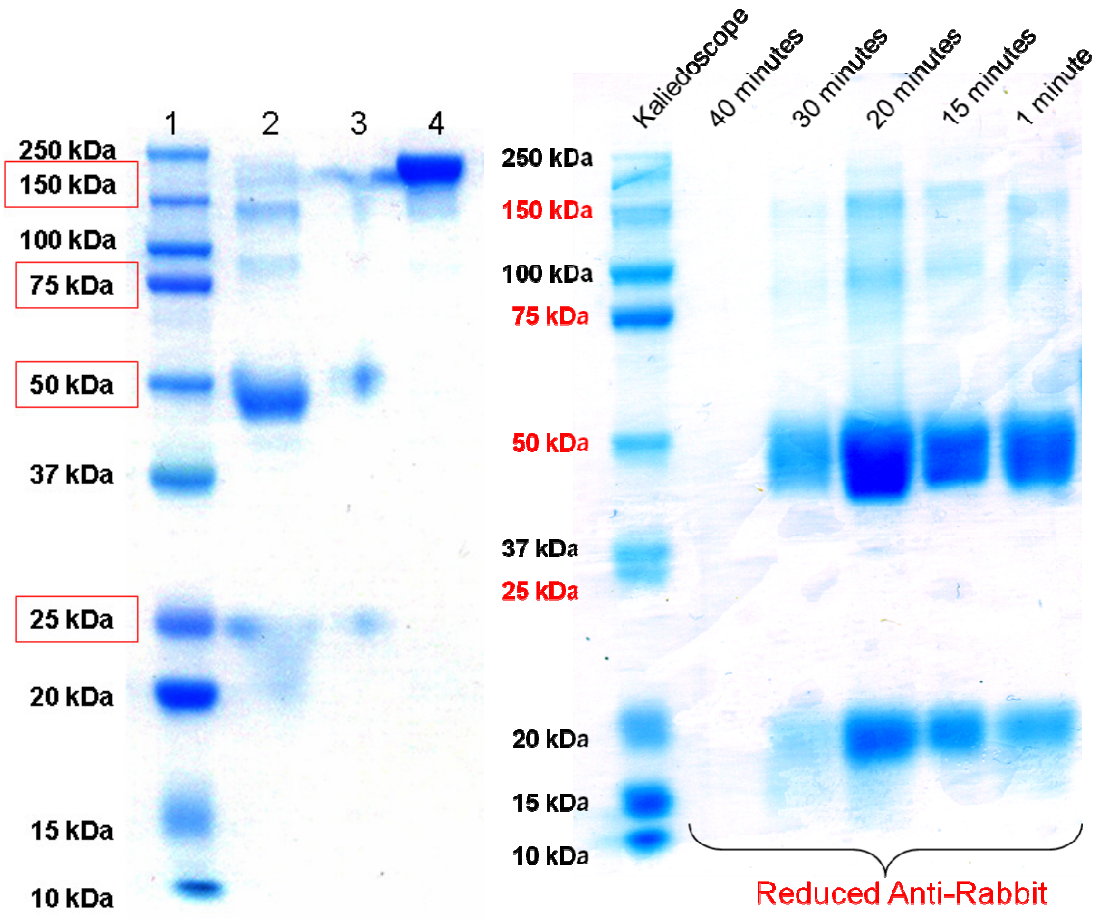

Figure 44. Polyacrylamide gel electrophoresis to determine fragmentation upon exposure to DTT. (*left*) Comparison of reduced to whole antibodies where kaleidoscope marker (*lane 1*), reduced anti-rabbit antibody passed through a Sephadex 10 column (*lane 2*), antibody after 30 minutes of reduction with no separation technique used (*lane 3*), and whole antibodies (*lane 4*) are shown. (*right*) The reduction of anti-rabbit is shown after reduction for 1-40 minutes at the times indicated.

In an attempt to reduce the cleavage of the 75 kDa fragment into 50 and 25 kDa fragments, the DTT exposure time was controlled. The time of DTT exposure varied from 1 to 40 minutes (Figure 44, right). As shown, even the 1 minute exposure time resulted in more 50 kDa bands than 75 kDa bands. Future studies should lower the DTT

concentration in addition to adjusting the times to achieve less fragmentation. Previous studies have shown that the bond between the two heavy chains is cleaved slower than the disulfide bonds between the light and heavy chains, so this study is predicted to have good results.[220]

The absorbance was measured before and after antibody reduction in order to quantify the protein concentration for QCM studies. Initial samples were diluted from a 1 mg/mL stock solution of goat anti-rabbit. A calibration curve was generated using several dilutions to determine a best fit line for antibody concentration in accordance with Beer's Law (Figure 45). The extinction coefficient ($\varepsilon_{percent}$) for these antibodies was determined to be 18.26 ± 0.87 $(g/100\ mL)^{-1}$ cm^{-1}, which is very similar to the previously reported value for goat IgGs of 18.7 $(g/100\ mL)^{-1}$ cm^{-1}.[221] After filtering the 25 kDa fragments from the rest of the protein, a reduction in absorbance was measured (Figure 46). After each sample was reduced and filtered, the concentration would be determined prior to further experimental use.

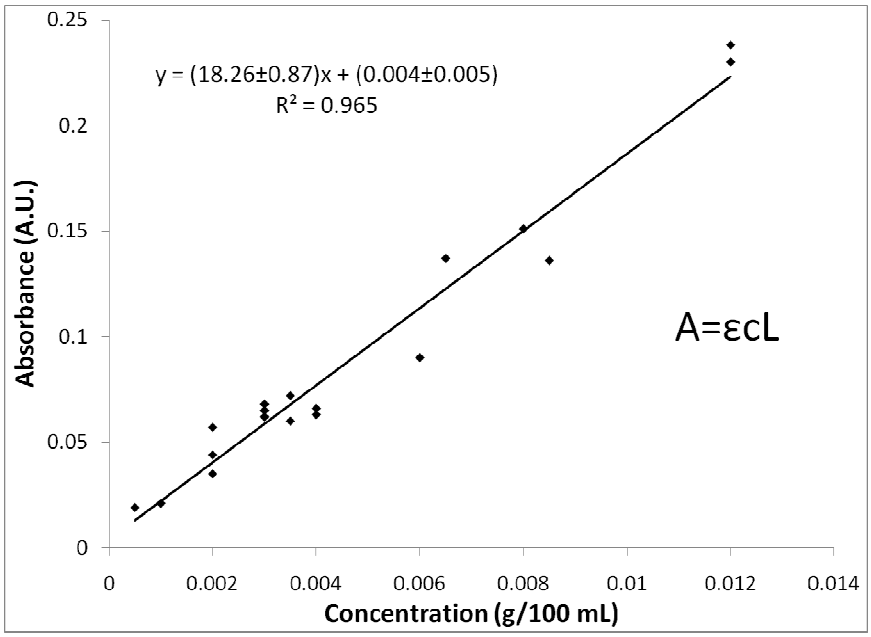

Figure 45. Absorbance of goat anti-rabbit antibodies at varying dilutions. The extinction coefficient ($\varepsilon_{percent}$) for these antibodies was determined to be 18.26 ± 0.87 $(g/100\ mL)^{-1}$ cm^{-1}.

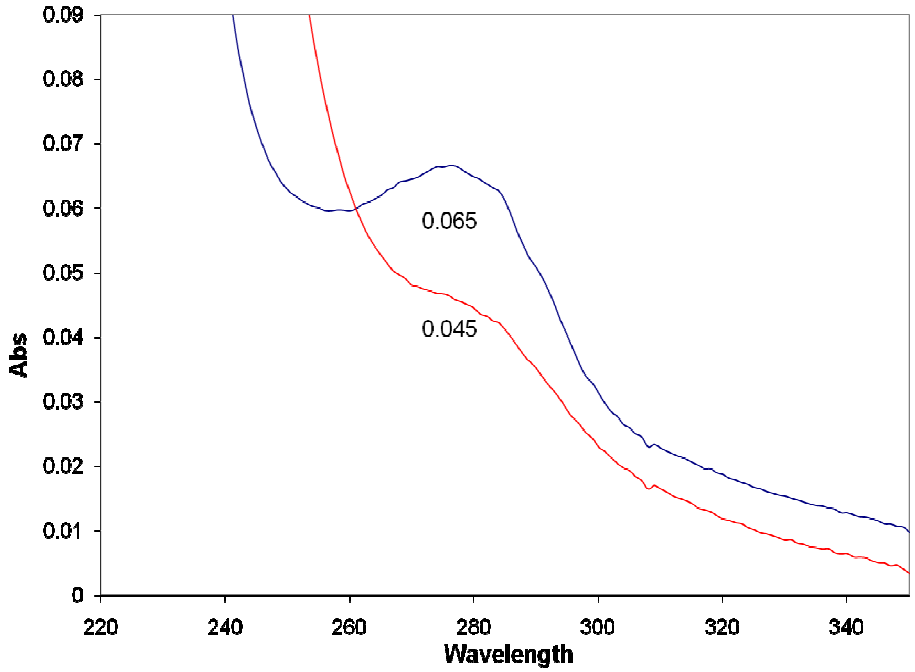

Figure 46. UV-Vis of antibodies before and after DTT Cleavage. The absorbance of whole antibodies (*blue line*) and antibodies reduced with DTT post-filtering (*red line*) is shown.

QCM detection of Rabbit Antibodies using Reduced anti-Rabbit Antibodies

Development of an immunosensor for the detection of rabbit antibodies was created using the reduced disulfide bonds to form a covalent bond with the gold (Figure 47). The antibody uses this chemistry to remain immobilized rather than through a protein linker. The antibodies are filtered after reduction with DTT which leaves the 50 kDa heavy chain along with the desired 75 kDa heavy-light chain fragment.

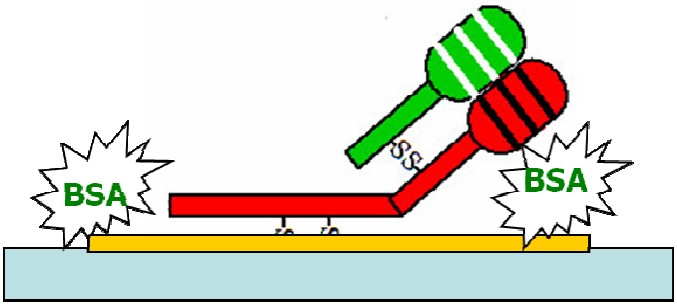

Figure 47. Schematic showing the desired orientation for the reduced antibody on the gold surface of the QCM sensor. The FC region is directed away from the crystal face and is available for immunorecognition. (Not to scale)

The QCM was successfully used to achieve detection of rabbit antibodies with this reduced antibody immunosensor. An example showing typical binding is shown (Figure 48). The antibodies were flowed across the face of the crystal until the surface was saturated. Deposition time was used to optimize anti-rabbit binding. The time of antibody deposition was controlled and ranged from 4-10 minutes. Successful detection was achieved when the anti-rabbit was deposited for at least 6 minutes. The variability of this binding was high, as can be seen in Figure 49. There was a desired linear trend, but with such high standard deviations, no real calibration can be achieved. Even though there was successful biding of the primary antibody to the gold at both 4 and 5 minutes, 58 ± 20 ng and 52 ± 6 ng respectively, there was limited binding of rabbit antibodies in any of the 6

trials. The largest amount of anti-rabbit that bound to the gold occurred when exposed to the crystal surface for 8 minutes, 143 ± 39 ng. This large amount of anti-rabbit on the surface of the crystal also accounted for the greatest detection of rabbit antibodies, 82 ± 56 ng. Specificity of the immunosensor toward rabbit antibodies was confirmed by the lack of rabbit antibody detection when the surface was covered with only BSA, as well as by the lack of detection of mouse immunoglobin with reduced anti-rabbit.

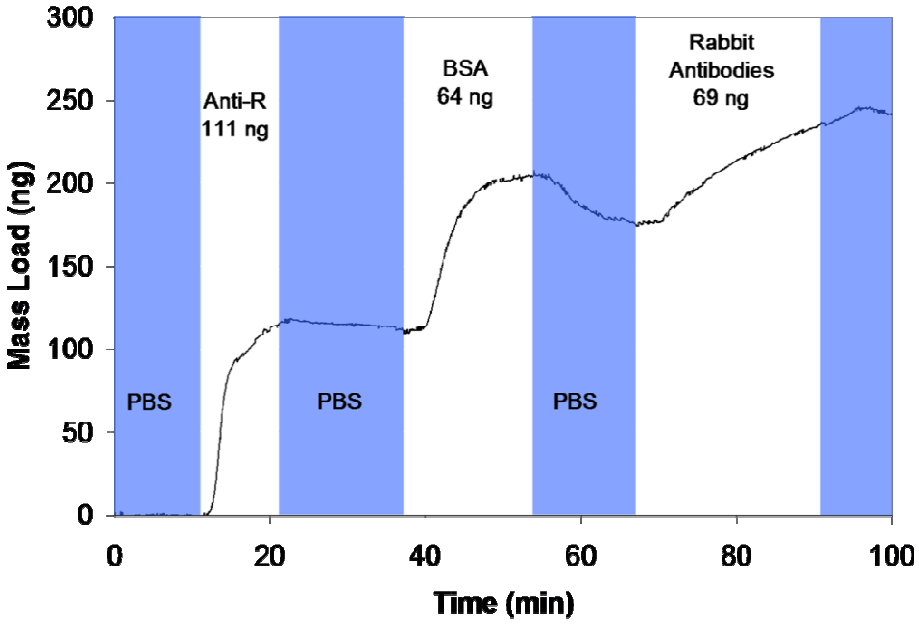

Figure 48. Typical detection of rabbit antibodies using reduced anti-rabbit antibodies.

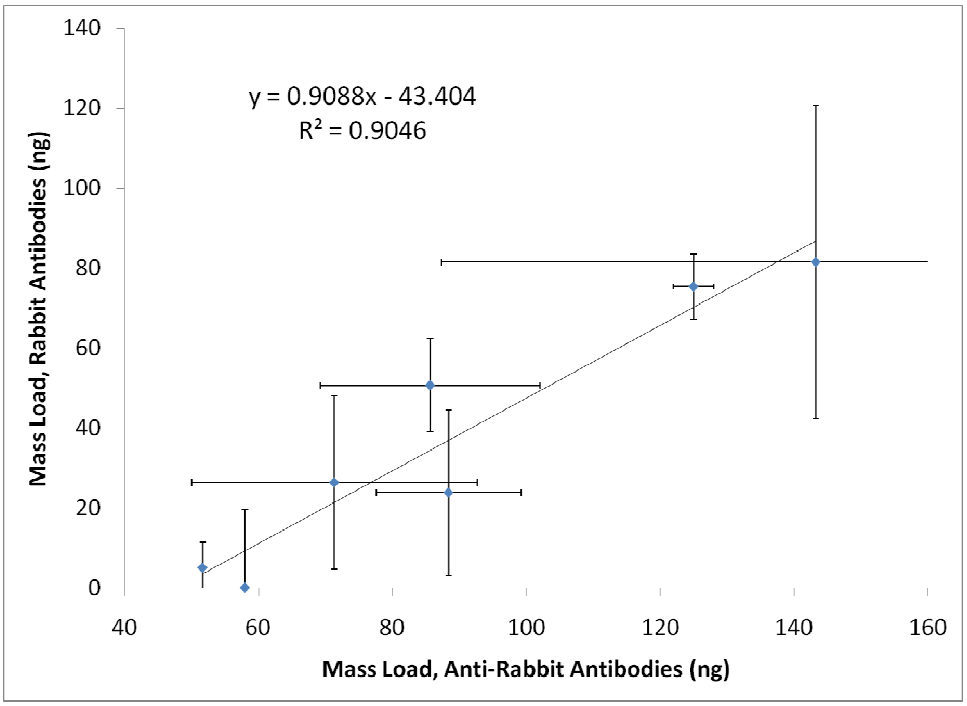

Figure 49. Linear trend showing the average binding with the use of reduced anti-rabbit antibodies. Each data point represents a unit of time, 4-10 minutes that the anti-rabbit was allowed to bind to the sensor surface.

CONCLUSIONS AND FUTURE WORK

Most proteins will bind to gold, albeit weakly through hydrophobic interactions. With this reduction strategy, the chemical attachment of the antibody to the gold was not controlled. Any part of each fragment could have bound to the gold and attachment was not limited to only the sulfide region. The antibodies could have bound strongly through the reduced disulfides, but it was more likely the majority bound non-specifically through any of the protein's hydrophobic pockets. If the orientation of the heavy-light chain fragments could be controlled and the reduced sulfide directed to the surface, then this attachment strategy would result in binding that was stronger than the more common use of Protein A or G antibody attachment. However, the antibody orientation was not controlled, and therefore, any hydrophobic part of the antibody could have interacted

with the gold surface. This promotes weak binding and results in dissociation of the antibody from the gold surface when binding at its Fab region occurs. Additionally, a higher molecular weight filter should have been used to remove the 50 kDa fragment along with the 25 kDa fragment. Lower concentrations of DTT can also be used to increase the concentration of the 75 kDa fragment. If a higher concentration of the 75 kDa fragment is present, then the random orientations that occur could become less significant. While this work has shown the reduction of the antibody backbone can provide for a strong immunosensor, the high variability in sensor calibrations discourages further use.

ACKNOWLEDGMENTS

I would like to thank Dr. Brian Huffman for his help with DTT cleavage and column preparation. Dr. Alex Schrimpe Rutledge was instrumental in running the polyacrylamide gel electrophoresis and I appreciate her help.

REFERENCES

1. Oita, I., Halewyck, H., Thys, B., Rombaut, B., Vander Heyden, Y. and Mangelings, D. (2010) Microfluidics in macro-biomolecules analysis: macro inside in a nano world. *Anal Bioanal Chem*, **398**, 239-264.

2. Yager, P., Edwards, T., Fu, E., Helton, K., Nelson, K., Tam, M. R. and Weigl, B. H. (2006) Microfluidic diagnostic technologies for global public health. *Nature*, **442**, 412-418.

3. Meyvantsson, I., Warrick, J. W., Hayes, S., Skoien, A. and Beebe, D. J. (2008) Automated cell culture in high density tubeless microfluidic device arrays. *Lab Chip*, **8**, 717-724.

4. Chikkaveeraiah, B. V., Liu, H., Mani, V., Papadimitrakopoulos, F. and Rusling, J. F. (2009) A microfluidic electrochemical device for high sensitivity biosensing: Detection of nanomolar hydrogen peroxide. *Electrochem Commun*, **11**, 819-822.

5. Rapp, B., Gruhl, F. and Länge, K. (2010) Biosensors with label-free detection designed for diagnostic applications. *Anal Bioanal Chem*, **398**, 2403-2412.

6. Shen, Z., Huang, M., Xiao, C., Zhang, Y., Zeng, X. and Wang, P. G. (2007) Nonlabeled Quartz Crystal Microbalance Biosensor for Bacterial Detection Using Carbohydrate and Lectin Recognitions. *Anal Chem*, **79**, 2312-2319.

7. Su, X.-L. and Li, Y. (2005) A QCM immunosensor for Salmonella detection with simultaneous measurements of resonant frequency and motional resistance. *Biosens Bioelectron*, **21**, 840-848.

8. Peduru Hewa, T. M., Tannock, G. A., Mainwaring, D. E., Harrison, S. and Fecondo, J. V. (2009) The detection of influenza A and B viruses in clinical specimens using a quartz crystal microbalance. *J Virol Methods*, **162**, 14-21.

9. Sauerbrey, G. (1959) The use of quartz oscillators for weighing thin layers and for microweighing. *Z Physik*, **155**, 206-222.

10. Xia, H., Wang, F., Huang, Q., Huang, J., Chen, M., Wang, J., Yao, C., Chen, Q., Cai, G. and Fu, W. (2008) Detection of Staphylococcus epidermidis by a Quartz Crystal Microbalance Nucleic Acid Biosensor Array Using Au Nanoparticle Signal Amplification. *Sensors*, **8**, 6453-6470.

11. Zuo, B., Li, S., Guo, Z., Zhang, J. and Chen, C. (2004) Piezoelectric immunosensor for SARS-associated coronavirus in sputum. *Anal Chem*, **76**, 3536-3540.

12. Skottrup, P. D., Nicolaisen, M. and Justesen, A. F. (2008) Towards on-site pathogen detection using antibody-based sensors. *Biosens Bioelectron*, **24**, 339-348.

13. Rutledge, R. D., Huffman, B. J., Cliffel, D. E. and Wright, D. W. (2008) Design and synthesis of an antigenic mimic of the Ebola glycoprotein. *J Mater Res*, **23**, 3161-3168.

14. Peduru Hewa, T. M., Tannock, G. A., Mainwaring, D. E., Harrison, S. and Fecondo, J. V. (2009) The detection of influenza A and B viruses in clinical specimens using a quartz crystal microbalance. *J Virol Methods*, **162**, 14-21.

15. Clark, L. C. and Lyons, C. (1962) Electrode Systems for Continuous Monitoring in Cardiovascular Surgery. *Ann N Y Acad Sci*, **102**, 29-45.

16. Ges, I. A. and Baudenbacher, F. (2010) Enzyme electrodes to monitor glucose consumption of single cardiac myocytes in sub-nanoliter volumes. *Biosens Bioelectron*, **25**, 1019-1024.

17. Chun, A. L. (2009) Nanoparticles offer hope for TB detection. *Nat Nanotechnol*, **4**, 698-699.

18. Sia, S. K. and Whitesides, G. M. (2003) Microfluidic devices fabricated in poly(dimethylsiloxane) for biological studies. *Electrophoresis*, **24**, 3563-3576.

19. Ciobanu, M., Taylor, D. E., Jr., Wilburn, J. P. and Cliffel, D. E. (2008) Glucose and Lactate Biosensors for Scanning Electrochemical Microscopy Imaging of Single Live Cells. *Anal Chem*, **80**, 2717-2727.

20. Arrabito, G., Musumeci, C., Aiello, V., Libertino, S., Compagnini, G. and Pignataro, B. (2009) On the Relationship between Jetted Inks and Printed Biopatterns: Molecular-Thin Functional Microarrays of Glucose Oxidase. *Langmuir*, **25**, 6312-6318.

21. Yan, J., Pedrosa, V. A., Simonian, A. L. and Revzin, A. (2010) Immobilizing Enzymes onto Electrode Arrays by Hydrogel Photolithography to Fabricate Multi-Analyte Electrochemical Biosensors. *ACS Appl Mater Interfaces*, **2**, 748-755.

22. (2009) Factsheet on Tuberculosis. *World Health Organization*. http://www.who.int/tb (accessed June 20, 2010).

23. Mabey, D., Peeling, R. W., Ustianowski, A. and Perkins, M. D. (2004) Tropical infectious diseases: Diagnostics for the developing world. *Nat Rev Micro*, **2**, 231-240.

24. Ferguson, N. M., Fraser, C., Donnelly, C. A., Ghani, A. C. and Anderson, R. M. (2004) Public Health Risk from the Avian H5N1 Influenza Epidemic. *Science*, **304**, 968-969.

25. Hauck, T. S., Giri, S., Gao, Y. and Chan, W. C. W. (2010) Nanotechnology diagnostics for infectious diseases prevalent in developing countries. *Adv Drug Delivery Rev*, **62**, 438-448.

26. Wilson, I. A., Niman, H. L., Houghten, R. A., Cherenson, A. R., Connolly, M. L. and Lerner, R. A. (1984) The structure of an antigenic determinant in a protein. *Cell*, **37**, 767-778.

27. Acheson, N. H. *Fundamentals of Molecular Virology*, John Wiley & Sons, Inc.: Hoboken, NJ, 2007, pp. 248-260.

28. Haldar, S., Chakravorty, S., Bhalla, M., De Majumdar, S. and Tyagi, J. S. (2007) Simplified detection of Mycobacterium tuberculosis in sputum using smear microscopy and PCR with molecular beacons. *J Med Microbiol*, **56**, 1356-1362.

29. Chakravorty, S., Dudeja, M., Hanif, M. and Tyagi, J. S. (2005) Utility of universal sample processing methodology. combining smear microscopy, culture, and PCR, for diagnosis of pulmonary tuberculosis. *J Clin Microbiol*, **43**, 2703-2708.

30. Chan, E. D., Reves, R., Belisle, J. T., Brennan, P. J. and Hahn, W. E. (2000) Diagnosis of tuberculosis by a visually detectable immunoassay for lipoarabinomannan. *Am J Respir Crit Care Med*, **161**, 1713-1719.

31. Engin, G., Acunas, B., Acunas, G. and Tunaci, M. (2000) Imaging of Extrapulmonary Tuberculosis. *RadioGraphics*, **20**, 471-488.

32. Maalouf, R., Fournier-Wirth, C., Coste, J., Chebib, H., Saikali, Y., Vittori, O., Errachid, A., Cloarec, J.-P., Martelet, C. and Jaffrezic-Renault, N. (2007) Label-free detection of bacteria by electrochemical impedance spectroscopy: comparison to surface plasmon resonance. *Anal Chem*, **79**, 4879-4886.

33. Perkins, E. A. and Squirrell, D. J. (2000) Development of instrumentation to allow the detection of microorganisms using light scattering in combination with surface plasmon resonance. *Biosens Bioelectron*, **14**, 853-859.

34. Palomino, J. C. (2005) Nonconventional and new methods in the diagnosis of tuberculosis: feasibility and applicability in the field. *Eur Respir J*, **26**, 339-350.

35. Hamasur, B., Bruchfeld, J., Haile, M., Pawlowski, A., Bjorvatn, B., Kallenius, G. and Svenson, S. B. (2001) Rapid diagnosis of tuberculosis by detection of mycobacterial lipoarabinomannan in urine. *J Microbiol Methods*, **45**, 41-52.

36. Sada, E., Aguilar, D., Torres, M. and Herrera, T. (1992) Detection of lipoarabinomannan as a diagnostic test for tuberculosis. *J Clin Microbiol*, **30**, 2415-2418.

37. Yang, L.-M. C., Diaz, J. E., McIntire, T. M., Weiss, G. A. and Penner, R. M. (2008) Covalent Virus Layer for Mass-Based Biosensing. *Anal Chem*, **80**, 933-943.

38. Fung, Y. S. and Wong, Y. Y. (2001) Self-assembled monolayers as the coating in a quartz piezoelectric crystal immunosensor to detect Salmonella in aqueous solution. *Anal Chem*, **73**, 5302-5309.

39. Das, K., Penelle, J., Rotello, V. M. and Nuesslein, K. (2003) Specific Recognition of Bacteria by Surface-Templated Polymer Films. *Langmuir*, **19**, 6226-6229.

40. Mo, X.-T., Zhou, Y.-P., Lei, H. and Deng, L. (2002) Microbalance-DNA probe method for the detection of specific bacteria in water. *Enzyme Microb Technol*, **30**, 583-589.

41. Lee, S.-H., Stubbs, D. D., Cairney, J. and Hunt, W. D. (2005) Rapid detection of bacterial spores using a quartz crystal microbalance (QCM) immunoassay. *IEEE Sens J*, **5**, 737-743.

42. Cooper, M. A. and Singleton, V. T. (2007) A survey of the 2001 to 2005 quartz crystal microbalance biosensor literature: applications of acoustic physics to the analysis of biomolecular interactions. *J Mol Recognit*, **20**, 154-184.

43. Pavey, K. D., Ali, Z., Olliff, C. J. and Paul, F. (1999) Application of the quartz crystal microbalance to the monitoring of Staphylococcus epidermidis antigen-antibody agglutination. *J Pharm Biomed Anal*, **20**, 241-245.

44. Schofield, A. L., Rudd, T. R., Martin, D. S., Fernig, D. G. and Edwards, C. (2007) Real-time monitoring of the development and stability of biofilms of Streptococcus mutans using the quartz crystal microbalance with dissipation monitoring. *Biosens Bioelectron*, **23**, 407-413.

45. Zhao, J., Zhu, W. and He, F. (2005) Rapidly determining E. coli and P. aeruginosa by an eight channels bulk acoustic wave impedance physical biosensor. *Sens Actuators, B*, **B107**, 271-276.

46. Ali, Z., O'Hare, W. T. and Theaker, B. J. (2003) Detection of bacterial contaminated milk by means of a quartz crystal microbalance based electronic nose. *J Therm Anal Calorim*, **71**, 155-161.

47. He, F. and Zhang, L. (2002) Rapid diagnosis of M. tuberculosis using a piezoelectric immunosensor. *Anal Sci*, **18**, 397-401.

48. Godber, B., Thompson, K. S. J., Rehak, M., Uludag, Y., Kelling, S., Sleptsov, A., Frogley, M., Wiehler, K., Whalen, C. and Cooper, M. A. (2005) Direct quantification of analyte concentration by resonant acoustic profiling. *Clin Chem* **51**, 1962-1972.

49. He, F., Zhang, L., Zhao, J., Hu, B. and Lei, J. (2002) A TSM immunosensor for detection of M. tuberculosis with a new membrane material. *Sens Actuators, B*, **B85**, 284-290.

50. Cooper, M. A. (2004) Advances in membrane receptor screening and analysis. *J Mol Recognit*, **17**, 286-315.

51. Saha, K., Bender, F. and Gizeli, E. (2003) Comparative Study of IgG Binding to Proteins G and A: Nonequilibrium Kinetic and Binding Constant Determination with the Acoustic Waveguide Device. *Anal Chem*, **75**, 835-842.

52. Campbell, G. A. and Mutharasan, R. (2005) Monitoring of the Self-Assembled Monolayer of 1-Hexadecanethiol on a Gold Surface at Nanomolar Concentration Using a Piezo-Excited Millimeter-Sized Cantilever Sensor. *Langmuir*, **21**, 11568-11573.

53. Shen, D., Huang, M., Chow, L. M. and Yang, M. (2001) Kinetic profile of the adsorption and conformational change of lysozyme on self-assembled monolayers as revealed by quartz crystal resonator. *Sens Actuators, B*, **B77**, 664-670.

54. Wu, B., Wu, K., Wang, P. and Zhu, D.-M. (2007) Adsorption Kinetics and Adsorption Isotherm of Poly(N-isopropylacrylamide) on Gold Surfaces Studied Using QCM-D. *J Phys Chem C*, **111**, 1131-1135.

55. Langmuir, I. (1932) VAPOR PRESSURES, EVAPORATION, CONDENSATION AND ADSORPTION. *J Am Chem Soc*, **54**, 2798-2832.

56. Janshoff, A., Galla, H.-J. and Steinem, C. (2000) Piezoelectric mass-sensing devices as biosensors-an alternative to optical biosensors? *Angew Chem, Int Ed*, **39**, 4004-4032.

57. Gerdon, A. E., Wright, D. W. and Cliffel, D. E. (2005) Quartz Crystal Microbalance Detection of Glutathione-Protected Nanoclusters Using Antibody Recognition. *Anal Chem*, **77**, 304-310.

58. Liu, Y., Yu, X., Zhao, R., Shangguan, D.-H., Bo, Z. and Liu, G. (2003) Real time kinetic analysis of the interaction between immunoglobulin G and histidine using

quartz crystal microbalance biosensor in solution. *Biosens Bioelectron*, **18**, 1419-1427.

59. Liu, Y., Tang, X., Liu, F. and Li, K. a. (2005) Selection of Ligands for Affinity Chromatography Using Quartz Crystal Biosensor. *Anal Chem*, **77**, 4248-4256.

60. Karpovich, D. S. and Blanchard, G. J. (1994) Direct Measurement of the Adsorption Kinetics of Alkanethiolate Self-Assembled Monolayers on a Microcrystalline Gold Surface. *Langmuir*, **10**, 3315-3322.

61. Ebara, Y., Itakura, K. and Okahata, Y. (1996) Kinetic Studies of Molecular Recognition Based on Hydrogen Bonding at the Air-Water Interface by Using a Highly Sensitive Quartz-Crystal Microbalance. *Langmuir*, **12**, 5165-5170.

62. Gerdon, A. E., Wright, D. W. and Cliffel, D. E. Quartz Crystal Microbalance Characterization of Nanostructure Assemblies in Biosensing In *Nanosystem Characterization Tools in the Life Sciences*; Kumar, C. S. S. R., Ed.; Wiley-VCH Verlag GmbH & Co. KGaA: Weinheim, Germany, **2006**; Vol. 3, pp 109-144.

63. Barry, C. E., III (2001) Interpreting cell wall "virulence factors" of Mycobacterium tuberculosis. *Trends Microbiol*, **9**, 237-241.

64. Alsteens, D., Verbelen, C., Dague, E., Raze, D., Baulard, A. R. and Dufrene, Y. F. (2008) Organization of the mycobacterial cell wall: a nanoscale view. *Pfluegers Arch*, **456**, 117-125.

65. (2007) TB Vaccine Testing Research Materials FAQs. *Colorado State University*. http://www.cvmbs.colostate.edu/microbiology/tb/faq.htm (accessed September 20, 2007).

66. Kaur, D., Lowary, T. L., Vissa, V. D., Crick, D. C. and Brennan, P. J. (2002) Characterization of the epitope of anti-lipoarabinomannan antibodies as the terminal hexaarabinofuranosyl motif of mycobacterial arabinans. *Microbiology*, **148**, 3049-3057.

67. Myszka, D. G., Morton, T. A., Doyle, M. L. and Chaiken, I. M. (1997) Kinetic analysis of a protein antigen-antibody interaction limited by mass transport on an optical biosensor. *Biophys Chem*, **64**, 127-137.

68. Hillier, A. C. and Ward, M. D. (1992) Scanning electrochemical mass sensitivity mapping of the quartz crystal microbalance in liquid media. *Anal Chem*, **64**, 2539-2554.

69. Eckert, R., Jeney, S. and HÖRber, J. K. H. (1997) Understanding Intercellular Interactions and Cell Adhesion: Lessons from studies on protein-metal interactions. *Cell Bio Inter*, **21**, 707-713.

70. Norde, W. (1986) Adsorption of proteins from solution at the solid-liquid interface. *Adv Coll Inter Sci*, **25**, 267-340.

71. Brewer, S. H., Glomm, W. R., Johnson, M. C., Knag, M. K. and Franzen, S. (2005) Probing BSA Binding to Citrate-Coated Gold Nanoparticles and Surfaces. *Langmuir*, **21**, 9303-9307.

72. Kato, K., Lian, L.-Y., Barsukov, I. L., Derrick, J. P., Kim, H., Tanaka, R., Yoshino, A., Shiraishi, M., Shimada, I., Arata, Y. and Roberts, G. C. K. (1995) Model for the complex between protein G and an antibody Fc fragment in solution. *Structure*, **3**, 79-85.

73. Boujday, S., Bantegnie, A., Briand, E., Marnet, P.-G., Salmain, M. and Pradier, C.-M. (2008) In-Depth Investigation of Protein Adsorption on Gold Surfaces: Correlating the Structure and Density to the Efficiency of the Sensing Layer. *J Phys Chem B*, **112**, 6708-6715.

74. Nilson, B. H. K., Loegdberg, L., Kastern, W., Bjoerck, L. and Akerstroem, B. (1993) Purification of antibodies using protein L-binding framework structures in the light chain variable domain. *J Immunol Methods*, **164**, 33-40.

75. Sharma, A., Saha, A., Bhattacharjee, S., Majumdar, S. and Das Gupta, S. K. (2006) Specific and randomly derived immunoactive peptide mimotopes of mycobacterial antigens. *Clin Vacc Immunol*, **13**, 1143-1154.

76. Hook, F., Rodahl, M., Brzezinski, P. and Kasemo, B. (1998) Energy Dissipation Kinetics for Protein and Antibody-Antigen Adsorption under Shear Oscillation on a Quartz Crystal Microbalance. *Langmuir*, **14**, 729-734.

77. Sauer-Eriksson, A. E., Kleywegt, G. J., Uhlen, M. and Jones, T. A. (1995) Crystal structure of the C2 fragment of streptococcal protein G in complex with the Fc domain of human IgG. *Structure*, **3**, 265-278.

78. Yang, L., Biswas, M. E. and Chen, P. (2003) Study of Binding between Protein A and Immunoglobulin G Using a Surface Tension Probe. *Biophys J*, **84**, 509-522.

79. Conway, J. H. and Sloane, J. J. A. *Sphere Packings, Lattices and Groups*, Springer-Verlag: New York, 1988, p. 2.

80. Brownsey, G. J., Noel, T. R., Parker, R. and Ring, S. G. (2003) The Glass Transition Behavior of the Globular Protein Bovine Serum Albumin. *Biophys J*, **85**, 3943-3950.

81. Tabak, M., Neto, D. o. d. S. and Salmon, C. E. G. (2006) On the Interaction of Bovine Serum Albumin (BSA) with Cethyltrimethyl Ammonium Chloride

Surfactant: Electron Paramagnetic Resonance (EPR) Study. *Braz J Phys*, **36**, 83-89.

82. Phillies, G. D. J. (1985) Diffusion of bovine serum albumin in a neutral polymer solution. *Biopolymers*, **24**, 379-386.

83. Wasyl, Z., Luchter, E. and Bielanski, W. (1971) Determination of the effective radius of protein molecules by thin-layer gel filtration. *Biochim Biophys Acta*, **243**, 11-18.

84. Jachimska, B., Wasilewska, M. and Adamczyk, Z. (2008) Characterization of Globular Protein Solutions by Dynamic Light Scattering, Electrophoretic Mobility, and Viscosity Measurements. *Langmuir*, **24**, 6866-6872.

85. De Wit, J. N. (1998) Nutritional and functional characteristics of whey proteins in food products. *J Dairy Sci*, **81**, 597-608.

86. Boehme, U. and Scheler, U. (2007) Effective charge of bovine serum albumin determined by electrophoresis NMR. *Chem Phys*, **435**, 342-345.

87. Rezwan, K., Meier, L. P., Rezwan, M., Vörös, J., Textor, M. and Gauckler, L. J. (2004) Bovine Serum Albumin Adsorption onto Colloidal Al2O3 Particles: A New Model Based on Zeta Potential and UV-Vis Measurements. *Langmuir*, **20**, 10055-10061.

88. Sarma, V. R., Silverton, E. W., Davies, D. R. and Terry, W. D. (1971) The Three-Dimensional Structure at 6 A Resolution of a Human Î³G1 Immunoglobulin Molecule. *J Biol Chem*, **246**, 3753-3759.

89. Labrijn, A. F., Poignard, P., Raja, A., Zwick, M. B., Delgado, K., Franti, M., Binley, J., Vivona, V., Grundner, C., Huang, C.-C., Venturi, M., Petropoulos, C. J., Wrin, T., Dimitrov, D. S., Robinson, J., Kwong, P. D., Wyatt, R. T., Sodroski, J. and Burton, D. R. (2003) Access of Antibody Molecules to the Conserved Coreceptor Binding Site on Glycoprotein gp120 Is Sterically Restricted on Primary Human Immunodeficiency Virus Type 1. *J Virol*, **77**, 10557-10565.

90. Kimura, S., Laosinchai, W., Itoh, T., Cui, X., Linder, C. R. and Brown, R. M., Jr. (1999) Immunogold Labeling of Rosette Terminal Cellulose-Synthesizing Complexes in the Vascular Plant Vigna angularis. *Plant Cell*, **11**, 2075-2086.

91. Narita, T., Kitazato, H., Koshimura, J., Suzuki, K., Murata, M. and Ito, S. (1999) Effects of protein meals on the urinary excretion of various plasma proteins in healthy subjects. *Nephron*, **81**, 398-405.

92. Mayans, M. O., Coadwell, W. J., Beale, D., Symons, D. B. and Perkins, S. J. (1995) Demonstration by pulsed neutron scattering that the arrangement of the

Fab and Fc fragments in the overall structures of bovine IgG1 and IgG2 in solution is similar. *Biochem J*, **311**, 283-291.

93. Boehm, M. K., Woof, J. M., Kerr, M. A. and Perkins, S. J. (1999) The fab and fc fragments of IgA1 exhibit a different arrangement from that in IgG: a study by X-ray and neutron solution scattering and homology modelling. *J Mol Recognit*, **286**, 1421-1447.

94. Takade, A., Umeda, A., Matsuoka, M., Yoshida, S.-i., Nakamura, M. and Amako, K. (2003) Comparative Studies of the Cell Structures of Mycobacterium leprae and M. tuberculosis Using the Electron Microscopy Freeze-Substitution Technique. *Microbiol Immunol*, **47**, 265-270.

95. Navratilova, I., Papalia, G. A., Rich, R. L., Bedinger, D., Brophy, S., Condon, B., Deng, T., Emerick, A. W., Guan, H.-W., Hayden, T., Heutmekers, T., Hoorelbeke, B., McCroskey, M. C., Murphy, M. M., Nakagawa, T., Parmeggiani, F., Qin, X., Rebe, S., Tomasevic, N., Tsang, T., Waddell, M. B., Zhang, F. F., Leavitt, S. and Myszka, D. G. (2007) Thermodynamic benchmark study using Biacore technology. *Anal Biochem*, **364**, 67-77.

96. Nelson, D. L. and Cox, M. M. *Lehninger Principles of Biochemistry*, 3rd ed., Worth Publishers: New York, **2000**.

97. Cooper, M. A., Dultsev, F. N., Minson, T., Ostanin, V. P., Abell, C. and Kieneman, D. (2001) Direct and sensitive detection of a human virus by rupture event scanning. *Nat Biotechnol*, **19**, 833-837.

98. Hook, F., Rodahl, M., Kasemo, B. and Brzezinski, P. (1998) Structural changes in hemoglobin during adsorption to solid surfaces: effects of pH, ionic strength, and ligand binding. *Proc Natl Acad Sci U S A*, **95**, 12271-12276.

99. Huang, C.-J., Cho, N.-J., Hsu, C.-J., Tseng, P.-Y., Frank, C. W. and Chang, Y.-C. (2010) Type I Collagen-Functionalized Supported Lipid Bilayer as a Cell Culture Platform. *Biomacromolecules*, **11**, 1231-1240.

100. Gerdon, A. E., Wright, D. W. and Cliffel, D. E. (2005) Hemagglutinin Linear Epitope Presentation on Monolayer-Protected Clusters Elicits Strong Antibody Binding. *Biomacromolecules*, **6**, 3419-3424.

101. Wittenberg, N. J. and Haynes, C. L. (2009) Using nanoparticles to push the limits of detection. *Wiley Interdiscip Rev Nanomed Nanobiotechnol*, **1**, 237-254.

102. Mackiewicz, M. R., Hodges, H. L. and Reed, S. M. (2010) C-Reactive Protein Induced Rearrangement of Phosphatidylcholine on Nanoparticle Mimics of Lipoprotein Particles. *J Phys Chem B*, **114**, 5556-5562.

103. Smith, S. (October 30, 2009) BU grad student develops infection: Possible link to lab experiments raises new safety concerns. *The Boston Globe*. http://www.boston.com/news/health/articles/2009/10/30/bu_grad_student_develops_infection/ (accessed September 23, 2010).

104. Mani, V., Chikkaveeraiah, B. V., Patel, V., Gutkind, J. S. and Rusling, J. F. (2009) Ultrasensitive Immunosensor for Cancer Biomarker Proteins Using Gold Nanoparticle Film Electrodes and Multienzyme-Particle Amplification. *ACS Nano*, **3**, 585-594.

105. Nam, J.-M., Thaxton, C. S. and Mirkin, C. A. (2003) Nanoparticle-based bio-bar codes for the ultrasensitive detection of proteins. *Science*, **301**, 1884-1886.

106. Tang, D. P., Yuan, R., Chai, Y. Q., Zhong, X., Dai, J. Y. and Zhang, L. Y. (2004) Novel potentiometric immunosensor for hepatitis B surface antigen using a gold nanoparticle-based biomolecular immobilization method. *Anal Biochem*, **333**, 345-350.

107. Ho, K.-C., Tsai, P.-J., Lin, Y.-S. and Chen, Y.-C. (2004) Using biofunctionalized nanoparticles to probe pathogenic bacteria. *Anal Chem*, **76**, 7162-7168.

108. Liu, G., Wang, J., Kim, J. and Jan, M. R. (2004) Electrochemical coding for multiplexed immunoassays of proteins. *Anal Chem*, **76**, 7126-7130.

109. Ingram, R. S., Hosteller, M. J. and Murray, R. W. (1997) Poly-hetero-w-functionalized alkanethiolate-stabilized gold cluster compounds. *J Am Chem Soc*, **119**, 9175-9178.

110. Agasti, S. S., Rana, S., Park, M.-H., Kim, C. K., You, C.-C. and Rotello, V. M. (2010) Nanoparticles for detection and diagnosis. *Adv Drug Delivery Rev*, **62**, 316-328.

111. Sardar, R., Funston, A. M., Mulvaney, P. and Murray, R. W. (2009) Gold Nanoparticles: Past, Present, and Future. *Langmuir*, **25**, 13840-13851.

112. Shangguan, T., Siegel, D. P., Lear, J. D., Axelsen, P. H., Alford, D. and Bentz, J. (1998) Morphological Changes and Fusogenic Activity of Influenza Virus Hemagglutinin. *Biophys J*, **74**, 54-62.

113. Bowman, M.-C., Ballard, T. E., Ackerson, C. J., Feldheim, D. L., Margolis, D. M. and Melander, C. (2008) Inhibition of HIV Fusion with Multivalent Gold Nanoparticles. *J Am Chem Soc*, **130**, 6896-6897.

114. Montet, X., Funovics, M., Montet-Abou, K., Weissleder, R. and Josephson, L. (2006) Multivalent Effects of RGD Peptides Obtained by Nanoparticle Display. *J Med Chem*, **49**, 6087-6093.

115. Wegner, G. J., Lee, H. J. and Corn, R. M. (2002) Characterization and optimization of peptide arrays for the study of epitope-antibody interactions using surface plasmon resonance imaging. *Anal Chem*, **74**, 5161-5168.

116. Muller, G. M. and Shapira, M. (1982) Anti-influenza response achieved by immunization with a synthetic conjugate. *Proc Natl Acad Sci USA*, **79**, 569-573.

117. Lu, Y., Ding, J. and Chen, Y.-H. (2002) A candidate vaccine against influenza virus intensively improved the immunogenicity of a neutralizing epitope. *Int Arch Allergy Immunol*, **127**, 245-250.

118. Brauer, G. *Handbook of Preparative Inorganic Chemistry*, Stecher, P. G., Ed., Academic Press: New York, 1965, Vol. 2, pp. 1053-1056.

119. Nwe, N., He, Q., Damrongwatanapokin, S., Du, Q., Manopo, I., Limlamthong, Y., Fenner, B., Spencer, L. and Kwang, J. (2006) Expression of hemagglutinin protein from the avian influenza virus H5N1 in a baculovirus/insect cell system significantly enhanced by suspension culture. *BMC Microbiology*, **6**, 16.

120. Templeton, A. C., Cliffel, D. E. and Murray, R. W. (1999) Redox and fluorophore functionalization of water-soluble, tiopronin-protected gold clusters. *J Am Chem Soc*, **120**, 4845-4849.

121. Gerdon, A. E., Wright, D. W. and Cliffel, D. W. (2005) Quartz crystal microbalance detection of glutathione-protected nanoclusters using antibody recognition. *Anal Chem*, **77**, 304-310.

122. Templeton, A. C., Chen, S., Gross, S. M. and Murray, R. W. (1999) Water-Soluble, Isolatable Gold Clusters Protected by Tiopronin and Coenzyme A Monolayers. *Langmuir*, **15**, 66-76.

123. Gerdon, A. E., Wright, D. W. and Cliffel, D. E. Quartz Crystal Microbalance Characterization of Nanostructure Assemblies in Biosensing In *Characterization Tools for Nanosystems in Life Sciences*; Kumar, C., Ed.; Wiley-VCH: New York, 2005; Vol. 3, pp 109-144.

124. Hostetler, M. J., Wingate, J. E., Zhong, C.-J., Harris, J. E., Vachet, R. W., Clark, M. R., Londono, J. D., Green, S. T., Stokes, J. J. and Wignall, G. D. (1998) Alkanethiolate gold cluster molecules with core diameters from 1.4 to 5.2 nanometers: core and molecular properties as a function of core size. *Langmuir*, **14**, 17-30.

125. Simpson, C. A., Huffman, B. J., Gerdon, A. E. and Cliffel, D. E. (2010) Unexpected Toxicity of Monolayer Protected Gold Clusters Eliminated by PEG-Thiol Place Exchange Reactions. *Chem Res Toxicol*, **23**, 1608-1616.

126. Chan, W. C. and White, P. D. *Fmoc Solid Phase Peptide Synthesis*, Hames, B. D., Ed., Oxford University Press: New York, 2000, pp. 9-74.

127. Lloyd-Williams, P., Albercicio, F. and Giralt, E. *Chemical Approaches to the Synthesis of Peptides and Proteins*, CRC Press: New York, 1997, pp. 12-16.

128. Van Regenmortel, M. H. V. (1989) The concept and operational definition of prorein epitopes. *Phil Trans R Soc B*, **323**, 451-466.

129. Hostetler, M. J., Templeton, A. C. and Murray, R. W. (1999) Dynamics of place-exchange reactions on monolater-protected gold cluster molecules. *Langmuir*, **15**, 3782-3789.

130. Montalti, M., Prodi, L., Zaccheroni, N., Baxter, R., Teobaldi, G. and Zerbetto, F. (2003) Kinetics of place-exchange reactions of thiols on gold nanoparticles. *Langmuir*, **19**, 5172-5174.

131. Jadzinsky, P. D., Calero, G., Ackerson, C. J., Bushnell, D. A. and Kornberg, R. D. (2007) Structure of a thiol monolayer-protected gold nanoparticle at 1.1 angstrom resolution. *Science*, **318**, 430-433.

132. Buttry, D. A. Applications of the QCM to Electrochemistry In *Electroanalytical Chemistry: A Series of Advances*; Bard, A. J., Ed.; Marcel Dekker: New York, 1991; Vol. 17, pp 10.

133. Tsionsky, V., Daikhin, L., Urbakh, M. and Gileadi, E. Theoretical Interpretation of the QCM Response In *Electroanalytical Chemistry: A Series of Advances*; Bard, A. J., Rubinstein, I., Eds.; Marcel Dekker: New York, 2004; Vol. 22, pp 8-26.

134. Kanazawa, K. K. and Gordon, J. G. (1985) Frequency of a quartz microbalance in contact with liquid. *Anal Chem*, **57**, 1771-1772.

135. Martin, S. E., Granstaff, V. and Frye, G. (1991) Characterization of a quartz crystal microbalance with simultaneous mass and liquid loading. *Anal Chem*, **63**, 2272-2281.

136. Kanazawa, K. K. (1997) Mechanical behaviour of films on the quartz microbalance. *Faraday Discuss*, **107**, 77-90.

137. Harkness, K. M., Fenn, L. S., Cliffel, D. E. and McLean, J. A. (2010) Surface Fragmentation of Complexes from Thiolate Protected Gold Nanoparticles by Ion Mobility-Mass Spectrometry. *Anal Chem*, **82**, 3061-3066.

138. Steinitz, M. (2000) Quantitation of the Blocking Effect of Tween 20 and Bovine Serum Albumin in ELISA Microwells. *Anal Biochem*, **282**, 232-238.

139. Hehre, W. H., *Spartan '04* 1.0.1; Wavefunction, Inc.; Irvine, CA, 2005.

140. Sauerbrey, G. (1959) The use of quartz oscillations for weighing thin layers and for microweighing. *Zeitschrift fuer Physik*, **155**, 206-222.

141. Su, X.-L. and Li, Y. (2005) A QCM immunosensor for Salmonella detection with simultaneous measurements of resonant frequency and motional resistance. *Biosensors and Bioelectronics*, **21**, 840-848.

142. Hirst, E. R., Yuan, Y. J., Xu, W. L. and Bronlund, J. E. (2008) Bond-rupture immunosensors - A review. *Biosens Bioelectron*, **23**, 1759-1768.

143. Cooper, M. A. (2003) Biosensing using rupture event scanning (REVS) *Meas Sci Technol*, **14**, 1888-1893.

144. Majumder, N., Bhattacharjee, S., Bhattacharyya, S., Dey, R., Guha, P., Pal, N. K. and Majumdar, S. (2008) Restoration of impaired free radical generation and proinflammatory cytokines by MCP-1 in mycobacterial pathogenesis. *Scand J Immunol* **67**, 329-339.

145. Grune, T. and Davies, K. J. (2003) The proteasomal system and HNE-modified proteins. *Mol Aspects Med*, **24**, 195-204.

146. Uchida, K. (2003) 4-Hydroxy-2-nonenal: a product and mediator of oxidative stress. *Prog Lipid Res*, **42**, 318-343.

147. Finkel, T. and Holbrook, N. J. (2000) Oxidants, oxidative stress and the biology of ageing. *Nature*, **408**, 239-247.

148. Dietert, R. R. and Golemboski, K. A. (1998) Avian macrophage metabolism. *Poult Sci*, **77**, 990-997.

149. Endo, K., Miyasaka, T., Mochizuki, S., Aoyagi, S., Himi, N., Asahara, H., Tsujioka, K. and Sakai, K. (2002) Development of a superoxide sensor by immobilization of superoxide dismutase. *Sens Actuators, B* **83**, 30-34.

150. Radi, R. (2004) Nitric oxide, oxidants, and protein tyrosine nitration. *Proc Natl Acad Sci U S A*, **101**, 4003-4008.

151. Sawyer, D. T. and Valentine, J. S. (1981) How super is superoxide? *Acc Chem Res*, **14**, 393-400.

152. Imlay, J. A. (2008) Cellular defenses against superoxide and hydrogen peroxide. *Annu Rev Biochem*, **77**, 755-776.

153. Amatore, C., Arbault, S., Ferreira, D. C. M., Tapsoba, I. and Verchier, Y. (2008) Vitamin C stimulates or attenuates reactive oxygen and nitrogen species (ROS, RNS) production depending on cell state: Quantitative amperometric measurements of oxidative bursts at PLB-985 and RAW 264.7 cells at the single cell level. *J Electroanal Chem*, **615**, 34-44.

154. Dahlgren, C. and Karlsson, A. (1999) Respiratory burst in human neutrophils. *J Immunol Methods*, **232**, 3-14.

155. Amatore, C., Arbault, S., Bouton, C., Coffi, K., Drapier, J.-C., Ghandour, H. and Tong, Y. (2006) Monitoring in real time with a microelectrode the release of reactive oxygen and nitrogen species by a single macrophage stimulated by its membrane mechanical depolarization. *ChemBioChem*, **7**, 653-661.

156. Amatore, C., Arbault, S. and Koh, A. C. W. (2010) Simultaneous Detection of Reactive Oxygen and Nitrogen Species Released by a Single Macrophage by Triple Potential-Step Chronoamperometry. *Anal Chem*, **82**, 1411-1419.

157. Amatore, C., Arbault, S., Chen, Y., Crozatier, C. and Tapsoba, I. (2007) Electrochemical detection in a microfluidic device of oxidative stress generated by macrophage cells. *Lab Chip*, **7**, 233-238.

158. Amatore, C., Arbault, S., Bouton, C., Drapier, J.-C., Ghandour, H. and Koh, A. C. W. (2008) Real-time amperometric analysis of reactive oxygen and nitrogen species released by single immunostimulated macrophages. *ChemBioChem*, **9**, 1472-1480.

159. Beissenhirtz, M. K., Scheller, F. W. and Lisdat, F. (2004) A Superoxide Sensor Based on a Multilayer Cytochrome c Electrode. *Anal Chem*, **76**, 4665-4671.

160. Cortina-Puig, M., Muñoz-Berbel, X., Calas-Blanchard, C. and Marty, J.-L. (2009) Electrochemical characterization of a superoxide biosensor based on the co-immobilization of cytochrome c and XOD on SAM-modified gold electrodes and application to garlic samples. *Talanta*, **79**, 289-294.

161. Kintzios, S., Marinopoulou, I., Moschopoulou, G., Mangana, O., Nomikou, K., Endo, K., Papanastasiou, I. and Simonian, A. (2006) Development of a novel, multi-analyte biosensor system for assaying cell division: Identification of cell proliferation/death precursor events. *Biosens Bioelectron*, **21**, 1365-1373.

162. Di Risio, S. and Yan, N. (2007) Piezoelectric Ink-Jet Printing of Horseradish Peroxidase: Effect of Ink Viscosity Modifiers on Activity. *Macromol Rapid Commun*, **28**, 1934-1940.

163. Deravi, L. F., Gerdon, A. E., Cliffel, D. E. and Wright, D. W. (2007) Output analysis of materials ink-jet printer. *Appl Phys Lett*, **91**, 113114/113111-113114/113113.

164. Deravi, L. F., Sumerel, J. L., Sewell, S. L. and Wright, D. W. (2008) Piezoelectric Inkjet Printing of Biomimetic Inks for Reactive Surfaces. *Small*, **4**, 2127-2130.

165. Andrieux, C. P., Hapiot, P. and Saveant, J. M. (1987) Mechanism of superoxide ion disproportionation in aprotic solvents. *J Am Chem Soc*, **109**, 3768-3775.

166. Dietz, R., Forno, A. E. J., Larcombe, B. E. and Peover, M. E. (1970) Nucleophilic reactions of electrogenerated superoxide ion. *J Chem Soc B*, 816-820.

167. Vasudevan, D. and Wendt, H. (1995) Electroreduction of oxygen in aprotic media. *J Electroanal Chem*, **392**, 69-74.

168. Pekmez, K., Can, M. and Yildiz, A. (1993) Electrochemistry in Aprotic Solvents Containing Anhydrous Perchloric Acid: Electroreduction Behavior of Quinones. *Electrochim Acta*, **38**, 607-611.

169. Wei, Y., Ji, X., Dang, X. and Hu, S. (2003) Studies on electrochemical properties and scavenge of superoxide anion in aprotic media by using carbon nanotubes powder microelectrode. *Bioelectrochemistry*, **61**, 51-56.

170. Saha, M. S. and Ohsaka, T. (2005) Electrode kinetics of the O2/O2- redox couple at Hg electrode in the presence of PVC in aprotic media. *Electrochim Acta*, **50**, 4746-4751.

171. Wei, Y., Dang, X. and Hu, S. (2004) Electrochemical properties of superoxide ion in aprotic media. *Russ J Electrochem*, **40**, 400-404.

172. Bard, A. J. and Faulkner, L. R. *Electrochemical Methods: Fundamental and Applications*, 2nd ed., John Wiley and Sons, Inc: New York, 2001.

173. Porras, A. G., Olson, J. S. and Palmer, G. (1981) The reaction of reduced xanthine oxidase with oxygen. Kinetics of peroxide and superoxide formation. *J Biol Chem*, **256**, 9096-9103.

174. Hamasaki, T., Kashiwagi, T., Imada, T., Nakamichi, N., Aramaki, S., Toh, K., Morisawa, S., Shimakoshi, H., Hisaeda, Y. and Shirahata, S. (2008) Kinetic analysis of superoxide anion radical-scavenging and hydroxyl radical-scavenging activities of platinum nanoparticles. *Langmuir*, **24**, 7354-7364.

175. Bonini, M. G., Miyamoto, S., Di Mascio, P. and Augusto, O. (2004) Production of the Carbonate Radical Anion during Xanthine Oxidase Turnover in the Presence of Bicarbonate. *J Biol Chem*, **279**, 51836-51843.

176. Hashimoto, S. (1974) New spectrophotometric assay method of xanthine oxidase in crude tissue homogenate. *Anal Biochem*, **62**, 426-435.

177. Pospisil, L., King, B. T. and Michl, J. (1998) Voltammetry in benzene using lithium dodecamethylcarba-closo-dodecaborate, LiCB11Me12, as a supporting electrolyte: reduction of Ag+. *Electrochim Acta*, **44**, 103-108.

178. Miller, R. C. and Fuoss, R. M. (1953) Electrolyte-Solvent Interaction. II. Quaternary Salts in Methanol-Nitromethane and Methanol-Benzene Mixtures. *J Am Chem Soc*, **75**, 3076-3080.

179. McCord, J. M. and Fridovich, I. (1969) Superoxide dismutase. Enzymic function for erythrocuprein (hemocuprein). *J Biol Chem*, **244**, 6049-6055.

180. Lima, E. A., Snider, R. M., Reiser, R. S., McKenzie, J. R., Eklund, S., Cliffel, D. E. and Wikswo., J. P. (In preparation) Multipotentiostat for multianalyte microphysiometry in eight electrochemical cells simultaneously. *Sensors and Actuators B: Chemical*,

181. Eklund, S. E., Taylor, D., Kozlov, E., Prokop, A. and Cliffel, D. E. (2004) A microphysiometer for simultaneous measurement of changes in extracellular glucose, lactate, oxygen, and acidification rate. *Anal Chem*, **76**, 519-527.

182. Terech, A., Pucheault, J. and Ferradini, C. (1983) Saturation Behavior of the Manganese-containing Superoxide-Dismutase from Paracoccus-Denitrificans. *Biochem Biophys Res Commun*, **113**, 114-120.

183. Lide, D. R., Ed. *CRC Handbook of Chemistry and Physics, 86th Edition*, p. 6-222, CRC Press LLC: New York, 2004.

184. Abreu, I. A. and Cabelli, D. E. (2010) Superoxide dismutases-a review of the metal-associated mechanistic variations. *Biochimica Et Biophysica Acta-Proteins and Proteomics*, **1804**, 263-274.

185. Eklund, S. E., Cliffel, D. E., Kozlov, E., Prokop, A., Wikswo, J. and Baudenbacher, F. (2003) Modification of the Cytosensor microphysiometer to simultaneously measure extracellular acidification and oxygen consumption rates. *Anal Chim Acta*, **496**, 93-101.

186. Pelmenschikov, V. and Siegbahn, P. E. M. (2006) Nickel Superoxide Dismutase Reaction Mechanism Studied by Hybrid Density Functional Methods. *J Am Chem Soc*, **128**, 7466-7475.

187. McCracken, J., Peisach, J. and Dooley, D. M. (1987) Cu(II) coordination chemistry of amine oxidases. Pulsed EPR studies of histidine imidazole, water, and exogenous ligand coordination. *J Am Chem Soc*, **109**, 4064-4072.

188. Lineweaver, H. and Burk, D. (1934) The Determination of Enzyme Dissociation Constants. *J Am Chem Soc*, **56**, 658-666.

189. Michaelis, L. and Menten, M. L. (1913) Kinetics of Invertase Action. *Biochem Z* **49.**, 333-369.

190. Meier, B., Michel, C., Saran, M., Huttermann, J., Parak, F. and Rotilio, G. (1995) Kinetic and Spectroscopic Studies on a Superoxide-Dismutase from Propionibacterium-Shermanii that is Active with Iron or Manganese- pH Dependence. *Biochem J*, **310**, 945-950.

191. Fee, J. A. and Bull, C. (1986) Steady-state kinetic studies of superoxide dismutases. Saturative behavior of the copper- and zinc-containing protein. *J Biol Chem*, **261**, 13000-13005.

192. Clark, R. A. and Bowden, E. F. (1997) Voltammetric Peak Broadening for Cytochrome c/Alkanethiolate Monolayer Structures: Dispersion of Formal Potentials. *Langmuir*, **13**, 559-565.

193. Berdichevsky, Y., Khandurina, J., Guttman, A. and Lo, Y. H. (2004) UV/ozone modification of poly(dimethylsiloxane) microfluidic channels. *Sensors and Actuators B-Chemical*, **97**, 402-408.

194. Bodas, D. and Khan-Malek, C. (2006) Formation of more stable hydrophilic surfaces of PDMS by plasma and chemical treatments. *Microelectron Eng*, **83**, 1277-1279.

195. Inoue, K. Y., Ino, K., Shiku, H., Kasai, S., Yasukawa, T., Mizutani, F. and Matsue, T. (2010) Electrochemical monitoring of hydrogen peroxide released from leucocytes on horseradish peroxidase redox polymer coated electrode chip. *Biosens Bioelectron*, **25**, 1723-1728.

196. Oh, S. R. (2008) Thick single-layer positive photoresist mold and poly(dimethylsiloxane) (PDMS) dry etching for the fabrication of a glass-PDMS-glass microfluidic device. *Journal of Micromechanics and Microengineering*, **18**, 115025.

197. Lotters, J. C., Olthuis, W., Veltink, P. H. and Bergveld, P. (1997) The mechanical properties of the rubber elastic polymer polydimethylsiloxane for sensor applications. *Journal of Micromechanics and Microengineering*, **7**, 145-147.

198. Bhagat, A. A. S., Jothimuthu, P. and Papautsky, I. (2007) Photodefinable polydimethylsiloxane (PDMS) for rapid lab-on-a-chip prototyping. *Lab Chip*, **7**, 1192-1197.

199. Cong, H. L. and Pan, T. R. (2008) Photopatternable conductive PDMS materials for microfabrication. *Adv Funct Mater*, **18**, 1912-1921.

200. Lo, Y.-C., Wu, Y.-H., Huang, C.-S., Liu, H.-W., Lin, C.-H., Lin, J., Hsu, W. and Wang, C. (2004) Sub-Microfabrication of Protein Micropatterns for Cell Biology Applications. *2004 International Conference on MEMS, NANO and Smart Systems*, 226-232.

201. Meyvantsson, I. and Beebe, D. J. (2008) Cell Culture Models in Microfluidic Systems. *Annu Rev Anal Chem*, **1**, 423-449.

202. Sasoglu, F. M., Bohl, A. J. and Layton, B. E. (2006) Microfabrication procedure of PDMS microbeam array using photolithography for laminin printing and piconewton force transduction on axons. *Conf Proc IEEE Eng Med Biol Soc*, **1**, 2844-2847.

203. Satyanarayana, S., Karnik, R. N. and Majumdar, A. (2005) Stamp-and-stick room-temperature bonding technique for microdevices. *Journal of Microelectromechanical Systems*, **14**, 392-399.

204. Arivanandhan, M., Sankaranarayanan, K. and Ramasamy, P. (2007) Studies on large uniaxially grown benzophenone single crystals. *Cryst Res Technol*, **42**, 578-582.

205. Bhattacharya, S., Datta, A., Berg, J. M. and Gangopadhyay, S. (2005) Studies on surface wettability of poly(dimethyl) siloxane (PDMS) and glass under oxygen-plasma treatment and correlation with bond strength. *Journal of Microelectromechanical Systems*, **14**, 590-597.

206. Eklund, S. E., Snider, R. M., Wikswo, J., Baudenbacher, F., Prokop, A. and Cliffel, D. E. (2006) Multianalyte microphysiometry as a tool in metabolomics and systems biology. *J Electroanal Chem*, **587**, 333-339.

207. Siems, W. G., Capuozzo, E., Verginelli, D., Salerno, C., Crifo, C. and Grune, T. (1997) Inhibition of NADPH oxidase-mediated superoxide radical formation in PMA-stimulated human neutrophils by 4-hydroxynonenal--binding to -SH and -NH2 groups. *Free Radic Res*, **27**, 353-358.

208. Costa Rosa, L. F., Curi, R., Murphy, C. and Newsholme, P. (1995) Effect of adrenaline and phorbol myristate acetate or bacterial lipopolysaccharide on stimulation of pathways of macrophage glucose, glutamine and O2 metabolism. Evidence for cyclic AMP-dependent protein kinase mediated inhibition of

glucose-6-phosphate dehydrogenase and activation of NADP+-dependent 'malic' enzyme. *Biochem J*, **310 (Pt 2)**, 709-714.

209. Iwata, R., Satoh, R., Iwasaki, Y. and Akiyoshi, K. (2008) Covalent immobilization of antibody fragments on well-defined polymer brushes via site-directed method. *Colloids and Surfaces B: Biointerfaces*, **62**, 288-298.

210. Kobayashi, N., Oyama, H., Nakano, M., Kanda, T., Banzono, E., Kato, Y., Karibe, T., Nishio, T. and Goto, J. (2009) "Cleavable" hapten-biotin conjugates: Preparation and use for the generation of anti-steroid single-domain antibody fragments. *Anal Biochem*, **387**, 257-266.

211. Pathak, S., Davidson, M. C. and Silva, G. A. (2007) Characterization of the Functional Binding Properties of Antibody Conjugated Quantum Dots. *Nano Lett*, **7**, 1839-1845.

212. Jia, F., Shelton, T. D. and Lewis, M. R. (2007) Preparation, Characterization, and Biological Evaluation of a Streptavidin-Chimeric T84.66 Conjugate for Antibody Pretargeting. *Cancer Biother Radiopharm*, **22**, 654-664.

213. Kamruzzahan, A. S. M., Ebner, A., Wildling, L., Kienberger, F., Riener, C. K., Hahn, C. D., Pollheimer, P. D., Winklehner, P., Hoelzl, M., Lackner, B., Schoerkl, D. M., Hinterdorfer, P. and Gruber, H. J. (2006) Antibody Linking to Atomic Force Microscope Tips via Disulfide Bond Formation. *Bioconjugate Chem*, **17**, 1473-1481.

214. Ji, T., Muenker, M. C., Papineni, R. V. L., Harder, J. W., Vizard, D. L. and McLaughlin, W. E. (2010) Increased Sensitivity in Antigen Detection with Fluorescent Latex Nanosphere-IgG Antibody Conjugates. *Bioconjugate Chem*, **21**, 427-435.

215. Babacan, S., Pivarnik, P., Letcher, S. and Rand, A. G. (2000) Evaluation of antibody immobilization methods for piezoelectric biosensor application. *Biosens Bioelectron*, **15**, 615-621.

216. Galli Marxer, C., Collaud Coen, M. and Schlapbach, L. (2003) Study of adsorption and viscoelastic properties of proteins with a quartz crystal microbalance by measuring the oscillation amplitude. *J Colloid Interface Sci*, **261**, 291-298.

217. Housden, N. G., Harrison, S., Roberts, S. E., Beckingham, J. A., Graille, M., Stura, E. and Gore, M. G. (2003) Immunoglobulin-binding domains: Protein L from Peptostreptococcus magnus. *Biochem Soc Trans*, **31**, 716-718.

218. Chatrathi, M. P., Wang, J. and Collins, G. E. (2007) Sandwich electrochemical immunoassay for the detection of Staphylococcal enterotoxin B based on immobilized thiolated antibodies. *Biosens Bioelectron*, **22**, 2932-2938.

219. Cleland, W. W. (1964) Dithiothreitol, a New Protective Reagent for SH Groups. *Biochemistry*, **3**, 480-482.

220. Hong, J., Lee, A., Han, H. and Kim, J. (2009) Structural characterization of immunoglobulin G using time-dependent disulfide bond reduction. *Anal Biochem*, **384**, 368-370.

221. Fasman, D. G., Ed. *Practical Handbook of Biochemistry and Molecular Biology*, p. 266, CRC Press: Boston, 1992.